Contribution to the investigation of dynamic responses of human tissues under high velocity impacts using finite element modeling

Jianbo Shen

THESE DE DOCTORAT DE L'ETABLISSEMENT UNIVERSITE BOURGOGNE FRANCHE-COMTE

PREPAREE A L'UNIVERSITE DE TECHNOLOGIE DE BELFORT-MONTBELIARD

Ecole doctorale n°

Sciences physiques pour l'ingénieur et microtechniques-SPIM

Doctorat de Mécanique

Par

Jianbo SHEN

Contribution to the investigation of dynamic responses of human tissues under high velocity impacts using finite element modeling

Thèse présentée et soutenue à UTBM site de Sévenans, le 2 Février 2022

Composition du Jury :

M. Sébastien LAPORTE	Professeur des Université, ENSAM Paris	Rapporteur
Mme Anne-Sophie BONNET	Professeur des Université, Université de Lorraine	Rapporteur
Mme Emmanuelle JACQUET	Maitre de Conférence HDR, Université de Franche-Comté	Examinateur
M. Eric WAGNAC	Professeur, Ecole de Technologie Supérieur	Président de jury
M. François PEYRAUT	Professeur des Université, UTBM	Examinateur
M. Sébastien ROTH	Professeur des Université, UTBM	Directeur de thèse

Acknowledgements

I would like to sincerely thank my supervisor Prof. Sébastien ROTH for his dedicated guidance during the last three years. This thesis could not be accomplished without his suggestions, support, trust and encouragement.

I also would like to express my sincere thanks to the members of my thesis jury: Prof. Sébastien LAPORTE from ENSAM Paris, Prof. Anne-Sophie BONNET from Université de Lorraine, Assoc. Prof. Emmanuelle JACQUET from Université de Franche-Comté, Prof. Eric WAGNAC from Ecole de Technologie Supérieur and Prof. François PEYRAUT from UTBM for accepting and spending their valuable time reviewing my thesis.

I am also grateful to China Scholarship Council (CSC) for providing me the financial support without which I could not finish my PhD thesis.

Meanwhile, I really appreciate it that I have many friendly and helpful colleagues in our laboratory: Shuangshuang Meng, Bingcong Jian, Monzer Al Khalil, Lorenzo Taddei and Hassan Frissane, your supports are also helpful to my thesis. I also want to express my thanks to the friends who accompanied me when I lived abroad alone in the past three years: Hongyuan Luo, Wenheng Liu, Shuohong Gao, Shaowu Liu, Zhiguang Hua, Cheng Chang, etc. Certainly, beautiful France and friendly French people provide me with good living environments and impress me a lot.

Finally, my parents' love gives me constant power, I love them too.

Contents

List of Figures

List of Tables

List of Acronyms

World Health Organization (WHO)
Postmortem Human Subjects (PMHS)
Finite Element (FE)
Styrene-Ethylene-Butylene-Styrene (SEBS)
Three Point Bending (3PB)
Anthropomorphic Test Devices (ATDs)
Split Hopkinson Pressure Bar (SHPB)
Acute Respiratory Distress Syndrome (ARDS)
Abbreviated Injury Scale (AIS)
Behind Armor Blunt Trauma (BABT)
Less-Lethal Kinetic (LLKE)
Motor Vehicle Crashes (MVCs)
Smoothed Particle Hydrodynamics (SPH)
Equation of State (EOS)
Cutaneous Surface Gauge (CSG)
Pleural Surface Gauge (PSG)

List of Symbols

E	Young's modulus (MPa)
$\boldsymbol{s}$	Deviatoric stress (MPa)
G	Shear modulus (MPa)
$\boldsymbol{e}$	Deviatoric strain
$\boldsymbol{\varepsilon}$	Elastic strain tensor
$\boldsymbol{I}$	Unit tensor
p	Pressure (MPa)
C_n	Material constant (n=0, 1, 2, 3)
μ	Dimensionless parameter
ρ	Current mass density (g/mm^3)
ρ_0	Initial mass density (g/mm^3)
c_0	Bulk wave velocity (m/s)
k	Hugoniot constant parameter
$\boldsymbol{\sigma}$	Stress tensor (MPa)
$\dot{\varepsilon}$	Strain rate (s^{-1})
E_0	Initial elastic modulus (MPa)
$F_{coulomb}$	Friction coefficient
ν	Poisson's ratio
m	Mass (g)
l	Length (mm)
r	Radius (mm)
α	Angle (degree)
$2a$	Major axis (mm)
$2b$	Minor axis (mm)
h_s	Superior layer thickness (mm)
h_i	Inferior layer thickness (mm)
σ_y	Yield stress (MPa)
E_t	Tangent modulus (MPa)
ε_{inc}	Incident strain
ε_{ref}	Reflected strain
ε_{tr}	Transmitted strain
v_{inp}	Input interface velocity (m/s)

v_{out}	Output interface velocity (m/s)
u_{inp}	Input interface displacement (mm)
u_{out}	Output interface displacement (mm)
F_{inp}	Input interface contact force (N)

General Introduction

The thorax part is found to be one of the most injured body areas under high velocity impacts, just second behind the head part. Thoracic injuries happen frequently in various frameworks of high velocity impact biomechanics such as road traffic accidents, sports and ballistic impacts. According to the World Health Organization (WHO), approximately 1.3 million people lose their lives as a result of road traffic crashes each year, and more people suffer from physical disabilities because of non-fatal injuries. Rib fractures and soft tissue injuries like lung injuries are the most common thoracic injuries and can be life-threatening. Specifically, rib fragments can also result in soft tissue injuries like pneumothorax and hemothorax by perforating soft organs. For vulnerable populations such as the elderly, they need longer hospital stays and have relatively higher fatality due to the decrease thoracic injury tolerance. Therefore, in order to better understand human thorax responses and injuries under high velocity impacts, it is of importance to investigate the dynamic responses of human tissues, which can provide valuable medical and forensic information and is also useful for designing and optimizing protecting devices.

Biomechanical experiments employing Postmortem Human Subjects (PMHS) and anesthetized animals are in general conducted to reach the objective of understanding the human body responses under high velocity impacts. However, the use of human cadavers is limited because of the high financial costs and ethical issues. Meanwhile, the development of computer science allows researchers to apply numerical simulations such as Finite Element (FE) method to simulate and investigate the behaviors of human tissues. So it is essential to take advantage of numerical tools to overcome the limitations in biomechanical experiments. In recent years, many biomechanical FE models have been established and employed to repeat real-world impact loading conditions to investigate human tissue behaviors, which include whole human body models, human thorax models and individual rib models.

Therefore, this thesis aims to contribute to the investigation of dynamic responses of human tissues under high velocity impacts using finite element modeling. Human tissues include soft tissues and hard tissues. In thoracic injuries, lung injuries are most common soft tissue injuries, and rib fractures are frequent hard tissue injuries. The usage of human soft tissue substitutes like rubber, clay, ballistic gelatin and polymer is popular in recent years, which can avoid high costs and ethical issues in human cadavers' experiments. Among soft tissue substitutes, the synthetic polymer Styrene-Ethylene-Butylene-Styrene (SEBS) gel highlights a number of benefits against the typical ballistic gelatin such as environmental stability and transparency. In recent years, researchers adopted the SEBS gel as soft tissue substitute in biomechanics impacts. Few

studies pay attention to the development of constitutive law of the synthetic polymer SEBS gel. Consequently, this thesis first aims to propose a novel strain-rate-dependent elasto-hydrodynamic constitutive law of the SEBS gel for the first time, which can interpret the dynamic behaviors of SEBS gel under various loading configurations. Dynamic three point bending (3PB) tests and anterior-posterior bending tests of isolated ribs are typically carried out to understand rib fractures, which mimic the environments like in car crash accidents. Only a few studies concentrate on dynamic 3PB tests of ribs under high velocity impacts using Split Hopkinson Pressure Bar (SHPB) apparatus, thus this thesis then numerically investigates the effect of geometrical and mechanical parameters of ribs submitted to high velocity impacts applying 3PB SHPB apparatus. In addition, previous numerical studies on ribs' dynamic anterior-posterior bending defined human rib cortical bone material models using material data obtained from tensile coupon tests because of the absence of rib cortical bone compressive material properties in the literature. Actually, the rib suffers both tensile and compressive loading modes during MVCs, for instance, the cutaneous surface suffers tension while the pleural surface suffers compression in frontal crash conditions. Therefore, this thesis also develops rib FE models with various material properties including human rib cortical bone material properties from different loading modes (tension and compression), strain rates (0.5 strain/s and 0.005 strain/s) and ages as well as porcine rib material properties, and validates them through replicating experimental configurations, in order to better understand rib structural responses and fracture locations under dynamic anterior-posterior bending.

The outline of the thesis is organized as follows:

Chapter 1 presents an overview of the research background of this thesis. The biomechanics of human thorax is introduced, and human thorax anatomy is presented first. Then, soft tissues and hard tissues (especially ribs) in human thorax part are introduced respectively, including soft organs, rib anatomy, material properties and injuries of soft tissues and rib fractures. Subsequently, the literature review of experimental and numerical studies of impacts on soft tissues and ribs are conducted. Finally, we briefly summarize the bibliographical study.

Chapter 2 develops a novel strain-rate-dependent elasto-hydrodynamic constitutive law of the synthetic polymer SEBS gel based on the mechanical characterization extracted from the literature. The proposed law is then implemented as a user material subroutine programed in Fortran in an explicit nonlinear FE software Radioss (Altair Hyperworks) to reproduce various loading configurations in order to validate the accuracy of the model, and the effect of strain rate is investigated. Numerical analysis reveals that the strain-rate-dependence effect is significant in SEBS gel especially for high strain rates.

Chapter 3 investigates the dynamic behaviors of isolated porcine ribs under three point

bending (3PB) based on finite element simulations, and both porcine and human rib material properties are applied for comparison. A 3PB Split Hopkinson Pressure Bar (SHPB) apparatus is established in order to replicate the experimental configurations. The numerical curved beam rib models are validated and show biofidelic behaviors by comparing numerical and experimental results. In addition, sensitivity studies are conducted to study the effects of geometrical and mechanical parameters such as cortical thickness, curvature radius and strain rate on dynamic responses of ribs under high velocity impacts. Numerical analysis highlights the significant effect of geometrical parameters on ribs dynamic behaviors. The consideration of the effect of mechanical parameters like loading mode and strain rate sensitivity in FE rib models is also needed.

Chapter 4 creates human rib FE models and validates them through replicating experimental configurations of ribs under dynamic anterior-posterior bending. Validation tests are conducted by comparing rib structural properties and fracture locations against experimental data of the literature based on finite element analysis. Human rib cortical bone material properties from different loading modes (tension and compression), strain rates (0.5 strain/s and 0.005 strain/s) and ages as well as porcine rib material properties are applied. Numerical force-displacement relationship, cortical strain, rotation and fracture locations correspond well with published experimental data, which demonstrates the robustness of the finite element rib models. Numerical rib structural responses are found to be sensitive to material properties from different loading modes, strain rates and ages. Therefore, it is necessary to consider the effect of material properties from different loading modes, strain rates and ages when establishing rib FE models.

Chapter 5 summarizes the overall conclusions of this thesis, and points out the existing limitations, and finally discusses the openings of future work.

1 State of Art

1.1 Introduction

Thoracic injuries happen frequently in various frameworks of high velocity impact biomechanics such as road traffic crashes, sports and ballistic impacts [1–4]. Fig. 1.1 shows the injury locations and severities of drivers in frontal car crashes by Cuerden et al. [5], it can be noted that the thorax part is one of the most injured body areas and can lead to severe and life-threatening injuries. As is introduced in general introduction, rib fractures and lung injuries are the most frequent thoracic injuries, and rib fragments can perforate the lung pleural surface, lung parenchyma, liver or heart, which may cause severe injuries such as pneumothorax and hemothorax or even death [6–8]. Specifically, the elderly are more likely to encounter rib fractures and serious complications, and they need longer recovery time or even face higher mortality owe to the decreased recovery capacity [9,10]. Therefore, this thesis concentrates on the investigation of dynamic responses of human tissues especially ribs and soft tissues under high velocity impacts using finite element modeling, which can help better understand the mechanisms of corresponding injuries and is useful for design, evaluate and optimizing protecting equipment.

Biomechanical experiments applying Postmortem Human Subjects (PMHS) and anesthetized animals are generally conducted to study human injuries under high velocity impacts [11,12]. However, the use of human or animal cadavers needs high costs and has ethical issues [13]. Besides, Anthropomorphic Test Devices (ATDs) are typically applied for injury prediction in impact biomechanics. But ATDs only represent gross human body so that they are not able to predict injuries of definite parts like individual rib fractures. Also, it takes time to redesign, calibrate and validate ATDs with updated human response data [14].

Consequently, numerical simulations such as Finite Element (FE) method have been used as alternative methods with the development of computer capacity. FE models can not only predict global human behaviors but also definite parts of human hard and soft tissues by precise modeling. In the past decades, various biomechanical FE models have been developed and play an important role in investigating injuries in biomechanical impacts [15], including full human body models and isolated thorax models. The Total Human Model for Safety (THUMS) [16], the Human Model for Safety (HUMOS) [17], the Global Human Body Models Consortium (GHBMC) [18] and the University of Waterloo Human Body Model (UW-HBM) [19] are some common full human body FE models. The first human FE thorax models were developed by Roberts and Chen [20],

and by Sundaram and Feng [21] in the 1970s. More refined models were developed in the following decades by Huang et al. [22], Plank et al. [23], Lizee et al. [24], Ruan et al. [2] and Kimpara et al. [25]. More recently, a biofidelic Hermaphrodite Universal Biomechanical yx human torso model (HUByx) was proposed by Roth et al. [26] and was used to replicate real-world accidents. In addition, in order to better understand dynamic behaviors of ribs and predict the occurrence of rib fractures, several isolated rib models were developed and simulated [27–32].

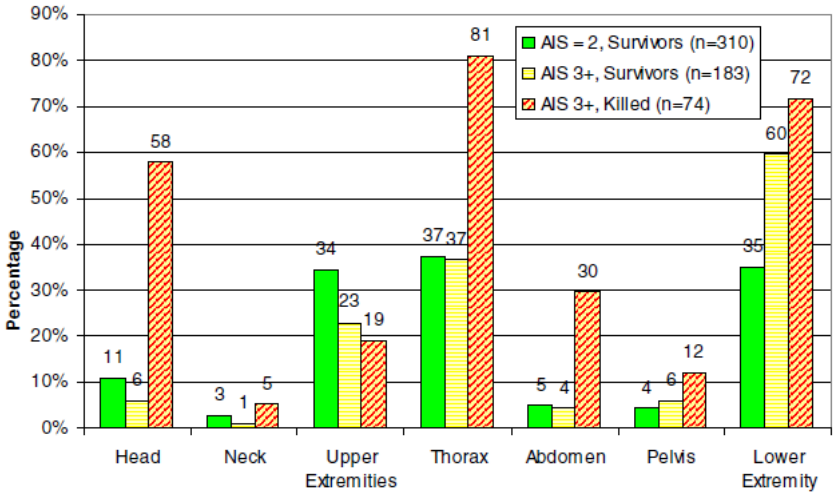

Figure 1.1: Injury regions and severity of drivers in front impact crashes, extracted from [5].

Therefore, the first chapter presents the literature review of the research background of this thesis. Firstly, the biomechanics of human thorax is introduced where human thorax anatomy is presented first. Then, soft tissues and hard tissues (especially ribs) of human thorax are introduced respectively, including soft organs, rib anatomy, material properties of soft and hard tissues, soft tissue injuries and rib fractures and common biological substitutes. Subsequently, the literature review of experimental and numerical studies of impacts on soft tissues and ribs are carried out, respectively. And we briefly summarize the bibliographical study at the end of this chapter.

1.2 Biomechanics of Human Thorax

1.2.1 Human Thorax Anatomy

The human thorax part is located between the neck and abdomen parts of the human trunk. The human thorax is consist of the thoracic cage, internal soft organs and soft tissues such as muscles, fascia, skin and blood vessels. The thoracic cage shown in Fig. 1.2 supports human thorax by its skeletal framework, and sustains the pressure from breathing process. The thoracic cage mainly includes sternum, vertebrae and ribs which

are linked by intervertebral discs and costal cartilage. Also, soft tissues like muscles, fascia and skin are supported by thoracic cage as well. Internal soft organs within the thoracic cage include the heart, lungs and great vessels, which are principal respiratory and circulatory organs [33].

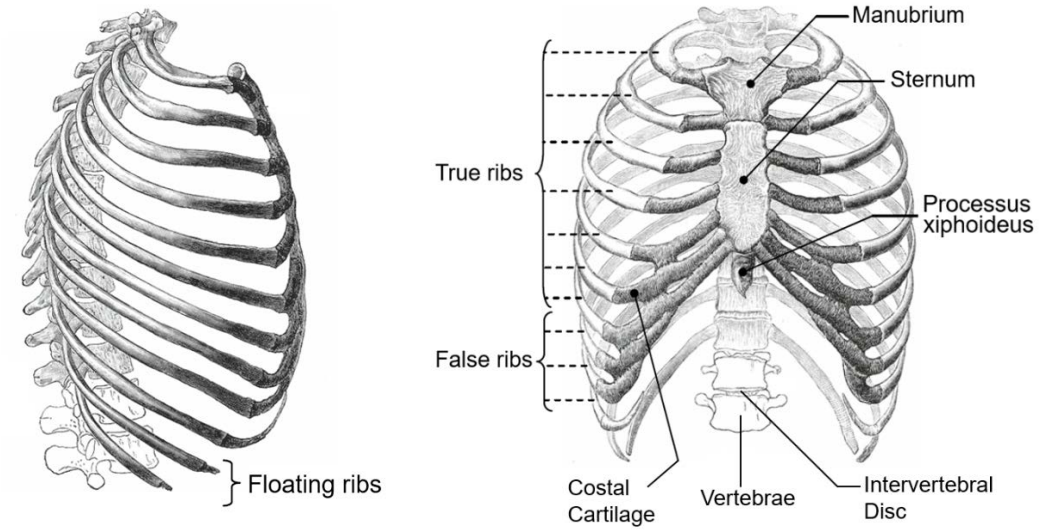

(a) Lateral view (b) Front view

Figure 1.2: Lateral (a) and front (b) view of thoracic cage, adapted from [34].

1.2.2 Soft Tissues

1.2.2.1 Soft Organs

As is shown in Fig. 1.3, the main respiratory and circulatory organs are located within the thoracic wall i.e. the lungs, the trachea, the heart and great vessels. Thereinto, the heart and lungs are two vital internal soft organs in human thorax, and are also vital organs of human beings second to brain.

The left and right lungs are human beings' principal respiratory organs and take up most space of the thoracic cavity. The left lung is consist of two lobes (upper and lower) and the right lung has three lobes (upper, middle and lower). The lungs' function is to exchange oxygen and carbon dioxide between human body and air. Each lung is consist of ten bronchopulmonary segments, and each segment has a segmental bronchus (Fig. 1.4). And the segmental bronchus divides into respiratory bronchioles where the gas exchange takes place at microscopic passages called pulmonary alveoli [35]. The heart is located between the two lung chambers. It pumps the blood to entire human body, including two kinds of circulations i.e. systemic and pulmonary circulation. The systemic circulation transfers oxygenated blood from pulmonary circulation to all tissues except for lungs and the pulmonary circulation pumps deoxygenated blood to

lungs [33,36].

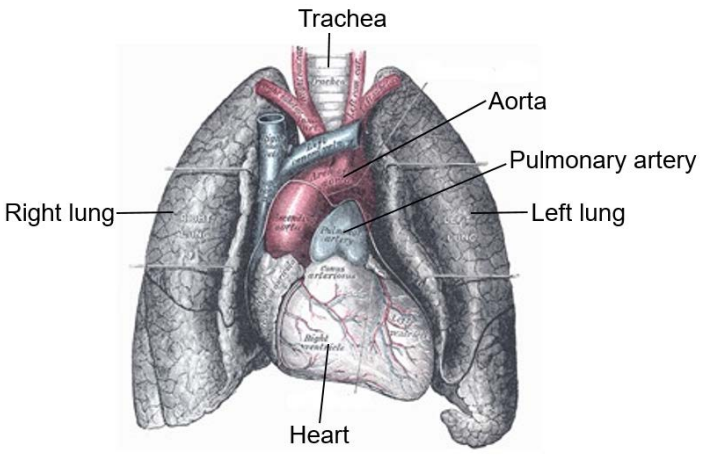

Figure 1.3: Illustration of thoracic soft organs, adapted from [34].

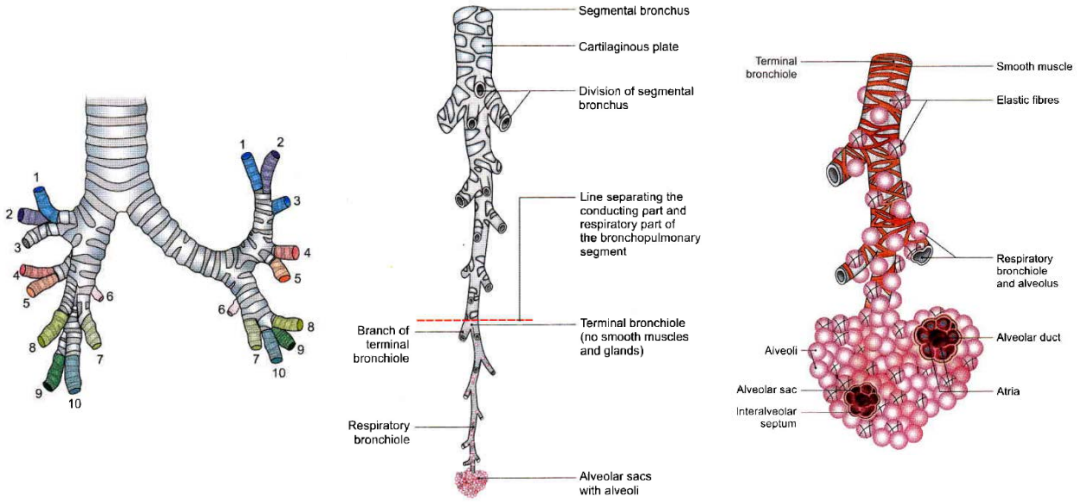

(a) (b) (c)

Figure 1.4: (a) Bronchopulmonary segments of lungs; (b) Bronchial tree; (c) Alveolar structure [33].

1.2.2.2 Common Soft Tissue Substitutes

In the past decades, it has seen increasing interests for researchers to use various soft tissue simulants as human tissue substitutes to investigate human soft tissue behaviors in impact biomechanics [37–43], which can avoid practical and ethical issues in human cadavers' experiments. Common human soft tissue substitutes used in the research field include rubber, clay, ballistic gelatin and polymer.

Silicone rubber is made of silicone, hydrogen, carbon and oxygen, and has a good balance of mechanical and chemical properties. Despite of the excellent stability and little dependence on temperature, silicone rubbers are commercially unavailable

because of lacking of convenient transparency and high costs [39,44]. Fig. 1.5 displays silicone rubber impacted by a flat-bottomed punch. Clay has been used to measure the deformation depth in blunt ballistic armor test for predicting the risk of trauma, nevertheless, it is not feasible to assess dynamic deformation of clay [43,45]. Fig. 1.6 illustrates the clay brick impacted by spherical steel spheres.

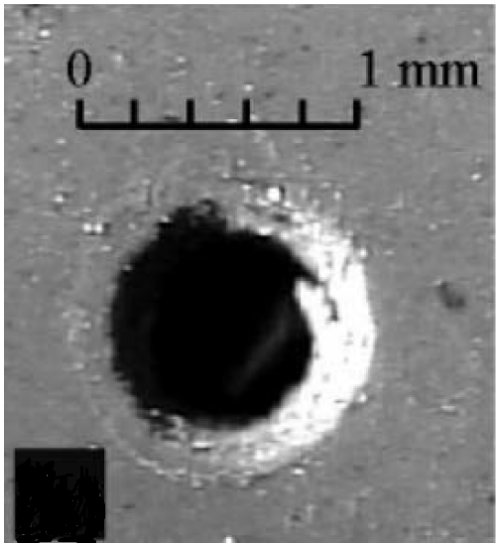

Figure 1.5: Silicone rubber impacted by a flat-bottomed punch [44].

Figure 1.6: Illustration of clay brick impacted by spherical steel spheres [43].

Compared to silicone rubber and clay, ballistic gelatins are more widely used as soft tissue simulants in biomechanics like penetrating impact, blunt impact and blast loading contexts [46–50]. There are two typical ballistic gelatins according to the mass fraction, i.e. 10% gelatin known as Fackler gelatin and 20% gelatin known as NATO gelatin, and the rest is composed of water [51–53]. The ballistic gelatin allows visualization and representation of the impact processes due to its transparency and imaging techniques. Fig. 1.7 exhibits the ballistic gelatin block under impacts and the size of the temporary cavity is measured by high-speed camera. However, previous studies have revealed the disadvantages of ballistic gelatins such as aging time, significant temperature sensitivity and humidity instabilities, which make the mechanical analysis complicated due to the alterations of their mechanical properties [53,54].

In contrast, the synthetic polymer SEBS (Styrene-Ethylene-Butylene-Styrene) gel (Fig.

1.8) highlights a number of practical benefits against ballistic gelatin i.e. environmental stability, reproducibility and mechanical consistency [55,56]. It is a triblock copolymer and the manufacturing process of SEBS gel is straightforward. It can be obtained by mixing SEBS powder and mineral oil and does not need complicated equipment, and it is easy to recyclable through melting. It was also revealed that SEBS gel has a similar backface deformation with 20% ballistic gelatin by ballistic impact tests [55]. Consequently, researchers adopted the synthetic polymer SEBS gel as soft tissue substitutes in place of ballistic gelatin in biomechanics in recent years [55–60]. For example, a systematical research of changing the toughness and modulus of a synthetic polymer SEBS gel was performed by Mrozek et al. [56], in order to investigate the relationship between mechanical properties and penetration depth under ballistic impacts. Bracq et al. [58] experimentally characterized the strain rate dependent mechanical properties of a 30% synthetic polymer SEBS gel through tensile and compressive tests at diverse strain rates. Therefore, in this thesis we took SEBS gel as soft tissue simulant and proposed a novel strain-rate-dependent elasto-hydrodynamic constitutive law of SEBS gel.

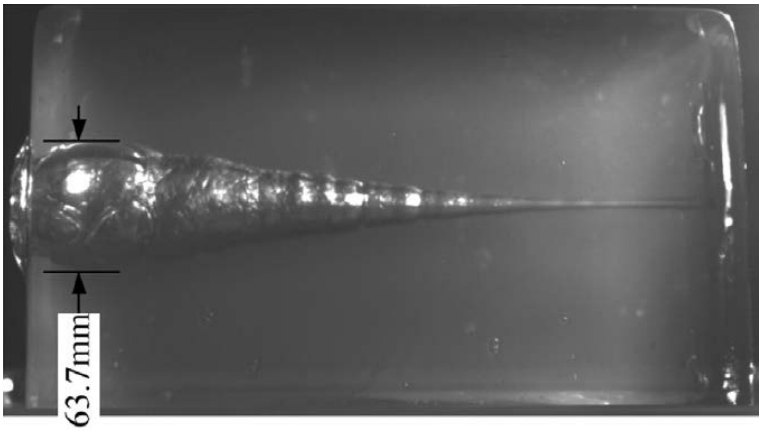

Figure 1.7: Representation of ballistic gelatin block under impacts [47].

Figure 1.8: Illustration of prototype SEBS gel block [55].

1.2.2.3 Material Properties

Numerical tools such as finite element methods have been widely applied in biomechanics, the key issues are developments of appropriate constitutive material laws which can describe the main material responses and their implementation in FE codes. Therefore, it is of increasing importance to study the material properties of human soft tissues and soft tissue simulants. The mechanical properties of the two vital internal soft organs i.e. lungs and the heart are generally represented by strain energy functions [61]. As is mentioned before, it has seen increasing interests for researchers to use soft tissue simulants as human tissue substitutes to investigate human soft tissue behaviors in impact biomechanics.

Therefore, many studies concentrated on the development of constitutive models of soft tissue simulant [38,53,62–65]. Generally, tensile and compression tests are conducted to measure the material properties. Some show viscoelastic, hyperelastic and visco-hyperelastic behavior. For example, Moy et al. [38] investigated the constitutive and failure behavior of 20% ballistic gelatin under tensile loading at different strain rates. Fig. 1.9 presents the tensile stress-strain relationship of ballistic gelatin and the flow stress increases with the increase of strain rate, which indicates that the gelatin is rate dependent. Cronin and Falzon [53] measured the mechanical properties of 10% ballistic gelatin applying compression test apparatus, and the Neo-Hookean hyperelastic constitutive model was used to characterize the material properties. For high strain rates, the well-known Split Hopkinson Pressure Bar (SHPB) apparatus was employed to conduct dynamic compressive tests of ballistic gelatins and obtain dynamic stress-strain response [63,64]. Fig. 1.10 shows the true compressive stress-strain relationships of 20% ballistic gelatin under various high strain rates conducted by Salisbury and Cronin [63], and it can be considered to have a hyperelastic behavior with strain rate dependence.

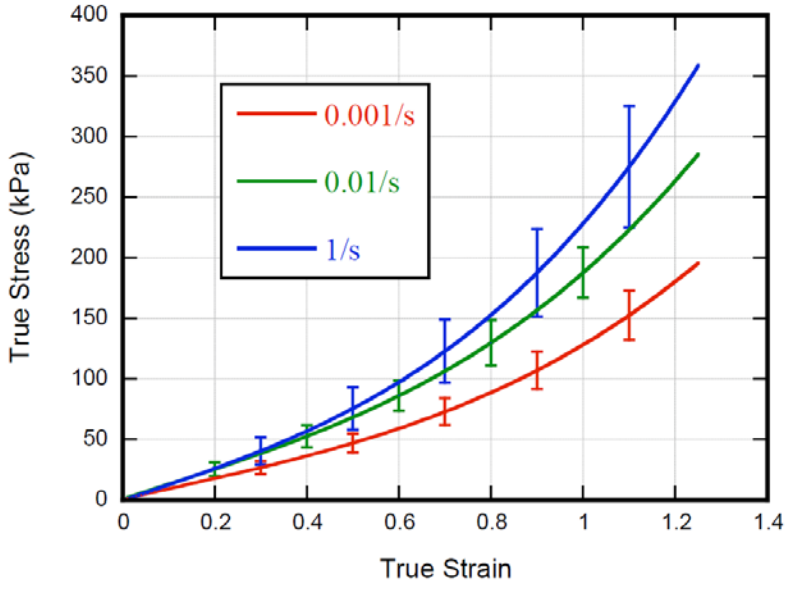

Figure 1.9: Stress-strain relationship of ballistic gelatin under tensile loading [38].

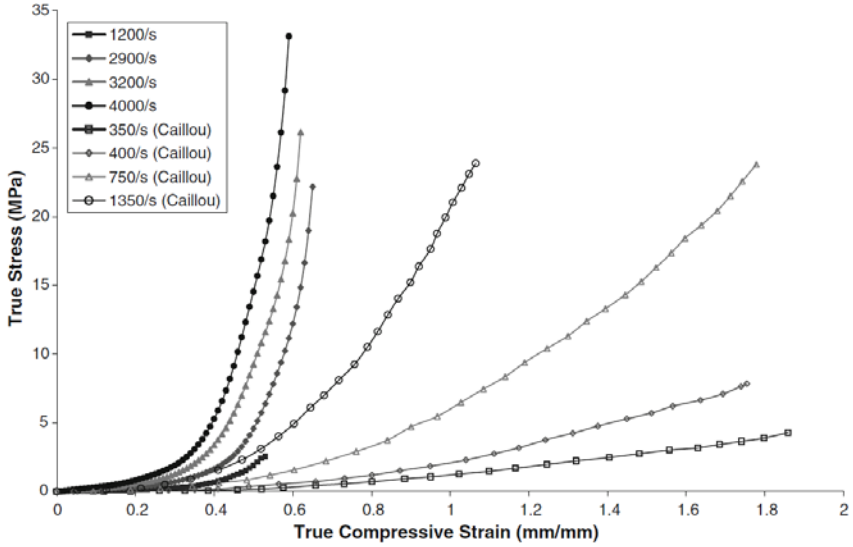

Figure 1.10: Compressive stress-strain relationship of ballistic gelatin at various high strain rates [63].

In recent years, the mechanical properties of synthetic polymer SEBS gel were investigated by researchers. Mrozek et al. [56] characterized SEBS gel using tensile and compression tests at low strain rates and the stress-strain data were fitted by hyperelastic constitutive models. Bracq et al. [58,59] also studied the mechanical behavior of a 30% SEBS gel at diverse strain rates through tensile tests and compressive experiments using SHPB apparatus, a visco-hyperelastic material law based on the Mooney-Rivlin model was proposed. Fig. 1.11-1.12 show the true stress-strain curves from tensile tests and engineering stress-strain relationships under dynamic compressive tests at various strain rates conducted by Bracq et al. [58]. Besides, Mauzac et al. [55] found that the SEBS gel exists a linear elastic mechanical characterization on its surface. Also, hydrodynamic behavior of the gelatins was considered to be more suitable at least at the beginning of penetration events [66,67], and it can be represented by an equation of state.

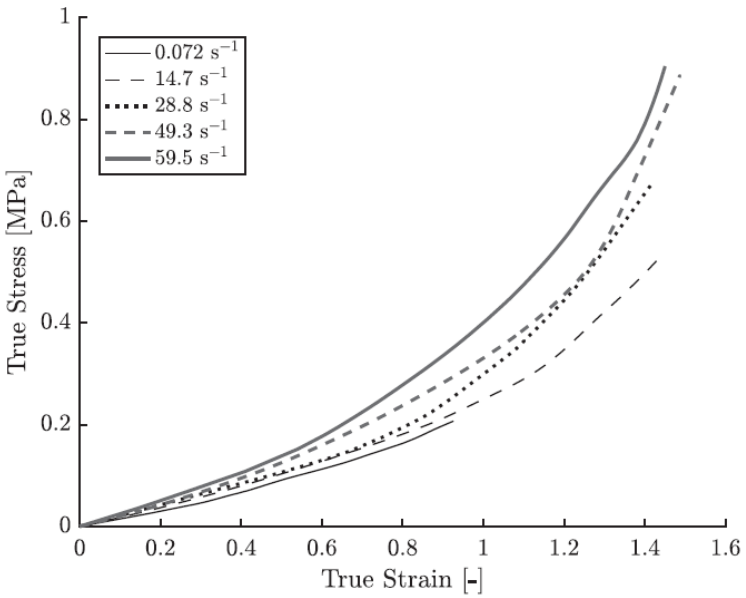

Figure 1.11: True stress-strain curves of the SEBS gel at different strain rates, extracted from [58].

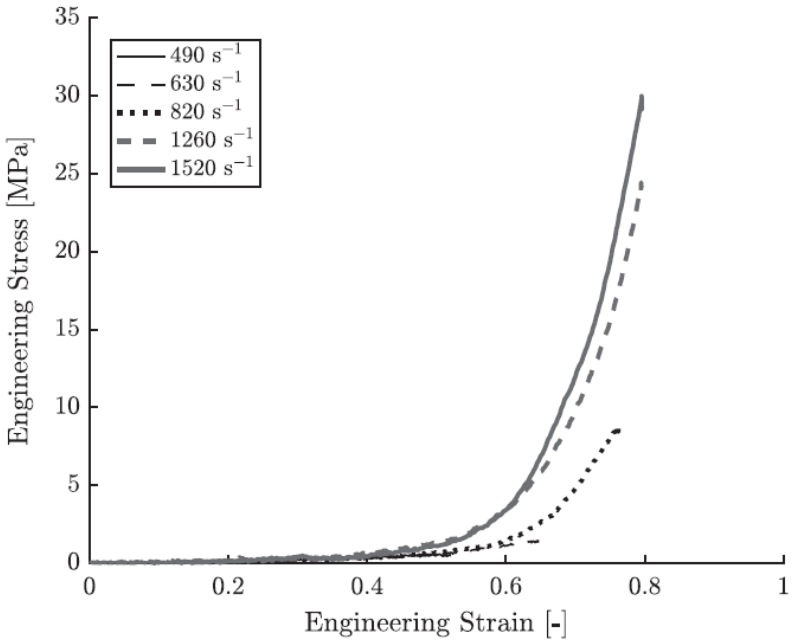

Figure 1.12: Engineering stress-strain relationships of SEBS gel under dynamic compressive tests at various strain rates, extracted from [58].

1.2.2.4 Soft Tissue Injuries

Thoracic injuries happen frequently in various frameworks of high velocity impact biomechanics such as road traffic crashes, sports and ballistic impacts, and can be life-threatening. Soft tissue injuries are main injuries apart from rib fractures among thoracic injuries, and rib fragments can perforate the lung pleural surface, lung parenchyma, liver or heart, which may cause severe injuries such as pneumothorax and

hemothorax or even death.

Lung injuries are the most frequent soft tissue injuries in human thorax part, and can cause multiple organ failure [68,69]. Pulmonary laceration, pneumothorax, hemothorax and pulmonary contusion are main lung injuries. Fig. 1.13 shows a thoracic CT image of pulmonary laceration (white arrow) and pulmonary contusion (black arrow). Pulmonary laceration occurs when the lung is torn at a large scale and a ruptured lung can release air and blood. Pneumothorax and hemothorax happen when the space between the lung and thoracic wall is filled with air and blood respectively. Pulmonary laceration can also lead to pulmonary contusion, where the alveoli is damaged and collapsed and filled with fluid, and may result in inflammatory reaction. Moreover, the possibility of Acute Respiratory Distress Syndrome (ARDS) increases if the contused lung volume is over 24% [70].

Heart laceration and contusion can be caused by contact the deformed hard tissues such as fractured ribs. Such heart injuries can affect the functionality of heart and lead to defective hear rhythm or even cardiac arrest [71]. Besides, similar injury types occur for great vessels and the aorta in human thorax under high velocity impacts, and the loss of blood can be life-threatening due to the rupture of the aorta [72].

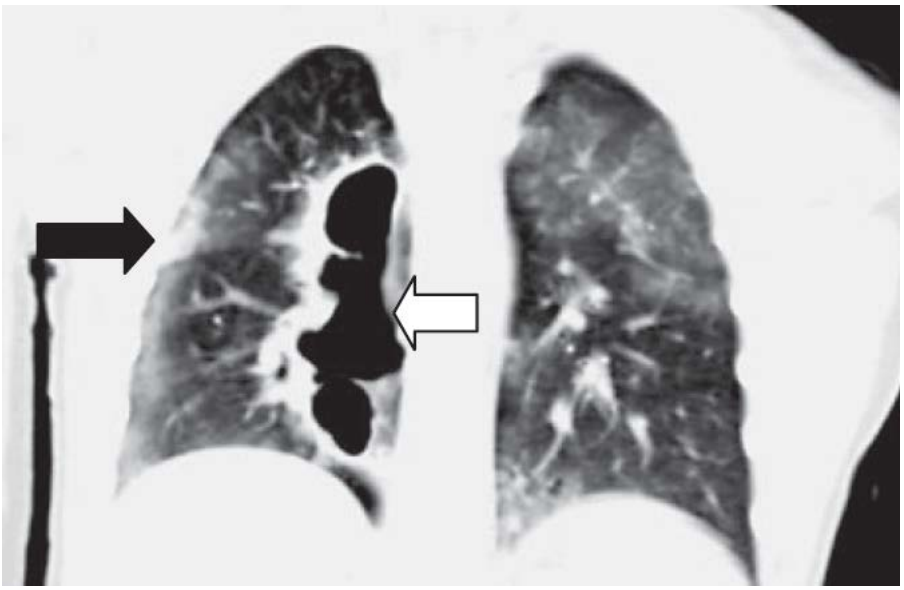

Figure 1.13: Thoracic CT image of pulmonary laceration (white arrow) and pulmonary contusion (black arrow) [73].

The Abbreviated Injury Scale (AIS) based on anatomic injuries is widely used to describe the different injury severities [74]. The AIS has a classification of six levels: from AIS 1 (minor) to AIS 6 (fatal) according to the threat to life, where level 1 is assigned to minor injury and level 6 means fatal injury. Table 1.1 displays the soft tissue injury in human thorax corresponding to different levels of AIS.

Table 1.1: Thoracic soft tissue injuries with corresponding AIS levels, extracted from [72].

	AIS	Soft tissue injury
Minor	1	Skin abrasion, contusion, laceration
Moderate	2	Major skin laceration, partial thickness tear, bronchus
Serious	3	Minor heart contusion, unilateral lung contusion
Severe	4	Severe heart contusion, intimal tear of aorta
Critical	5	Major aortic laceration, heart perforation, ventricular heart rupture
Fatal	6	Aortic laceration with haemorrhage

1.2.3 Hard Tissues

1.2.3.1 General Introduction of Bones

Human thorax is supported by the skeletal framework of the thoracic cage. The bone tissues within thoracic cage include sternum, vertebrae and ribs which are linked by intervertebral discs and costal cartilage as shown in Fig. 1.14.

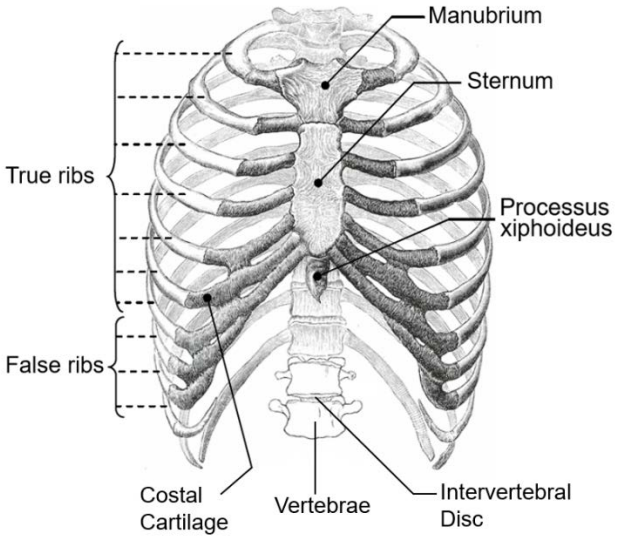

Figure 1.14: Anterior view of human thoracic cage, adapted from [34].

The sternum locates at the anterior end of the thoracic cage. It is a flat bone, constituting the anterior median part of the thoracic cage, and articulates with the first 7 pairs of ribs.

As is shown in Fig. 1.15, it consists of manubrium, body and xiphoid process. The upper part is called manubrium, it is quadrilateral in shape. It is the strongest and thickest part of the sternum. The middle part which resembles the blade is the body, it is thinner, longer and narrower than the manubrium. And the lower part gradually forming the point of the sword is called xiphoid process, it is the thinnest and smallest part of the sternum. It is cartilaginous in the youth but its upper end becomes ossified in adults [33].

The 12 thoracic vertebrae and the intervening intervertebral discs are at the posterior end of the thoracic cage, the lateral view of typical thoracic vertebrae is exhibited in Fig. 1.16. The thoracic vertebrae are identified by the demi-facets on the sides of vertebral bodies which articulate with the corresponding ribs.

Also, there are 12 ribs on each side of the thoracic cage (Fig. 1.14) and each rib articulates posteriorly with the thoracic vertebral column. Thereinto, the first 7 pairs of ribs articulate anteriorly with the sternum through corresponding costal cartilages and they are called true or vertebrosternal ribs. The 8th, 9th and 10th ribs are called false or vertebrochondral ribs, the costal cartilage end of these three ribs joins the next higher costal cartilage. The 11th and 12th ribs are known as floating or free ribs as they are free at the anterior extremity [33].

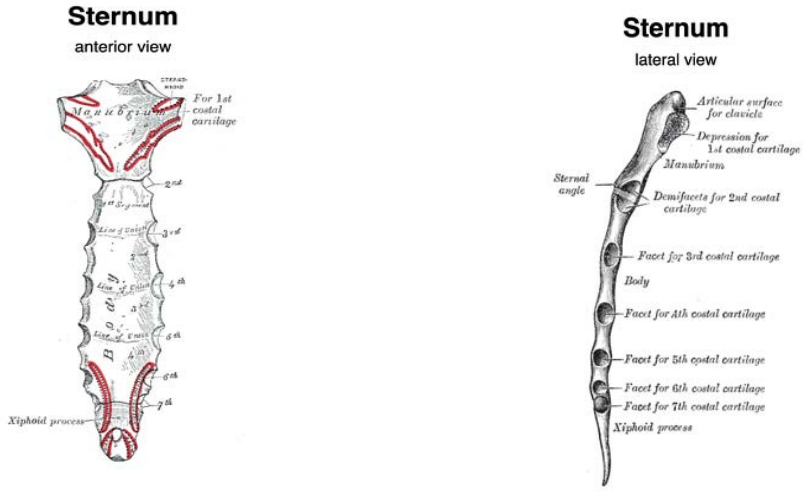

(a) Anterior view (b) Lateral view

Figure 1.15: Anterior (a) and lateral (b) view of sternum [34].

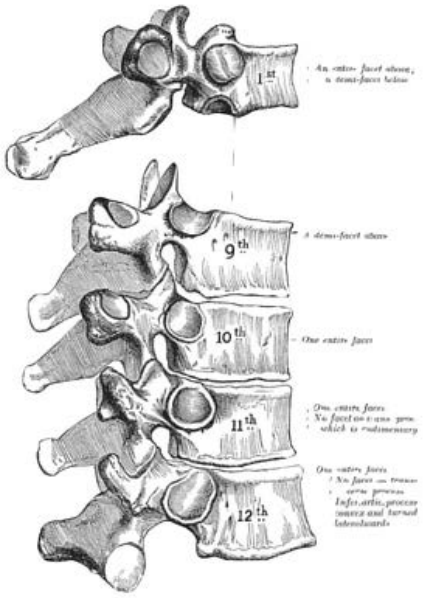

Figure 1.16: Lateral view of typical thoracic vertebrae [34].

Bone tissue is a biological collagen based tissue composed of organic materials, inorganic materials and water. Bone is an essential element of human musculoskeletal system and has a lightweight cross sectional construction which is able to stand heavy loads, therefore it gives structural support to other tissues. Bone consists of a dense cortical bone shell outside and filled with light trabecular bone inside as is shown in Fig. 1.17.

The cortical bone is also referred to as compact bone, it has a more mineralized and less porous structure compared to the trabecular bone. Cortical bone is composed of the units called osteons. Each osteon has a cross section in which the cylindrical layers of lamellae enclose the Haversian canal. Inside the Haversian canal are blood vessels, nerves and lymph vessels [75].

The trabecular bone is less mineralized and more porous in contrast to cortical bone, therefore it is also called spongy or cancellous bone. It is composed of interconnecting trabeculae.

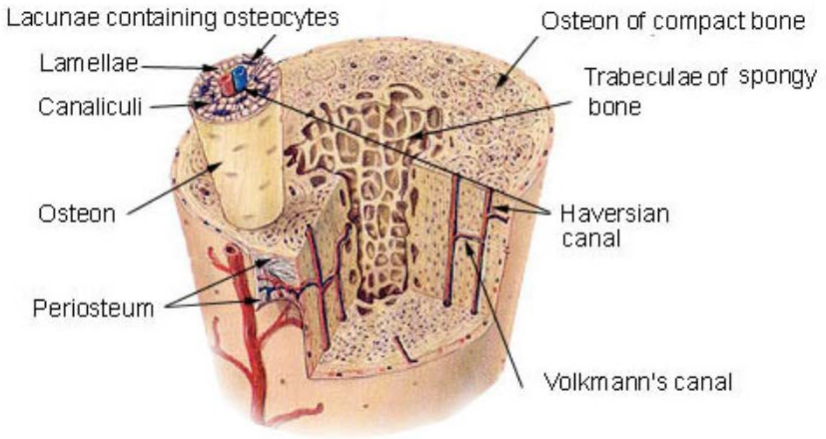

Figure 1.17: Illustration of a cross section of a long bone, extracted from [75].

1.2.3.2 Rib Anatomy

As is mentioned in the previous section, there are 12 ribs on each side of the thoracic cage. A typical rib is composed of three anatomical regions as illustrated in Fig. 1.18, i.e. head, neck and body. Head locates at the anterior extremity of the rib, where two articular facets are separated by a wedge. The rib articulates with corresponding thoracic vertebra through the articular facets. Neck connects the rib head with the tubercle, and the tubercle articulates with corresponding thoracic vertebra via its articular facet. Body of the rib is flat and curved with cutaneous and pleural surfaces. The cutaneous surface is located closed to the skin, while the pleural surface is faced with the internal organs and protects them from external damage. The costal groove is located at the pleural surface.

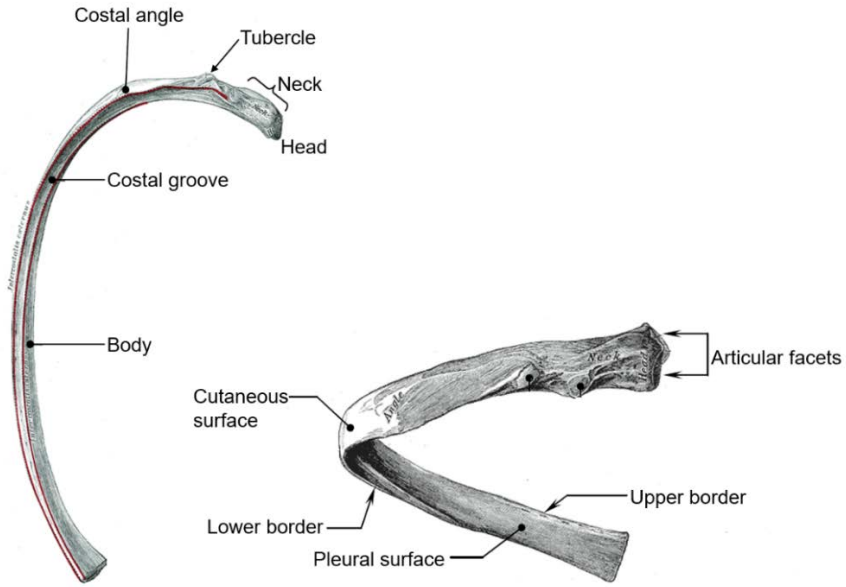

Figure 1.18: Structure of a typical human rib, adapted from [34].

The ribs are located in the ribcage with an angle to the transverse plane of thorax as illustrated in Fig. 1.2. According to the morphological terms, each rib is different because the lengths and angles of orientation are different. The length of the ribs increases gradually from the 1st to the 7th rib and then decreases from the 8th to the 12th rib. Similarly, the angle of orientation increases from the 1st to the 9th rib and thereafter it decreases to the 12th rib. The first two ribs together with the last three ribs are atypical ribs due to their special features, and the 3rd to the 9th ribs are typical ribs. Besides, the upper two ribs and the two floating ribs are the least commonly fractured ribs. Therefore, a middle rib is normally used to analyze the characteristics and fractures of ribs [33,34].

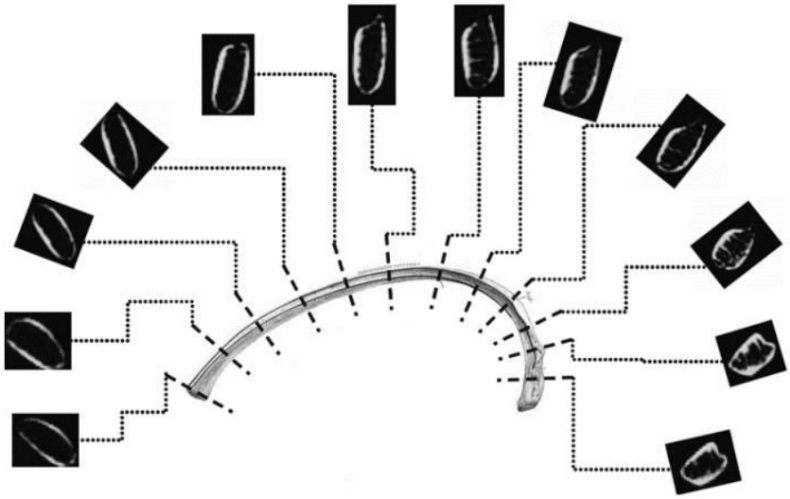

Figure 1.19: Transition of the rib cross section geometry, extracted from [76].

The cross section geometry of a rib has a transition feature, it has a circular shape from the head to the neck and translates to an elliptical cross section from the neck to the rest of the whole rib body as shown in Fig. 1.19. Therefore, a rib can generally be approximated to have an elliptical cross section. Fig. 1.20 exhibits the cross section of a representative human rib photographed by Granik and Stein [77], and the CT scan of the cross section of a 5th rib is shown in Fig. 1.21. It is obvious that the cross section of a rib is composed of two bone tissue, i.e. outer cortical bone layer and a more porous trabecular bone inside.

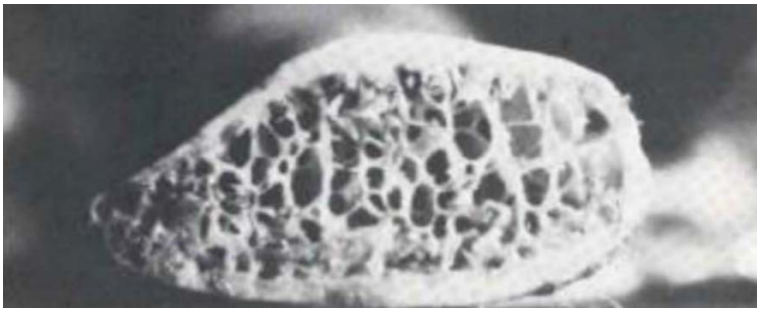

Figure 1.20: Photograph of the cross section of a representative human rib, extracted from [77].

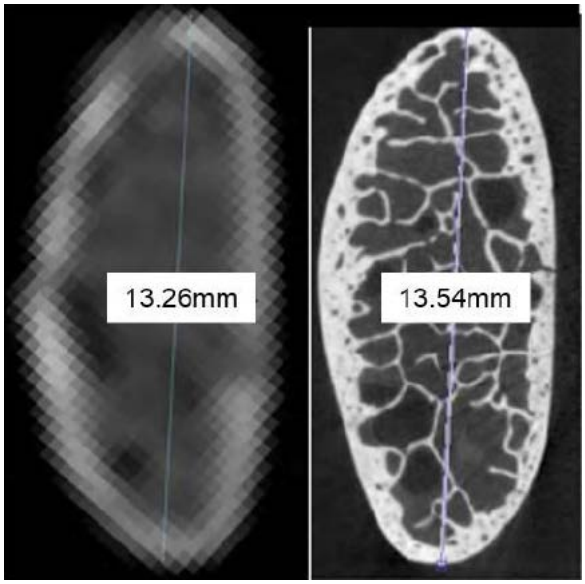

Figure 1.21: CT (left) and μCT (right) scan of the cross section of a 5th human rib [78].

1.2.3.3 Common Human Rib Substitutes

The use of human cadavers is limited because of the high financial costs and ethical issues. Therefore, human ribs are not easy to obtain when conducting fracture experiments under high velocity impacts. On the other hand, animal cadavers and animal ribs are readily to purchase from local butchers. Thereinto, porcine ribs are commonly used as human rib substitutes as they have similar geometrical and anatomical characteristics with human ribs [79,80].

Consequently, researchers have conducted some studies on rib fractures applying porcine ribs in recent years. For example, Christensen et al. [81,82] first examined the rib fracture patterns using eleven pigs exposed to blast loadings (Fig. 1.22), and then performed manual bending force fracture testing on 46 pig ribs, butterfly fractures (Fig. 1.23) were found to be a possible indicator of blast trauma. Margaret [83] investigated porcine rib fracture patterns under three different loading modes i.e. end-compression loading, low velocity three-point bending and dynamic loadings, which verified the assumption that porcine ribs are a useful substitute for the study of human rib fracture patterns, fracturing in a similar location and mode as human ribs. More recently, experimental and numerical studies of porcine ribs subjected to dynamic 3PB loadings applying SHPB apparatus were conducted in order to help predict human rib fractures by Ayagara et al. [31].

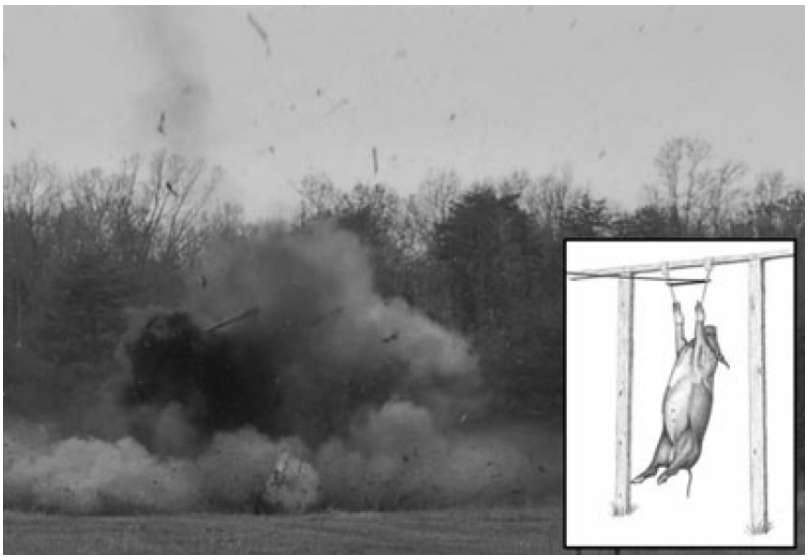

Figure 1.22: Schematic of pig specimen under blast loading, extracted from [82].

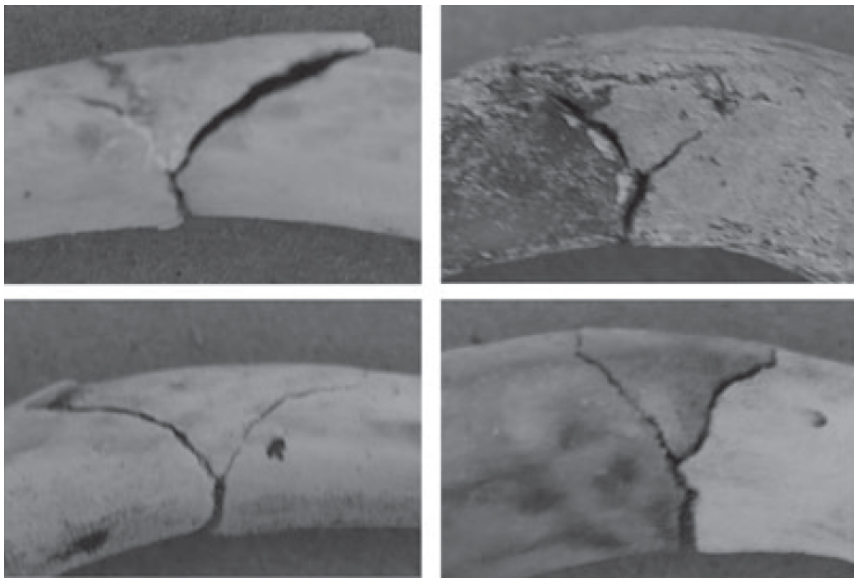

Figure 1.23: Representation of butterfly fractures of porcine ribs [82].

1.2.3.4 Material Properties of Ribs

As finite element models are increasingly used to evaluate the thoracic injuries, the investigations of material properties of ribs help to develop appropriate constitutive laws which can be appropriately implemented in FE codes. Therefore, researchers have payed attention to the material properties of ribs for a better comprehension of the mechanical behaviors of ribs in the past decades. The bone cross section is composed of cortical bone and trabecular bone, cortical bone exhibits an elasto-plastic behavior while trabecular shows behavior similar to polymeric foams because of the difference of architectural arrangement [84,85]. Fig. 1.24 (a)-(b) shows typical mechanical properties of cortical and trabecular bone, respectively.

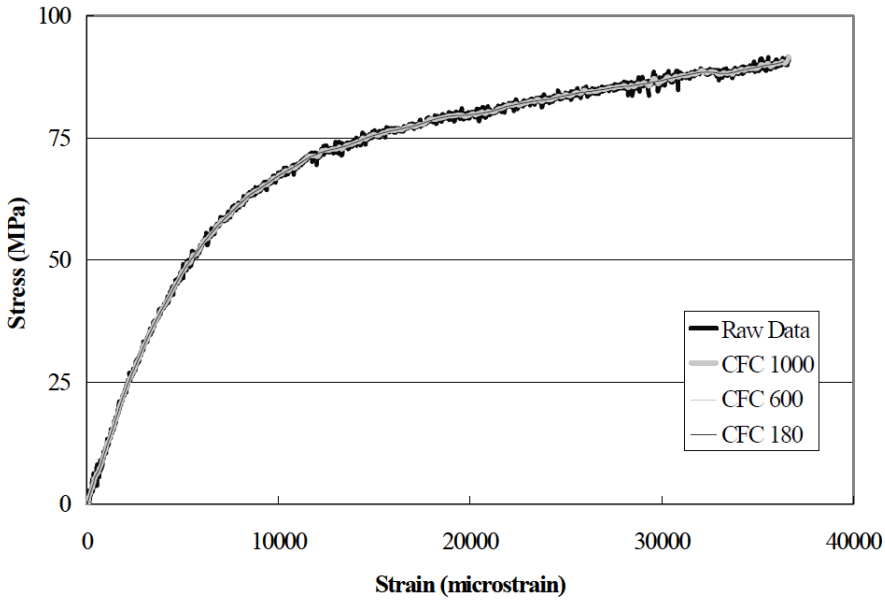

(a) Mechanical behavior of cortical bone, Kemper et al. [86].

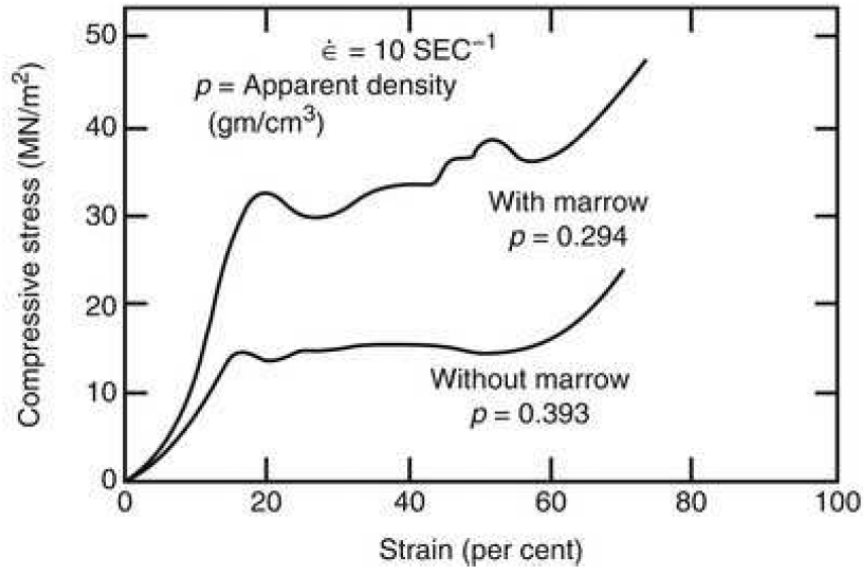

(b) Mechanical behavior of trabecular bone, Carter and Hayes [87].

Figure 1.24: Mechanical properties of cortical and trabecular bones.

Tensile and compression tests are commonly performed to characterize material properties of ribs. Numerous tensile coupon tests have been conducted to investigate the material properties of ribs [86,88–91]. For instance, Kemper et al. [86] first conducted 117 tensile coupon tests on human rib cortical bones from six cadavers and gave the complete stress-strain relationship. Subsequently, Kemper et al. [88] extended the sample quantity and found that rib cortical bone tensile material properties were not affected by rib level or region. Albert et al. [90] investigated tensile tests of 29 6th human rib cortical bones, the material properties of rib cortical bone were found to be

consistent with published data by Kemper. However, previous studies of rib cortical bone material properties are limited to tensile tests and no literature is about compressive material properties. Hence, Albert et al. [92] recently first performed compressive tests on human rib cortical bone and compared the compressive material properties with existing tensile data of the literature. They found that compression led to higher yield and ultimate stress while tension led to higher failure strain.

Additionally, many three-point bending tests on whole rib segments have been performed in order to investigate material properties of ribs applying linear elastic beam equations[77,93–95]. For instance, Granik and Stein [77] conducted three-point bending tests of 6th and 7th human ribs, they obtained the average elastic modulus and bending failure stress as 11.5GPa and 106MPa, respectively. Yoganandan and Pintar [93] tested material properties of 7th and 8th ribs from 30 human cadavers using three-point bending techniques, the average Young's modulus of 7th and 8th rib was 2.3GPa and 1.9GPa respectively. Moreover, Cormier et al. [94] performed three-point bending tests on a total of 52 rib samples of 2nd to 12th rib taken from anterior, lateral and posterior regions, respectively. The average modulus and ultimate stress were found to be 17.7GPa and 135.4MPa, respectively.

The effect of strain rate on the material properties of bones was also evaluated by many studies. McElhaney [96] conducted one of the first studies on the investigation of effects of different loading rates on human cortical bone, compression tests were performed on human femur, where the ultimate stress and modulus increase while the ultimate strain decreases with the increase of loading rate. The increase of Young's modulus with increasing loading rate was also reported by some other researchers [97–99]. However, Ferreira et al. [100] in contrary reported a decreasing effect and Pithioux et al. [101] found that cortical bone behavior was not relevant to strain rates. Besides, the effect of age, sex and other factors on material properties of bones were investigated as well [86,91,92,102,103].

In general, both the cortical and trabecular bones are modeled using elasto-plastic constitutive material model in FE numerical analysis [28–32,104,105]. Also, it is assumed that cortical bone shows isotropic hardening while trabecular bone obeys kinematic hardening [28,106].

1.2.3.5 Rib Fractures

Rib fractures are most common thoracic injuries, and rib fragments can perforate the lung pleural surface, lung parenchyma, liver or heart, which may cause severe injuries such as pneumothorax and hemothorax or even death. Specifically, the elderly are more likely to encounter rib fractures and serious complications, and they need longer recovery time or even face higher mortality owe to the decreased recovery capacity.

Therefore, understanding the patterns of rib fractures and prediction of rib structural responses and fracture location under high velocity impacts is essential.

Common rib fracture types comprise transverse, oblique, buckle, butterfly, partial butterfly and comminuted [107], and Fig. 1.25 shows various types of rib fractures. Rib fracture locations can be classified as anterior, anterolateral, posterolateral and posterior portions. Fig. 1. 26 displays the frequencies of fracture locations alongside rib curve length, it can be seen that most fractures occurred in the anterolateral portion of the rib i.e. at the anterior and middle sections [108].

Similar to soft tissue injuries, different rib cage injury severities are represented by the Abbreviated Injury Scale (AIS) based on anatomic injuries. Table 1.2 displays various rib cage injury severities corresponding to different levels of AIS.

Figure 1.25: Various types of rib fractures, (a) oblique, (b) transverse, (c) buckle, (d) comminuted, (e) butterfly, (f) partial butterfly, adapted from [83].

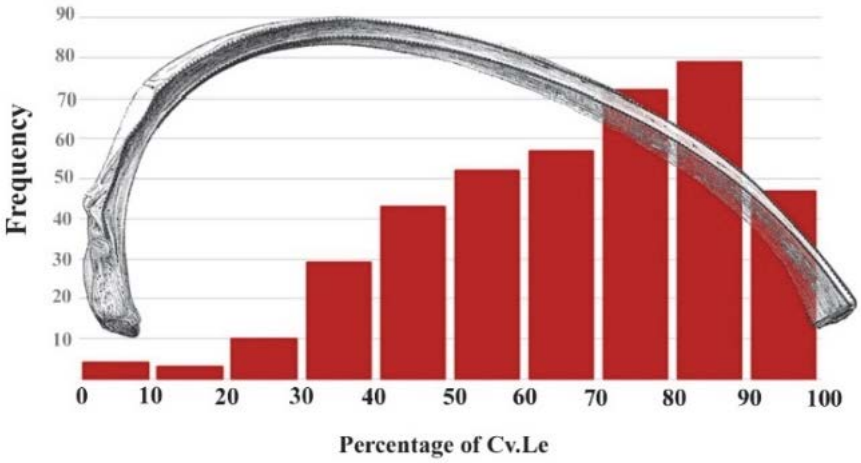

Figure 1.26: Distribution of rib fracture location frequency, extracted from [108].

Table 1.2: Rib cage injuries with corresponding AIS levels, extracted from [72].

	AIS	Rib cage injury
Minor	1	Single rib fracture
Moderate	2	2-3 rib fractures, sternum fracture
Serious	3	>4 rib fractures, 2-3 rib fractures with hemothorax or pneumothorax
Severe	4	>4rib fractures with hemothorax, pneumothorax or flail chest
Critical	5	Bilateral flail chest

1.3 Experimental Studies of Impacts on Soft Tissues and Ribs in the Literature

1.3.1 Experiments on Common Soft Tissue Substitutes

In the past decades, it has seen increasing interests for researchers to use various soft tissue simulants as human tissue substitutes to investigate human soft tissue behaviors in impact biomechanics, which can avoid the drawbacks of the use of human cadavers because of the high financial costs and ethical issues. As is introduced in Section 1.2.2.2, among the human soft tissue substitutes used in the research field, the ballistic gelatin is more widely used and the synthetic polymer SEBS gel is adopted by researchers in place of ballistic gelatin in recent years because of a number of benefits against the typical ballistic gelatin. Consequently, a literature review is conducted about experimental studies of impacts on ballistic gelatin and SEBS gel recently in the following two subsections.

1.3.1.1 Ballistic Gelatin

Fackler was the first to compare ballistic gelatin with living tissue and found that ballistic gelatin was an appropriate human tissue simulant by conducting comparative tests with porcine legs [109,110]. Ballistic gelatins were afterwards widely used as soft tissue simulants in biomechanics especially in the contexts of penetrating and blunt impacts [41,47,48,111–117]. The ballistic gelatin allows visualization and representation of the temporary and permanent wound profiles and provide an approximation about wounds in human tissues due to its transparency and imaging techniques.

For instance, Bree and Gotts [112] studied the compression wave propagation in ballistic gelatin shielded by aluminum plates and employed a twin peak theory. Bresson et al. [113] experimentally study the expansion dynamic behavior of 9mm Parabellum hollow point projectiles in 10% ballistic gelatin, they demonstrated that the knowledge of expansion law can be useful to investigate a gunshot in human body. Wen et al. [47] firstly conducted ballistic experiments of the impact penetration of steel spheres on 10% ballistic gelatin at moderate speeds in order to better understand the injury caused to human soft tissue, and subsequently studied the behind armor ballistic trauma [114], the temporary cavity was recorded by a high speed camera and it can be taken as evaluation of severity of injury caused by impacts. The schematics and photo of Wen's experimental setup is displayed in Fig. 1.27, and the temporary cavity profiles in ballistic gelatin under impact speed of 690m/s was shown in Fig. 1.28. Liu et al. [48] conducted non-penetration impact tests of handgun bullets on 10% ballistic gelatin block behind soft armor, a viscoelastic model was established to predict the shock wave attenuation in ballistic gelatin. Also, Luo et al. [41] investigated the transient pressure and transient cavity response of 10% ballistic gelatin in the context of behind armor blunt trauma (BABT) through pistol bullets impacting ballistic gelatin behind the soft body armor.

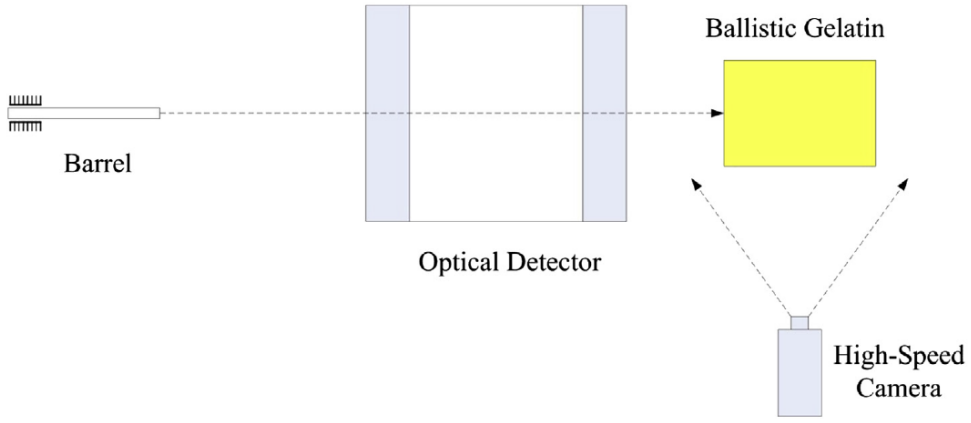

(a) Schematic of the experimental setup.

(b) Photo of the experimental setup.

Figure 1.27: Schematic and photo of the experimental setup of impact of steel spheres on ballistic gelatin, extracted from [47].

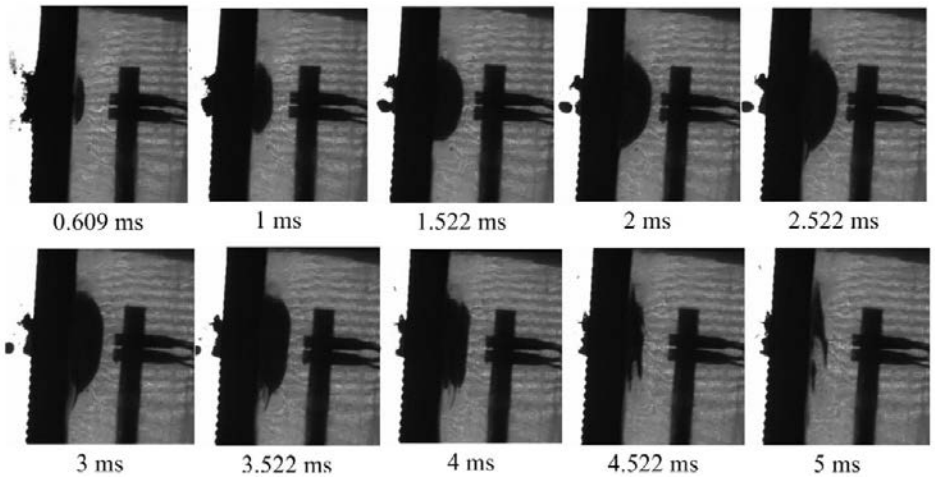

Figure 1.28: Representation of temporary cavity profiles in ballistic gelatin under impact speed of 690m/s in BABT experiments [114].

1.3.1.2 SEBS Gel

The synthetic polymer Styrene-Ethylene-Butylene-Styrene (SEBS) gel highlights a number of benefits against the typical ballistic gelatin such as environmental stability and mechanical consistency. In consequence, researchers adopted the SEBS gel as soft tissue substitute in place of ballistic gelatin in biomechanics impacts in recent years [55–58,118–120].

Mauzac et al. [55,57] measured the dynamic back face deformation of direct impacts of Less-lethal kinetic (LLKE) projectiles on SEBS gel, and afterwards conducted similar experiments in the context of BABT using SEBS gel, they found that SEBS gel can be effectively applied to assess the back face deformation. Fig. 1. 29 (a)-(b)

respectively shows the image of dynamic back face deformation of direct impact of LLKE projectile and BABT tests on SEBS gel in Mauzac's experiments. Mrozek et al. [56] characterized the mechanical properties of SEBS gel and investigated the relationship between mechanical properties and ballistic penetration depth in SEBS gel via tensile, compression and penetration tests. Moreover, Bracq et al. [58,59] characterized the strain rate dependent mechanical properties of a 30% synthetic polymer SEBS gel and performed blunt ballistic experiments to validate the developed constitutive law. More recently, they employed SEBS gel as a reference material to assess blunt ballistic impacts using a wide range of LLKE projectiles [119], Fig. 1.30 (a)-(b) exhibits the experimental setup and a photograph of the gel wall displacement captured by a high-speed camera during the impact of a rigid projectile. In addition, Veysset et al. [120] performed microscale high velocity impact experiments on SEBS gel using 10-24*um* diameter steel micro-particles with strain rates up to $10^7 s^{-1}$, which can be used in ballistic drug delivery applications.

(a) Impact of LLKE projectile on SEBS gel.

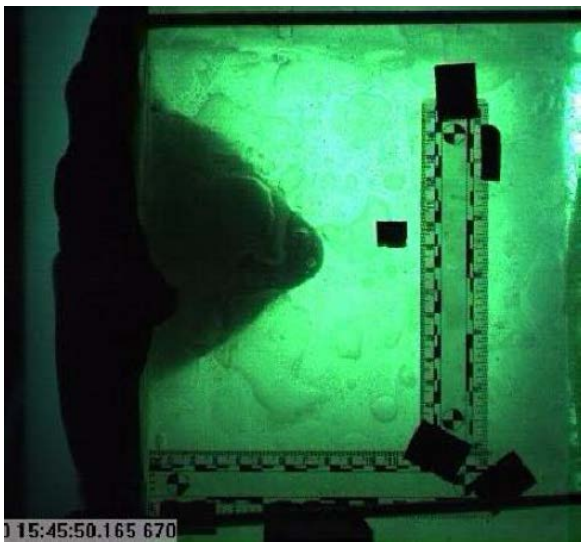

(b) BABT test on SEBS gel.

Figure 1.29: Image of dynamic back face deformation of direct impact of (a) LLKE

projectile and (b) BABT tests on SEBS gel [55,57].

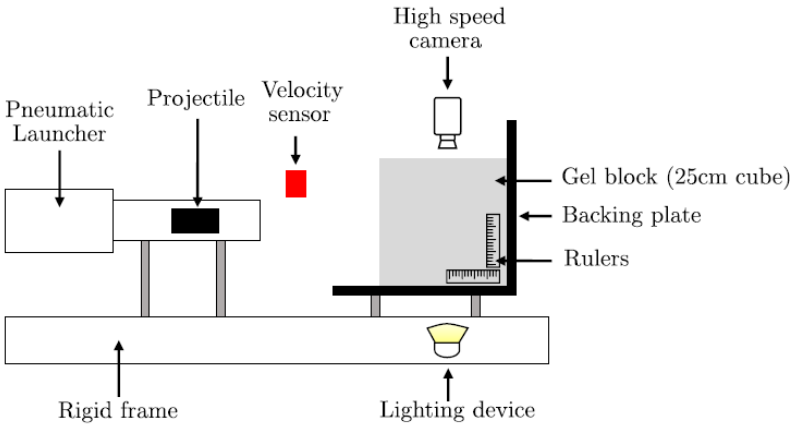

(a) Schematics of the experimental setup.

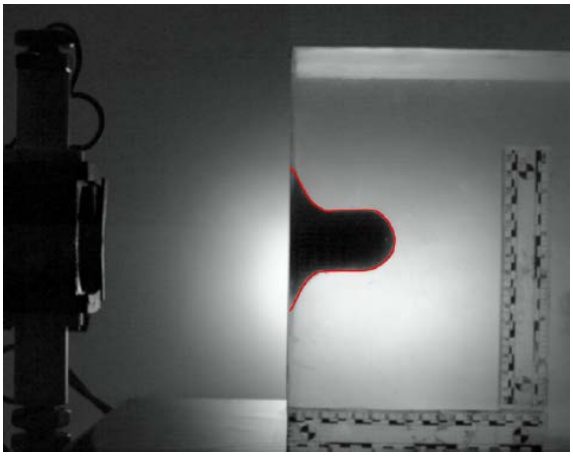

(b) Photograph of the gel wall displacement of SEBS gel during blunt impacts.

Figure 1.30: (a) Experimental setup and (b) a photograph of the gel wall displacement captured by a high-speed camera during the impact of a rigid projectile [119].

1.3.2 Experiments on Isolated Ribs

Rib fractures are most common thoracic injuries, and rib fragments can perforate the lung pleural surface, lung parenchyma, liver or heart, which may cause severe injuries such as pneumothorax and hemothorax or even death. Consequently, it is of importance to investigate the dynamic responses of ribs under dynamic loadings. To better understand the mechanisms of rib fractures and corresponding injury criterion, numerous experimental studies have been conducted on isolated ribs in the past decades, thereinto, three-point bending and anterior-posterior bending experiments on isolated ribs were performed to mimic real-world impact loadings like in motor vehicle crashes (MVCs). So the following two subsections review these two kinds of experimental studies conducted in recent years.

1.3.2.1 Three-point Bending

In the past decades, many experimental efforts have been done on isolated ribs under quasi-static or dynamic three-point bending (3PB) loadings [31,77,88,93,121–125]. For instance, one of the most cited works was conducted by Granik and Stein [77], they developed a quasi-static 3PB test methodology and tested the responses of 6th and 7th human ribs, the experimental setup is displayed in Fig. 1.31. Charpail [123] also performed quasi-static 3PB tests on human 6th, 7th and 8th ribs to study the structural responses and fractures of human ribs as shown in Fig. 1.32, where the author found that the thickness of cortical bone at a particular cross section affects bending stiffness and strength. Kimpara et al. [122] pointed out that there were differences of ribs responses and injury thresholds between female and male ribs via quasi-static 3PB tests. Moreover, Kemper et al. [88] investigated structural responses of human ribs by conducting 3PB experiments, and the results showed that there exists variations in structural responses with respect to anatomical region and rib level due to changes in local geometry.

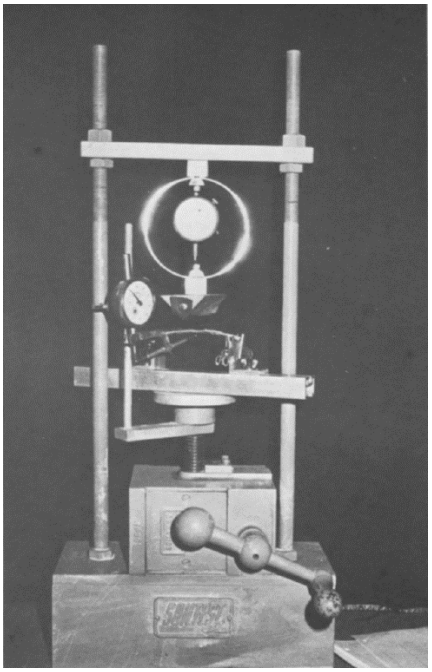

Figure 1.31: Experimental setup of 3PB test on ribs designed by Granik and Stein [77].

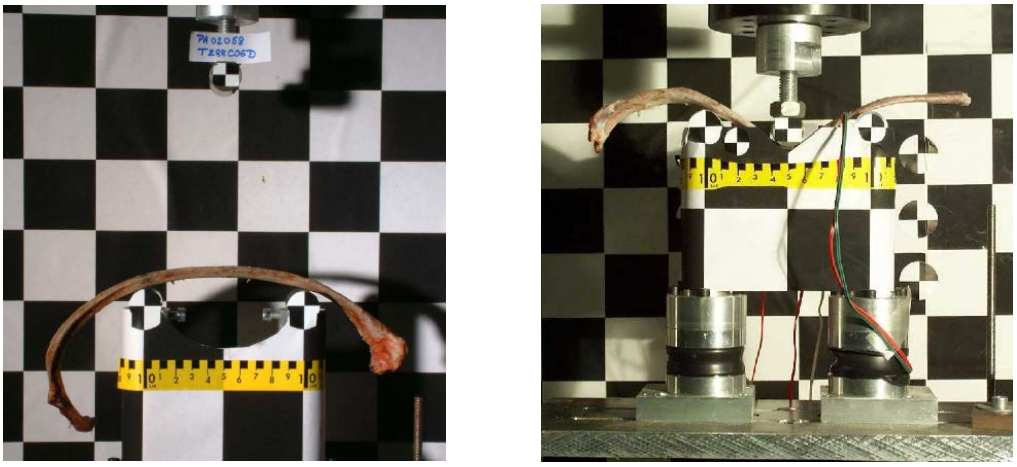

Figure 1.32: Experimental setup of 3PB test employed by Charpail [123].

The aforementioned studies mostly concentrated on quasi-static 3PB tests and used human ribs in the experiments. Recently, Aubert et al. [124] used porcine ribs as human rib surrogates and carried out dynamic 3PB tests of porcine ribs at high velocity impacts using Split Hopkinson Pressure Bar (SHPB) apparatus with the aim of investigating dynamic behaviors of ribs. Subsequently, Ayagara et al. [31,125] conducted experimental studies of porcine ribs subjected to dynamic 3PB loadings applying SHPB apparatus as well, where force response, structural response and fracture pattern were studied. Fig. 1.33 exhibits the experimental configuration of porcine rib under dynamic 3PB bending using SHPB apparatus.

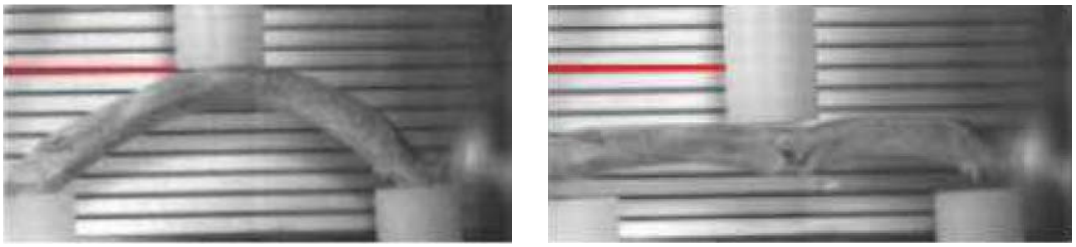

Figure 1.33: Illustration of porcine rib under dynamic 3PB bending using SHPB apparatus, extracted from [125].

1.3.2.2 Anterior-Posterior Bending

Anterior-posterior bending loading produces tension on the external surface of the rib, which is different from 3PB bending where the loading is in a lateral direction and produces compression on the external surface [126]. Anterior-posterior bending tests on isolated ribs were applied by researchers to replicate real-world frontal impact loading conditions in order to investigate the structural responses of ribs in recent years [27,29,108,127–133]. Charpail et al. [27] first proposed a novel experimental protocol to apply dynamic anterior-posterior loads to individual ribs using a pendulum fixture in 2005, where the sternal (anterior) end of the rib was pushed towards the vertebral

(posterior) end within rib's major plane. Kindig et al. [128] then conducted anterior-posterior bending experiments on 27 isolated rib extracted from levels 2 to 10 in order to identify rib level differences in fracture characteristics, rib 2 was found to be stiffer than other rib levels based on the methodology proposed by Charpail. The experimental configuration is shown in Fig. 1. 34. Also, Li et al. [29,127] then performed experiments of second, fourth and tenth human isolated ribs under anterior-posterior bending to study ribs' structural responses and fracture tolerance. Moreover, many experimental studies of human isolated ribs under dynamic frontal impacts were conducted in Ohio State University [108,130–133], for instance, variations in structural responses of human isolated ribs under dynamic anterior-posterior loading were investigated by Agnew et al. [108] and Kang et al. [133] based on a large quantity of ribs, where different affecting factors of age, sex, body size and rib geometry were taken into account. Fig. 1.35 (a)-(b) exhibits the experimental fixture of isolated ribs under dynamic frontal impacts by a pendulum and rib fractures, respectively.

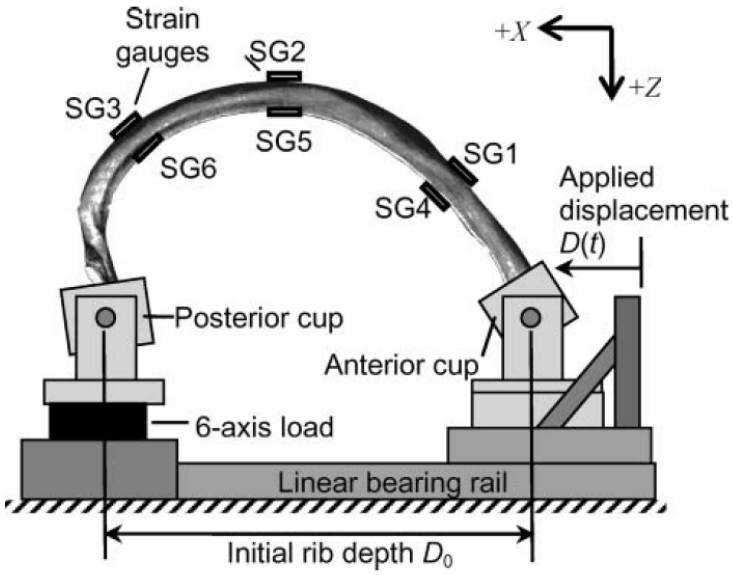

Figure 1.34: Experimental configuration of anterior-posterior bending on ribs, extracted from [128].

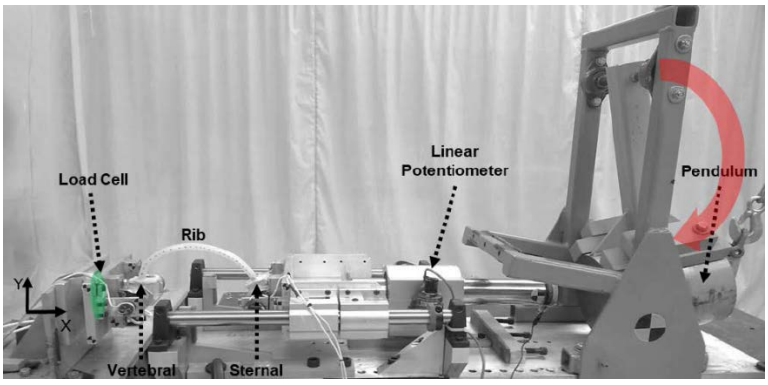

(a) Experimental fixture of ribs under dynamic frontal impacts by a pendulum.

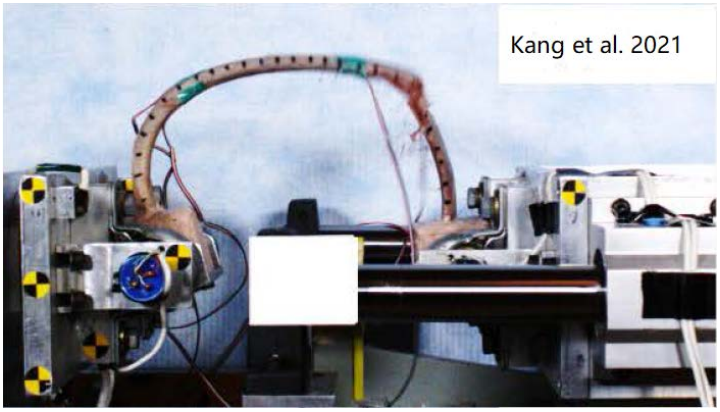

(b) A picture of rib fractures.

Figure 1.35: Experimental (a) fixture of isolated ribs under dynamic frontal impacts by a pendulum and (b) rib fractures [133].

1.4 Numerical Simulations of Impacts on Soft Tissues and Ribs in the Literature

1.4.1 Simulations on Common Soft Tissue Substitutes

The development of computer science allows researchers to apply numerical simulations such as Finite Element (FE) method to simulate and investigate the behaviors of human tissues, which can overcome the limitations in biomechanical experiments. FE models can not only predict global human behaviors but also definite parts of human hard and soft tissues by precise modeling. In the past decades, various biomechanical FE models have been developed and play an important role in investigating injuries in biomechanical impacts. In the previous section 1.3.1, a literature review of the experimental studies of impacts on common soft tissue substitute ballistic gelatin and SEBS gel is introduced. In this section, the numerical simulation studies of impacts on ballistic gelatin and SEBS gel in recent years are reviewed.

Many numerical simulations have been conducted to simulate the behaviors of ballistic gelatins as soft tissue simulants in the contexts of penetrating and blunt impacts in recent years [40,47,50,114,115,134,135]. For instance, Wen et al. [47] simulated the penetration of a steel sphere impacting a 10% ballistic gelatin block through finite element analysis, the numerical temporary cavity size and pressure time histories corresponded well with the experimental ones. Fig. 1.36 and Fig. 1.37 display the mesh discretization of the finite element models and comparison of experimental and numerical temporary cavity profiles, respectively. Subsequently, Wen et al. [114] also numerically studied the behind armor ballistic trauma using a bullet striking a shielded

ballistic gelatin block. Moreover, the smoothed particle hydrodynamics (SPH) method combined with finite element method was used by Taddei et al. [40] and by Al.Khalil et al. [50] to numerically interpret the penetrating impacts on 20% and 10% ballistic gelatin, respectively

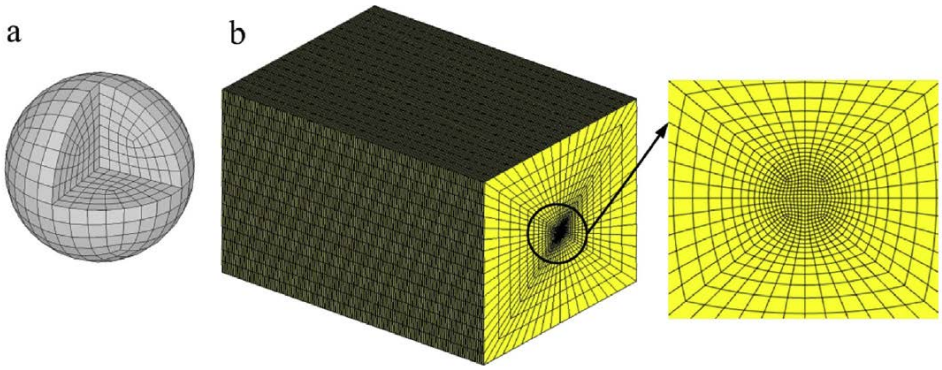

Figure 1.36: Finite element mesh discretization of the (a) steel sphere and (b) ballistic gelatin block [47].

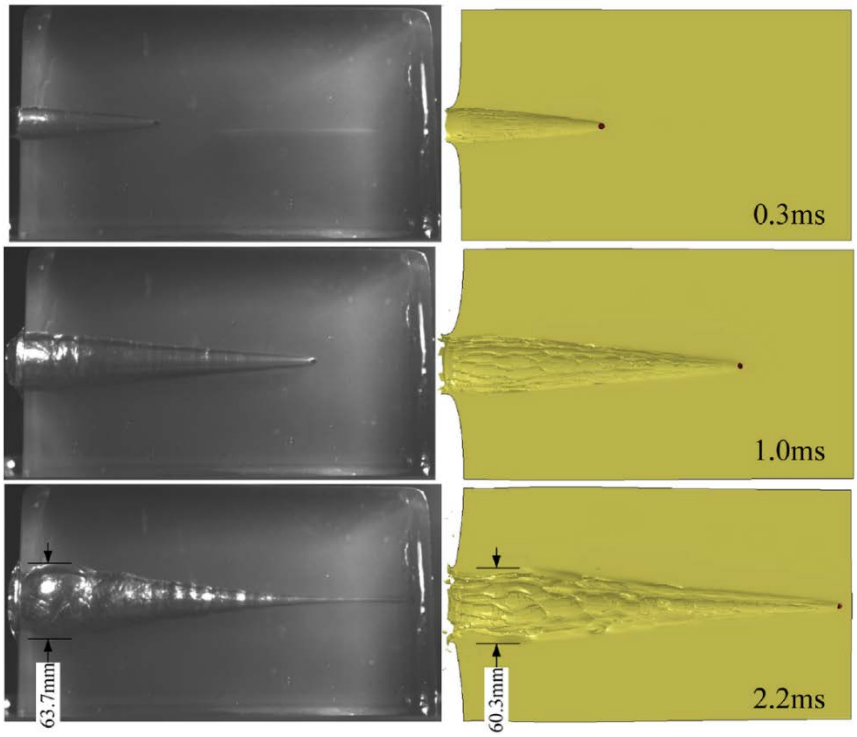

Figure 1.37: Comparison of experimental and numerical temporary cavity profiles in ballistic gelatin at an impact velocity of 728m/s [47].

Recently, numerical simulations of SEBS gels under high velocity impacts were also conducted by researchers to help better understand human soft tissue dynamic behaviors apart from experimental studies [59,60]. Bracq et al. [59] modeled the SEBS gel with a visco-hyperelastic constitutive law based on the Mooney-Rivlin model and validated it by replicating blunt ballistic experiments using finite element modeling.

The comparison of experimental and numerical displacement of blunt ballistic impacts on SEBS gel was shown in Fig. 1.38. In addition, Meng et al. [60] simulated the dynamic responses of the SEBS gel under high velocity micro-particle impacts at a microscale using the SPH method, which can be applied in the medical field.

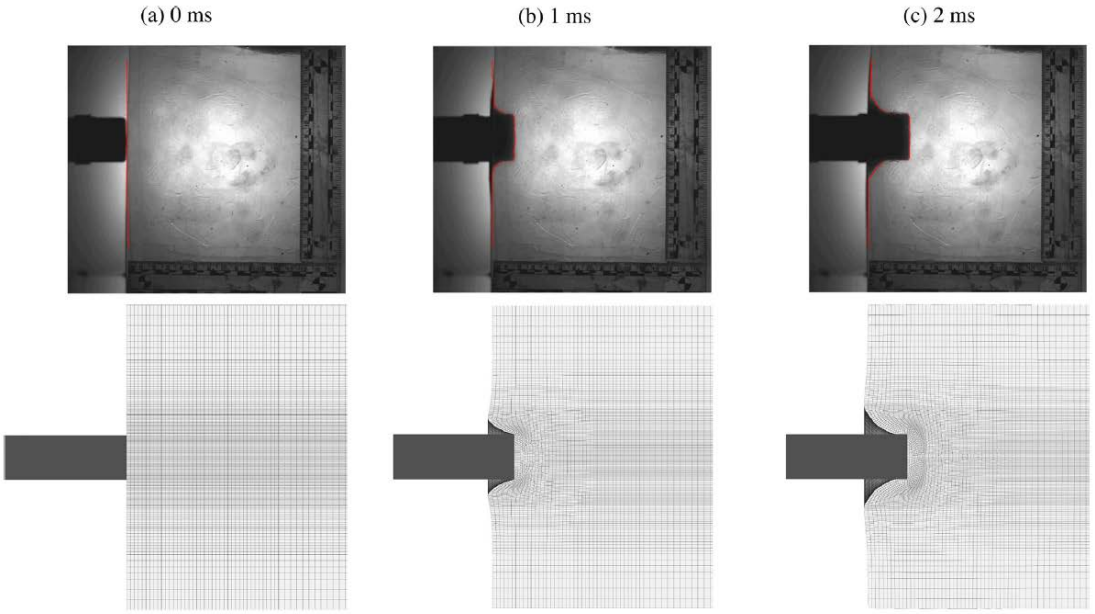

Figure 1.38: Comparison of experimental and numerical displacement of a blunt ballistic impact on SEBS gel [59].

1.4.2 Simulations on Isolated Ribs

As is introduced in section 1.3.2, numerous experimental studies of impacts on isolated ribs have been conducted in the past decades in order to better understand dynamic behaviors of ribs and predict the occurrence of rib fractures. Meanwhile, researchers also took advantage of numerical simulations as an alternative method, so this section review the numerical three-point bending (3PB) and anterior-posterior bending simulations on isolated ribs.

Charpail [123] simulated 14 human ribs without trabecular bone under 3PB bending as shown in Fig. 1.39, numerical results were used to optimize cortical bone properties in the following simulations. Ayagara et al. [31] conducted numerical studies of porcine ribs subjected to dynamic 3PB loadings applying SHPB apparatus, a modified elastic-plastic constitutive law was employed to model both cortical and trabecular bones, the numerical force-displacement curve and fracture pattern showed a good correlation with experimental results.

Figure 1.39: Representation of finite element modeling of rib cortical bone under 3PB bending by Charpail [123].

In addition, many researchers developed finite element models of isolated rib models under anterior-posterior bending loads [27–30,32,104,105,123,136]. Thereinto, Charpail et al. [27] established FE models of isolated human ribs with variable cortical thickness based on CT scan techniques and simulated them under anterior-posterior loadings. Numerical fracture locations and force values correlated well with experimental data even though the fracture time and displacement didn't match well with experimental data. Li et al. [28] developed and validated human rib FE models with two types of cortical meshes, in which hex-shell models were proved to be applicable for predicting rib structural responses and fractures and more computationally efficient than all-hex models. The authors subsequently investigated the effect of cortical thickness, mesh density and material properties on force-displacement relationship and rib fracture locations based on FE simulations [29]. Also, subject-specific FE rib models were created for predicting rib stiffness and fracture location under dynamic anterior-posterior bending by Iraeus et al. [30], seven out of the twelve rib models predicting good fracture locations compared to experimental tests. Recently, Yates et al. [32] established several subjected-specific 6th human rib FE models to predict rib biomechanical responses under anterior-posterior bending with material data derived from tensile coupon tests. Fig. 1.40 (a)-(d) displays several finite element rib models subjected to anterior-posterior bending loads in the literature.

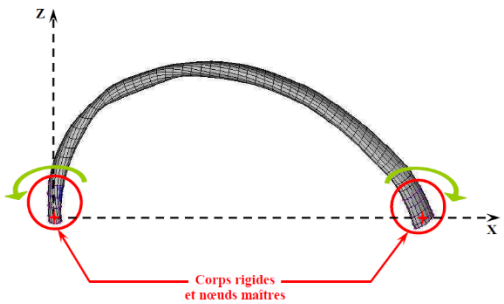

(a) Charpail [123].

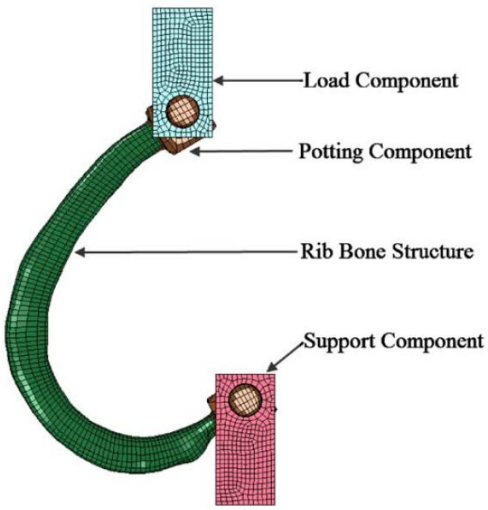

(b) Li et al. [28].

(continued)

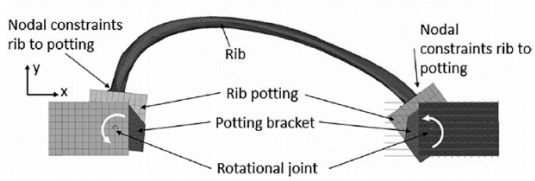

(c) Iraeus et al. [30].

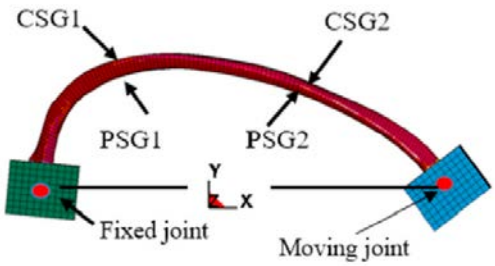

(d) Yates et al. [32].

Figure 1.40: Several finite element rib models under anterior-posterior bending loads.

1.5 Summary of Bibliographical Study

This chapter presents the literature review of the research background of this thesis. The biomechanics of human thorax is introduced where human thorax anatomy is presented first. Then, soft tissues and hard tissues (especially ribs) of human thorax are introduced respectively, including soft organs, common soft tissue and human rib substitutes, rib anatomy, material properties, soft tissue injuries and rib fractures. Finally, experimental and numerical studies of impacts on soft tissues and ribs in the literature are introduced, respectively.

The thorax part is found to be one of the most injured body areas under high velocity impacts, thereinto, rib fractures and soft tissue injuries like lung injuries are the most common thoracic injuries and can be life-threatening. Therefore, in order to better understand human thorax responses and injuries under high velocity impacts, it is of importance to investigate the dynamic responses of human tissues, which can provide valuable medical and forensic information and is also useful for designing and optimizing protecting devices.

In recent years, many biomechanical FE models have been established and employed to repeat real-world impact loading conditions to investigate human tissue behaviors which can avoid practical issues in biomechanical experiments. However, there is no model can take all the factors such as age, sex, material properties and geometry etc. into consideration. Therefore, this thesis aims to contribute to the investigation of dynamic responses of human tissues under high velocity impacts using finite element modeling.

Human tissues include soft tissues and hard tissues. In thoracic injuries, lung injuries are most common soft tissue injuries, and rib fractures are frequent hard tissue injuries. Among soft tissue substitutes, the synthetic polymer Styrene-Ethylene-Butylene-Styrene (SEBS) gel highlights a number of benefits against the typical ballistic gelatin such as environmental stability and transparency. In consequence, researchers adopted

the SEBS gel as soft tissue substitute in biomechanics impacts in recent years. But few studies pay attention to the development of constitutive law of the synthetic polymer SEBS gel. Hence, in Chapter 2, this thesis first aims to propose a novel strain-rate-dependent elasto-hydrodynamic constitutive law of the SEBS gel for the first time, which can interpret the dynamic behaviors of SEBS gel under various loading configurations. Dynamic three point bending (3PB) tests and anterior-posterior bending tests of isolated ribs are typically carried out to understand rib fractures, which mimic the environments like in car crash accidents. Only a few studies concentrate on dynamic 3PB tests of ribs under high velocity impacts using Split Hopkinson Pressure Bar (SHPB) apparatus, thus this thesis then numerically investigates the effect of geometrical and mechanical parameters of ribs submitted to high velocity impacts applying 3PB SHPB apparatus in Chapter 3. In addition, previous numerical studies on ribs' dynamic anterior-posterior bending defined human rib cortical bone material models using material data obtained from tensile coupon tests because of the absence of rib cortical bone compressive material properties in the literature. Actually, the rib suffers both tensile and compressive loading modes during MVCs, for instance, the cutaneous surface suffers tension while the pleural surface suffers compression in frontal crash conditions. Therefore, this thesis also develops rib FE models with various material properties including human rib cortical bone material properties from different loading modes (tension and compression), strain rates (0.5 strain/s and 0.005 strain/s) and ages as well as porcine rib material properties, in order to better understand rib structural responses and fracture locations under dynamic anterior-posterior bending in Chapter 4. Chapter 5 summarizes the overall conclusions of this thesis and points out the existing limitations, and finally discusses the openings of future work.

2 Numerical Modeling of the SEBS Gel under High Velocity Impacts: Investigation of the Effect of the Strain Rate in an Elasto-Hydrodynamic Law

2.1 Introduction

The synthetic polymer Styrene-Ethylene-Butylene-Styrene (SEBS) gel highlights a number of benefits against the typical ballistic gelatin such as environmental stability, reproducibility, mechanical consistency and transparency. Consequently, researchers adopted the SEBS gel as soft tissue substitute in biomechanics impacts in recent years. The development of appropriate constitutive material laws which can describe the main aspects of material responses and their implementation in FE codes is a key issue in FE simulations. Only Bracq et al. [59] payed attention to the development of constitutive modeling of the SEBS gel. In consequence, the main purpose of this chapter is to propose a novel strain-rate-dependent elasto-hydrodynamic constitutive law of the SEBS gel for the first time based on the mechanical characterization experiments of the literature, which can interpret the dynamic behaviors of SEBS gel under various loading configurations. The proposed law is then implemented as a user material subroutine programed in Fortran in an explicit nonlinear FE software Radioss (Altair Hyperworks) to reproduce various loading configurations in order to validate the accuracy of the model, and the effect of strain rate is investigated. Numerical analysis reveals that the strain-rate-dependence effect is significant in SEBS gel especially for high strain rates.

The outline of this chapter is organized as follows. In Section 2.2, the SEBS gel material used in this thesis is first introduced. Then, the constitutive modeling of the SEBS gel and finite element validation tests under various loading configurations including compressive plate test, Split Hopkinson Pressure Bar (SHPB) test and blunt ballistic impact test are presented as well. Section 2.3 displays the comparative results of implementation of the new proposed law in an explicit non-linear FE software against experimental data of the literature. Section 2.4 discusses the obtained comparative results presented in Section 2.3. Finally, the major conclusions are summarized in Section 2.5.

2.2 Materials and Methods

2.2.1 Material

The soft tissue substitute material applied in this thesis is the same synthetic polymer SEBS gel (styrene-ethylene-butylene-styrene) used by Bracq et al. [58]. It is a triblock copolymer produced by Kraton Polymers LLC (G1652). The 30 wt% SEBS gel is obtained by mixing SEBS powder and mineral oil with the styrene/elastomer ratio of 30/70%. The mineral oil is supplied by ESSO S.A.L (PRIMOL 352). The manufacturing process of this gel does not need complicated equipment and is comparatively straightforward. An oven is used to place a metallic drum where the mineral oil is preheated at 100° C for 2h. The SEBS powder is added in gradually and mixed continuously at the same time. Then increase the temperature to 150° C and keep the mixtures soaked for 4h with intermittent mixing. After the mixture liquid is fully melted and there exists no bubble, the liquid is cast into an appropriate mold with a dedicated geometry. The liquid is cooled to room temperature slowly before the removal from the mold in order to reduce the sink deformation. The material density of this SEBS gel is about 880kg/m^3.

2.2.2 Constitutive Modeling

It is essential to develop appropriate constitutive material laws for modeling soft tissue simulants which can describe the main aspects of material responses and their implementation in FE codes. To our knowledge, only Bracq et al. [59] payed attention to the constitutive modeling of the synthetic polymer SEBS gel, where the authors developed a novel visco-hyperelastic constitutive law based on the Mooney-Rivlin model. Nevertheless, Mauzac et al. [55] found that the SEBS gel exists a linear elastic mechanical characterization on its surface. Hydrodynamic behavior of the gelatins is considered to be more suitable at least at the beginning of penetration events [66]. Meanwhile, strain rate effects are proved to be significant and were included in the modeling of the synthetic polymer SEBS gel [58,59]. Therefore, the author here aims to propose a novel strain-rate-dependent elasto-hydrodynamic constitutive law of the SEBS gel based on the mechanical characterization experiments of the literature for the first time, which can simulate the SEBS gel behavior under blunt ballistic impacts.

The new proposed constitutive law here is implemented as a user material subroutine programmed in Fortran in the explicit non-linear FE software Radioss (Altair Hyperworks) in order to take the strain rate sensitivity into account. The stress tensor in this law can be decomposed into a deviatoric and a dilatational components and they represent the elastic and hydrodynamic behavior, respectively. The deviatoric stress is

calculated by Hooke's law using Young's modulus *E*. The hydrodynamic behavior is represented by a polynomial equation of state (EOS) [137]. Moreover, the strain rate dependence of the Young's modulus *E* is investigated via Matlab curve fitting toolbox based on the mechanical characterization experiments conducted by Bracq et al. [58]. The detailed formulation of the material law is described as follows.

The deviatoric stress representing the elastic behavior can be expressed as [66]:

$$\boldsymbol{s} = 2G\boldsymbol{e} \tag{2.1}$$

where G is shear modulus and $\boldsymbol{e}$ is the deviatoric strain defined as:

$$\boldsymbol{e} = \boldsymbol{\varepsilon} - \frac{1}{3}(tr\boldsymbol{\varepsilon})\boldsymbol{I} \tag{2.2}$$

where $\boldsymbol{\varepsilon}$ and $\boldsymbol{I}$ are elastic strain tensor and the unit tensor, respectively.

The dilatational component of the constitutive law is represented by a polynomial equation of state (EOS) describing the hydrodynamic behavior denoted as [137]:

$$p = C_0 + C_1\mu + C_2\mu^2 + C_3\mu^3 \tag{2.3}$$

where p is the pressure, C_0, C_1, C_2 and C_3 are material constants and μ is a dimensionless parameter written as:

$$\mu = \frac{\rho}{\rho_0} - 1 \tag{2.4}$$

where ρ and ρ_0 are current mass density and initial mass density, respectively.

For small and moderate values of μ, the material constants in Eq. (2.3) are given as [66]:

$$\begin{aligned} C_0 &= 0 \\ C_1 &= \rho_0 c_0^2 \\ C_2 &= (2k-1)C_1 \\ C_3 &= (k-1)(3k-1)C_1 \end{aligned} \tag{2.5}$$

where C_0 is the initial equilibrium pressure and assumed to be ignored, C_1 equals to the bulk modulus as c_0 is the bulk wave velocity and $k = 1.87$ is the Hugoniot constant parameter [138].

Thus, the elasto-hydrodynamic law here is expressed by combining the deviatoric and dilatational components as:

$$\boldsymbol{\sigma} = -p\boldsymbol{I} + \boldsymbol{s} \tag{2.6}$$

where $\boldsymbol{\sigma}$ is the stress tensor.

Moreover, taking the strain rate dependence into consideration, the Young's modulus E is denoted in terms of the strain rate $\dot{\varepsilon}$, the relationship between Young's modulus E and the strain rate $\dot{\varepsilon}$ is investigated via Matlab curve fitting toolbox based on the mechanical characterization experiments conducted by Bracq et al. [58]. Bracq et al. carried out experimental tensile tests by applying specific tensile samples and gripping devices to obtain the true stress-strain relationship of the SEBS gel at different strain rates from $0.072s^{-1}$ to $59.5s^{-1}$. Fig. 2.1 displays the true stress-strain curves of the SEBS gel at different strain rates extracted from [58]. It shows stress stiffening with the increase of strain rate. The Young's modulus of the SEBS gel at diverse strain rates are measured according to the slopes of the stress-strain curves. The value of Young's modulus E as a function of the strain rate based on a power law function is shown in Fig. 2.2, which is obtained by applying Matlab curve fitting toolbox. The general form of the equation is described as:

$$E = E_0 + a \cdot (\tfrac{\dot{\varepsilon}}{\dot{\varepsilon}_0})^n \tag{2.7}$$

where E_0 is the initial elastic modulus of the SEBS gel, $\dot{\varepsilon}_0 = 1/s$, and a and n are coefficients of the equation.
Thus, the new proposed strain-rate dependent constitutive law is depicted as follows:

$$E = 0.12 + 0.003093\dot{\varepsilon}^{0.8505}$$
$$R^2 = 0.9879 \tag{2.8}$$

where the R-square coefficient of determination shows a high goodness of fit.

The strain-rate-dependent elasto-hydrodynamic law developed here is then implemented and validated as a user material subroutine programmed in Fortran in the explicit non-linear FE software Radioss (Altair Hyperworks) through various numerical simulations.

For the material property, a same mathematical law was implemented except for the Young's modulus equation (Eq. 2.8), which is secondary considered as a constant value, leading to an elasto-hydrodynamic law without the influence of the strain rate.

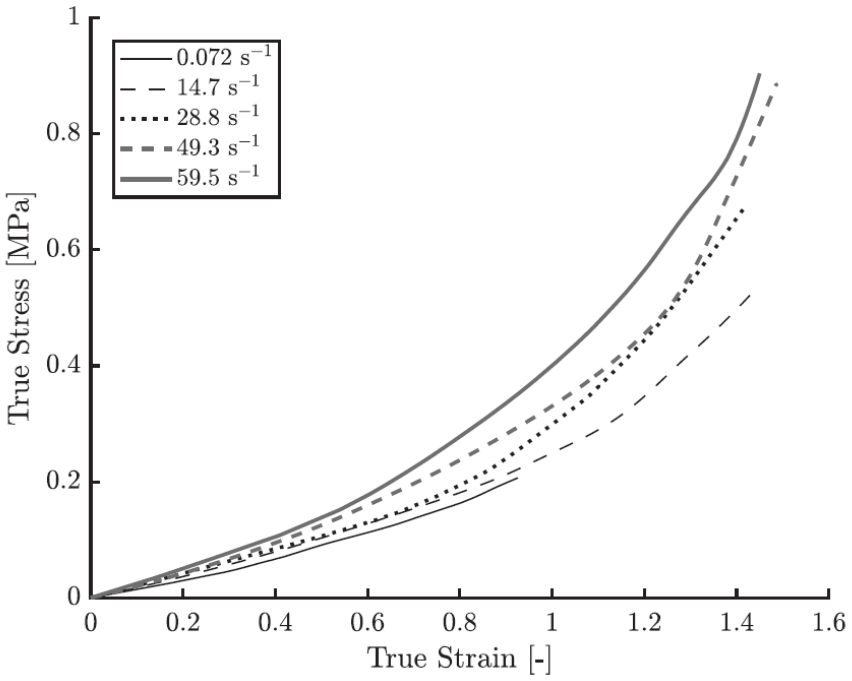

Figure 2.1: True stress-strain curves of the SEBS gel at different strain rates extracted from [58].

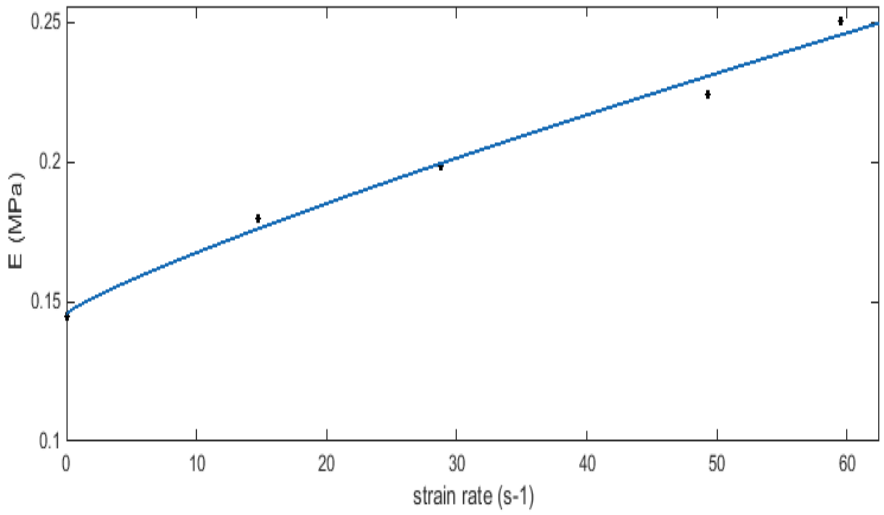

Figure 2.2: Strain rate dependence of Young's modulus E via curve fitting based on power law function.

2.2.3 Finite Element Modeling

2.2.3.1 Compressive Plate Test

Validation tests are conducted via implementation of the new proposed law in finite element simulations under various loading configurations. Firstly, the finite element modeling of compression experiments is established at intermediate strain rates from 14.7s^{-1} to 59.5s^{-1}. Fig. 2.3 displays the experimental configuration of the SEBS gel compressed by a steel plate. To model the equivalent loading conditions in experiments [58], the geometry size of the SEBS gel cylinder is 5.5mm in height and 10mm in diameter. The aspect ratio (L/D) inferior to 0.63 can avoid unstable results in such compressive numerical simulations [139]. A flexible thin steel plate is used to compress the gel sample and another fixed one to support it. Specific displacement rates of 80, 158, 271 and 327mm/s are applied to the flexible plate in order to represent diverse strain rates of 14.7, 28.8, 49.3 and 59.5s^{-1} in compression experiments, respectively. The use of silicon oil lubricant between plates and the gel leads to a comparatively low friction coefficient. The constant friction coefficient $F_{coulomb}$ between the contact interfaces of steel plates and the gel sample is equal to 0.06 and has been proved to be reasonable at intermediate strain rates [59]. Also, a minimal physical gap is selected between the interfaces for convenient numerical solutions. The finite element model of the SEBS gel under compressive plate tests is shown in Fig. 2.4. Comparisons between numerical data and those in experiments of the literature are investigated and discussed.

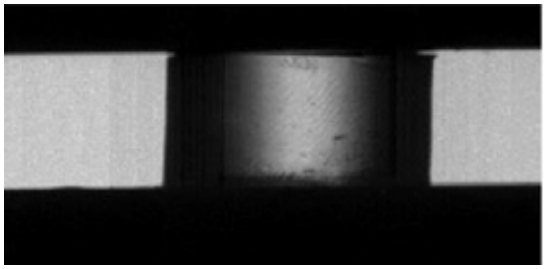

Figure 2.3: Experimental configuration of the SEBS gel compressed by a steel plate, extracted from [59].

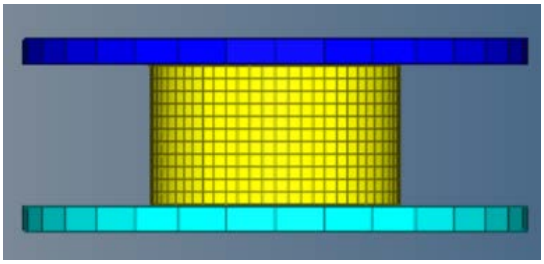

Figure 2.4: Finite element modeling of the SEBS gel under compressive plate tests.

2.2.3.2 Split-Hopkinson Pressure Bar Test

Then, an accurate finite element model of the Split Hopkinson Pressure Bar (SHPB) apparatus is developed in order to replicate the dynamic SHPB experiments in a numerical level. As shown in Fig. 2.5, it consists of a striker bar, an input bar and an output bar. The mesh discretization near the strain gauges and the SEBS gel sample is illustrated in Fig. 2.6. Specifically, the red elements in Fig. 2.5 are utilized to reflect the input and output strain signals along the longitudinal bar direction. The geometry sizes and mechanical parameters of the polymeric bars are displayed in Table 2.1. Furthermore, the FE SHPB model established here can be reduced to a quarter during calculations because of the symmetry in order to save calculation time. The initial impact velocities of the striker bar used here are determined in dynamic experiments [58] with an object of achieving dynamic strain rates from $630s^{-1}$ to $1260s^{-1}$. Besides, a Coulomb friction law is applied between the contact interfaces of bars and the gel sample, which may explain the barreling effect during compression experiments. The friction coefficient values for each strain rate are extracted from the literature [59].

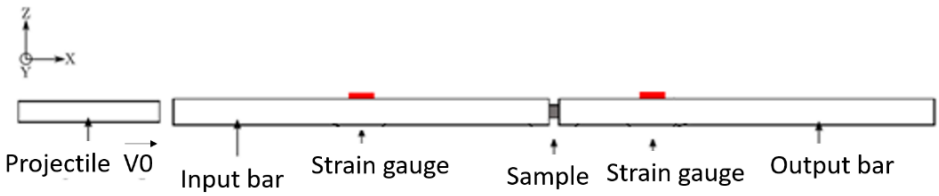

Figure 2.5: Schematic of configuration of the SHPB experiments, adapted from [59].

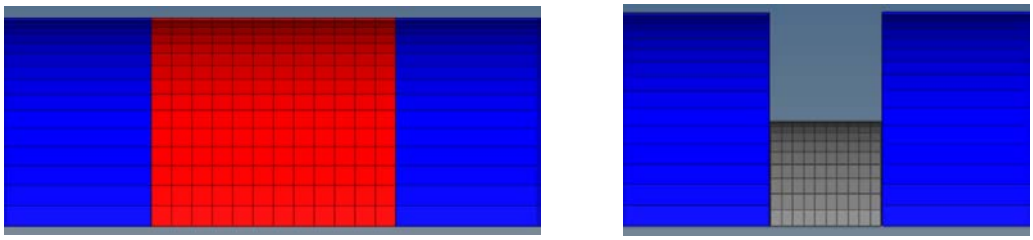

Figure 2.6: Mesh discretization (a quarter) near the strain gauge (left) and the SEBS gel sample (right).

Table 2.1: Geometrical sizes and mechanical parameters of the SHPB polymeric bars [59].

	Striker bar	Input bar	Output bar
Length (mm)	950	3040	3020
Diameter (mm)	16.1	20.3	20.4
Density (kg/m^3)	1149	1158	1146
Wave speed (m/s)	1750	1740	1740
Young's modulus (MPa)	3517	3506	3470
Poisson's ratio	0.4	0.4	0.4

2.2.3.3 Blunt Ballistic Impact Test

Finally, a typical blunt ballistic experiment is replicated through finite element modeling. Fig. 2.7 illustrates the gel wall displacement impacted by a rigid projectile. As is mentioned in previous SHPB modeling, the establishment of the FE model can be degraded to a quarter due to the symmetrical boundary conditions. The representative FE model of a rigid projectile impacting the SEBS gel is shown in Fig. 2.8. The rigid round projectile is of 37mm in diameter and with a mass of 140g as was used in experiments [11,59]. More precisely, the geometry size, mesh discretization as well as corresponding boundary conditions are presented in Fig. 2.9. The dimension of the SEBS gel cube is 250mm. Considering the high element distortions in ballistic impact simulations, the gel mesh is discretized more precisely. As illustrated in Fig. 2.9, a relatively fine mesh is chosen in the impact region and a coarser mesh is sufficient for the region away from the impact center. The symmetrical boundary conditions are applied to symmetry planes of the gel cube and the backing plate in experiments is modeled by fixing the backing surface of the gel. Nevertheless, different from the previous two FE configurations, the Coulomb friction law in impact modeling is ignored as it has been revealed to have no influence on gel wall displacements [59]. Three different initial impact velocities of 12, 20 and 30m/s are applied to the projectile respectively for repeating the experimental configurations.

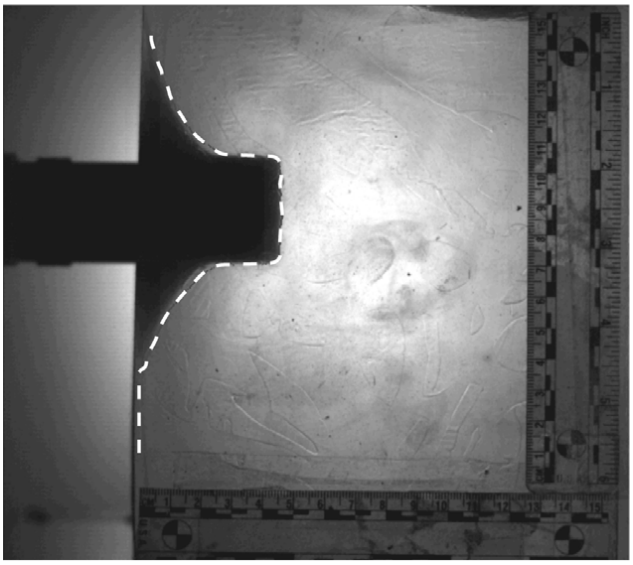

Figure 2.7: A picture of the gel wall displacement during blunt ballistic impacts by a rigid projectile [59].

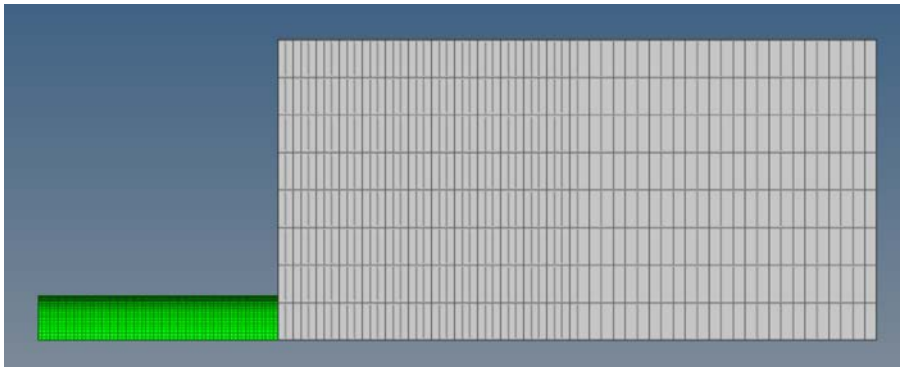

Figure 2.8: Schematic of the FE modeling of a rigid projectile impacting the SEBS gel (a quarter).

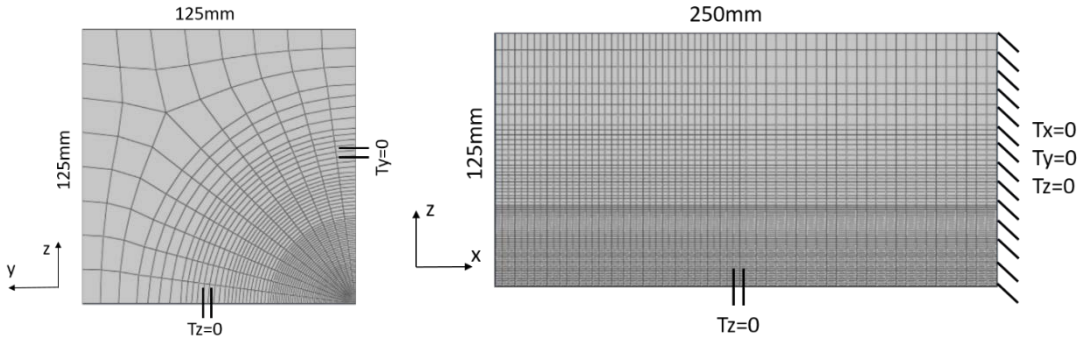

Figure 2.9: Depictions the SEBS gel size, mesh and boundary conditions in blunt ballistic FE modeling (a quarter).

2.3 Results

2.3.1 Validation of Compressive Plate Test

In order to highlight the effect of the strain rate on the results, each configuration is numerically replicated with two laws (with and without the strain rate dependency), i.e. with a constant Young's modulus from one side and with the developed Young's modulus as a function of the strain rate as described in Section 2.2.2 from the other side. Firstly, Fig. 2.10 (a)-(b) provides a comparison of experimental and numerical load versus displacement curves with and without strain rate dependence at diverse intermediate strain rates.

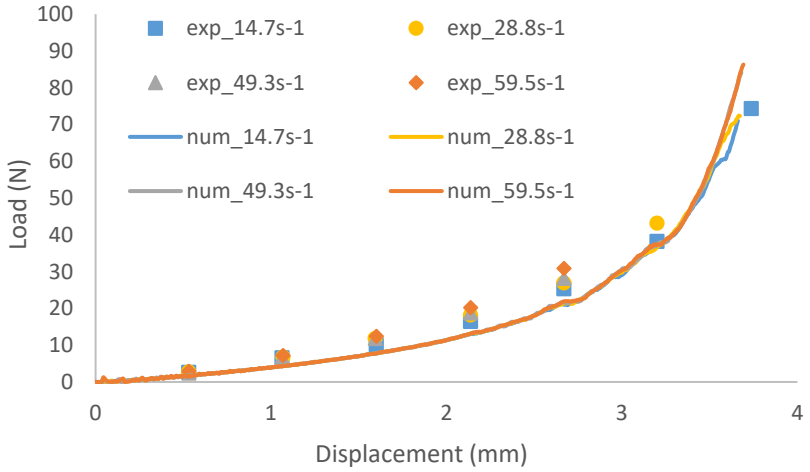

(a) with strain rate dependence

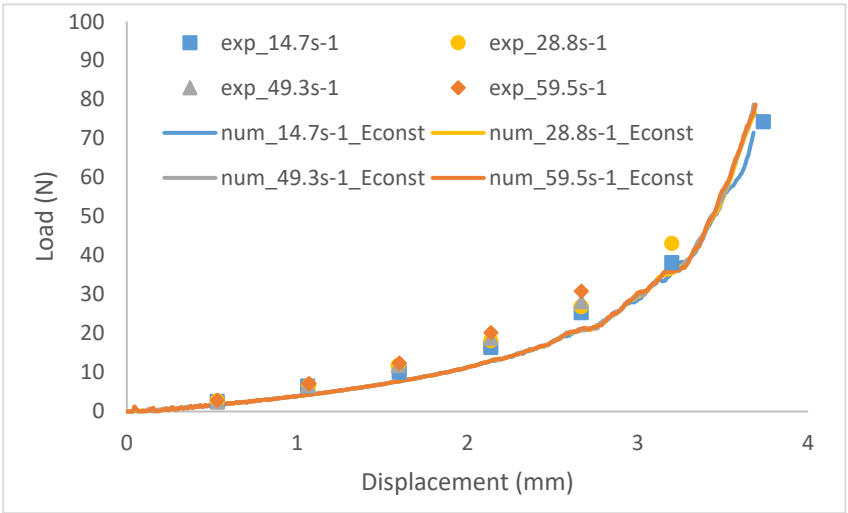

(b) without strain rate dependence (constant Young's modulus)

Figure 2.10: Experimental and numerical load versus displacement curves with (a) and without (b) strain rate dependence during compression tests at intermediate strain rates.

2.3.2 Validation of Split-Hopkinson Pressure Bar Test

The second configuration consists of the numerical replication of dynamic SHPB compressive experiments on SEBS gel at different strain rates. Fig. 2.11 (a)-(f) illustrates the engineering strain time histories at various strain rates (from 630 s^{-1} to 1260 s^{-1}) with and without strain rate dependence.

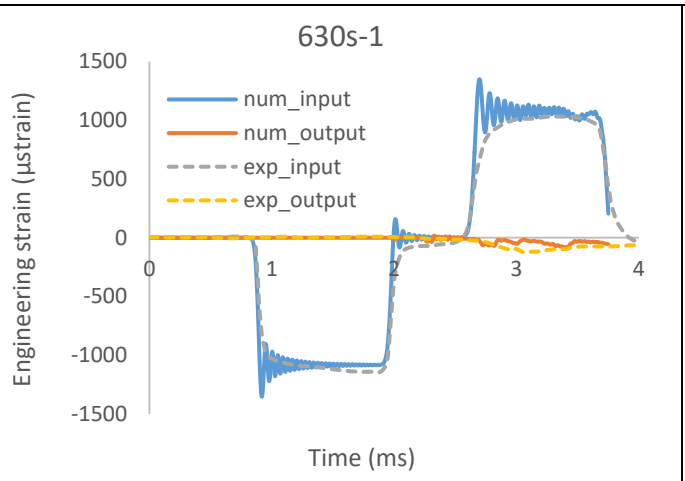

(a) 630s^{-1} with strain rate dependence.

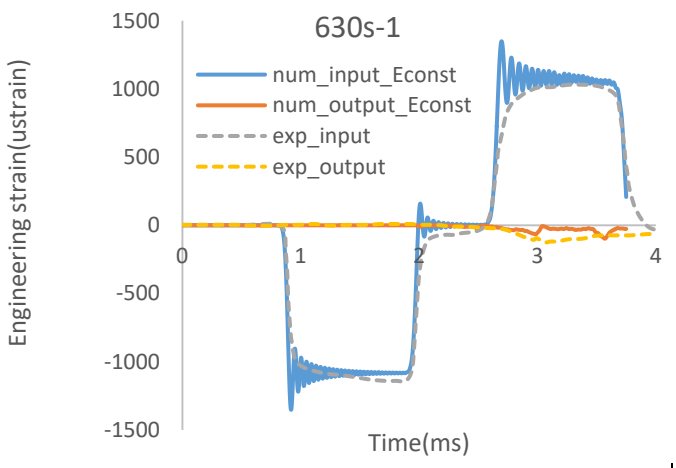

(b) 630s^{-1} without strain rate dependence (constant Young's modulus).

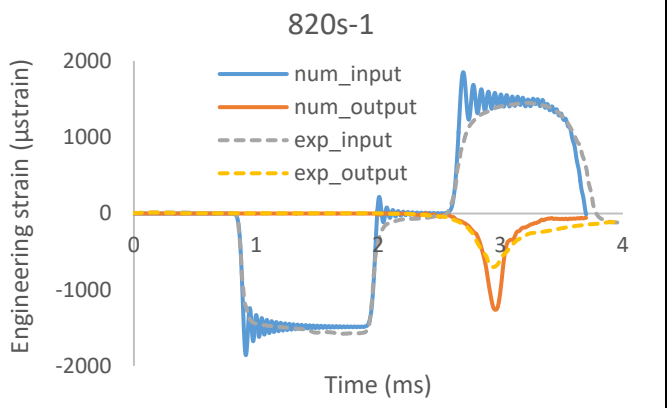

(c) 820s^{-1} with strain rate dependence.

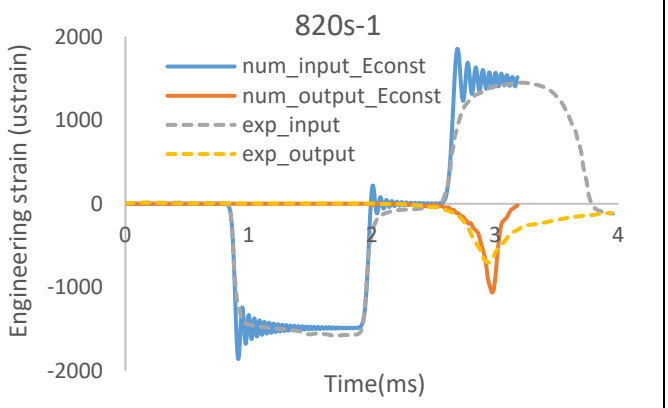

(d) 820s^{-1} without strain rate dependence (constant Young's modulus).

(continued)

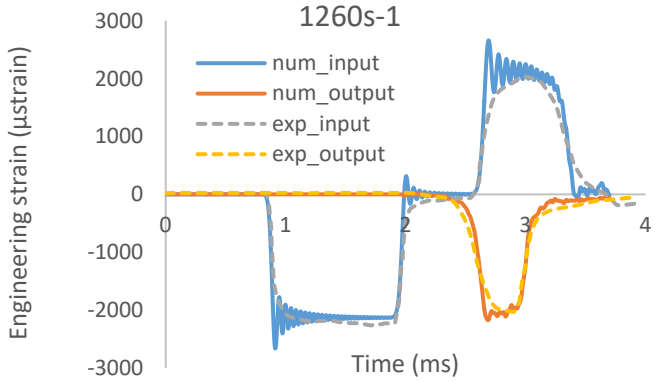

(e) $1260s^{-1}$ with strain rate dependence.

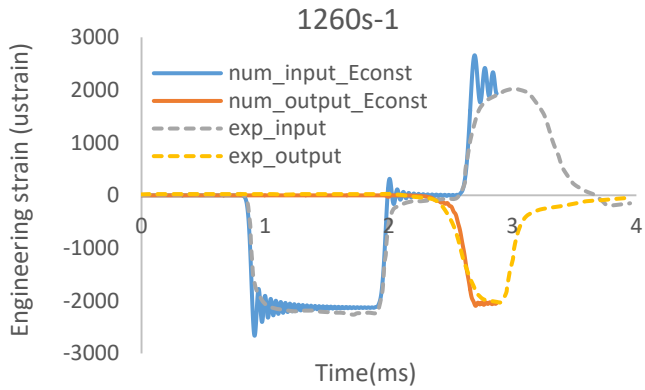

(f) $1260s^{-1}$ without strain rate dependence (constant Young's modulus).

Figure 2.11: Engineering strain time history provided by the SHPB simulations at various strain rates, and for the two constitutive laws.

2.3.3 Validation of Blunt Ballistic Impact Test

Finally, the third numerical replication consists of the impact of the cylindrical projectile on the SEBS gel target at three different velocities. Fig. 2.12 presents the comparison of the numerical gel wall displacement time histories with the two laws between experimental data of the literature. Moreover, the gel wall stress distributions (with (a) and without (b) strain rate dependence) under three different impact velocities are shown in Fig. 2.13.

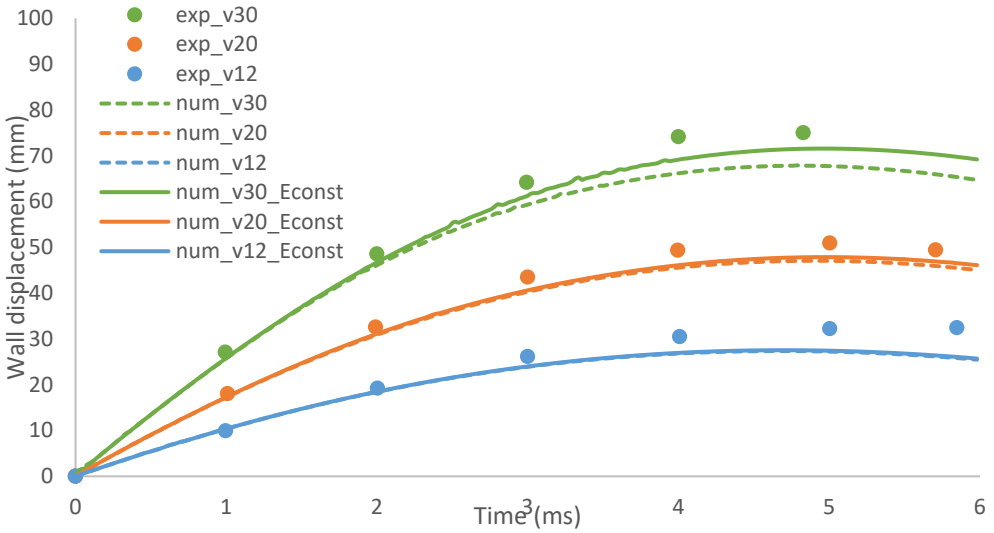

Figure 2.12: Experimental and numerical gel wall displacement time history at various initial impact velocities (12, 20 and 30m/s).

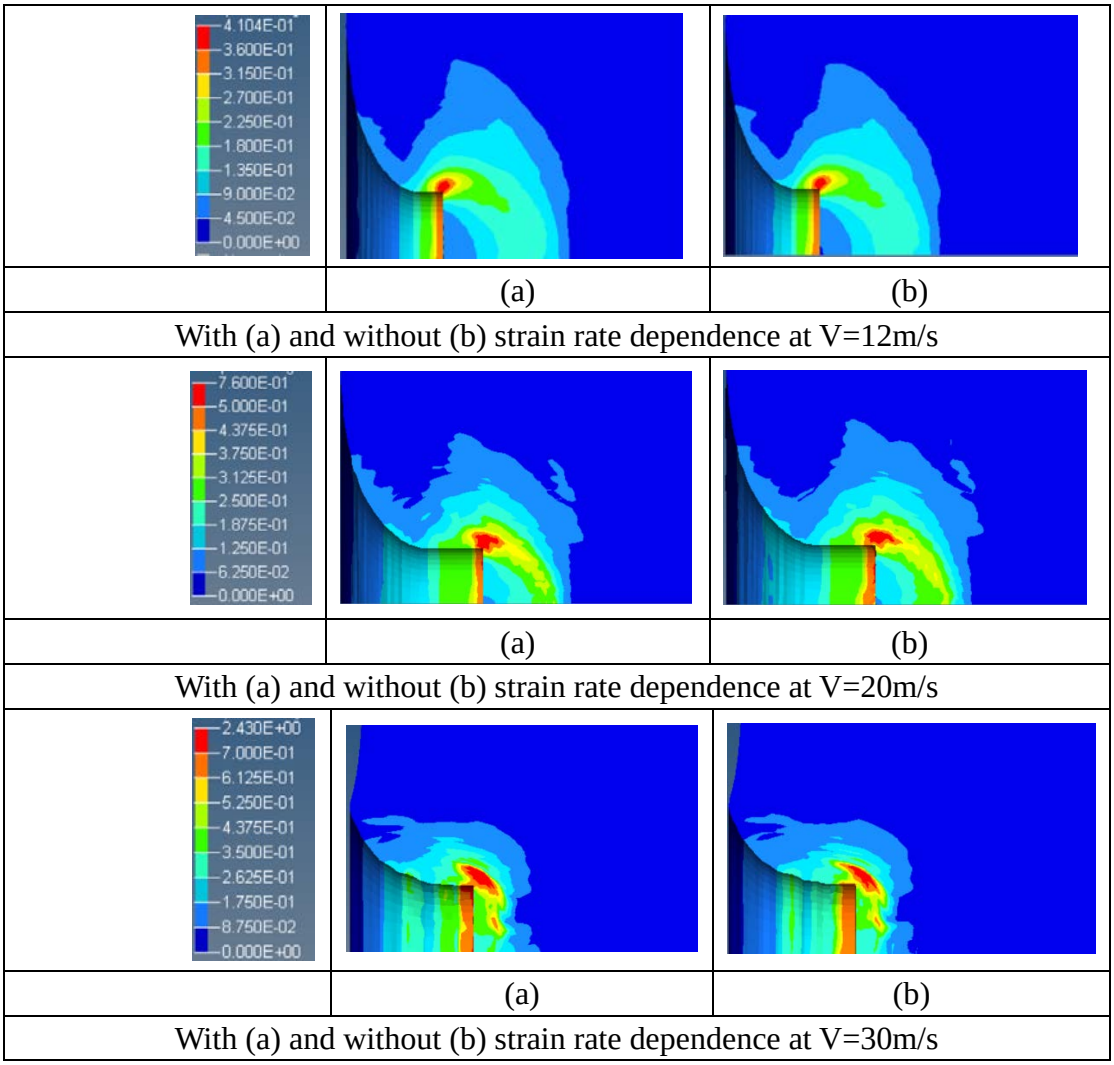

Figure 2.13: Stress distribution (MPa) in the SEBS target under various impact velocities with two different laws.

In addition, Fig. 2.14 (a)-(c) compares the average error of experimental and numerical results between this study (elasto-hydrodynamic with strain rate effect) and Ref. [59]. Compression test at $14.7s^{-1}$, blunt impact at 30m/s and SHPB analysis at $1260s^{-1}$ are depicted, respectively.

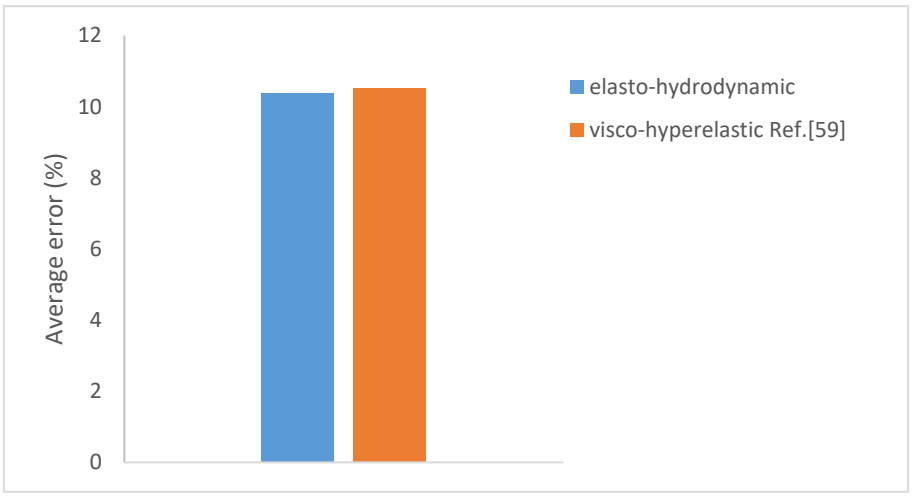

(a) Compression test at $14.7s^{-1}$

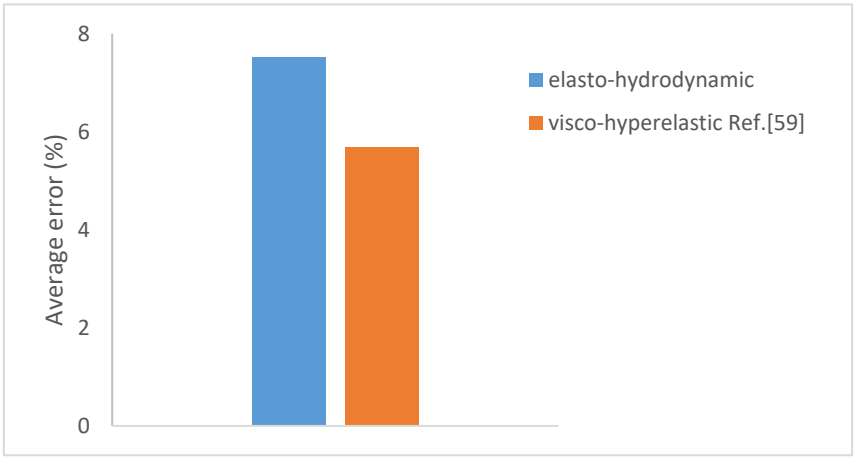

(b) Blunt impact at 30m/s

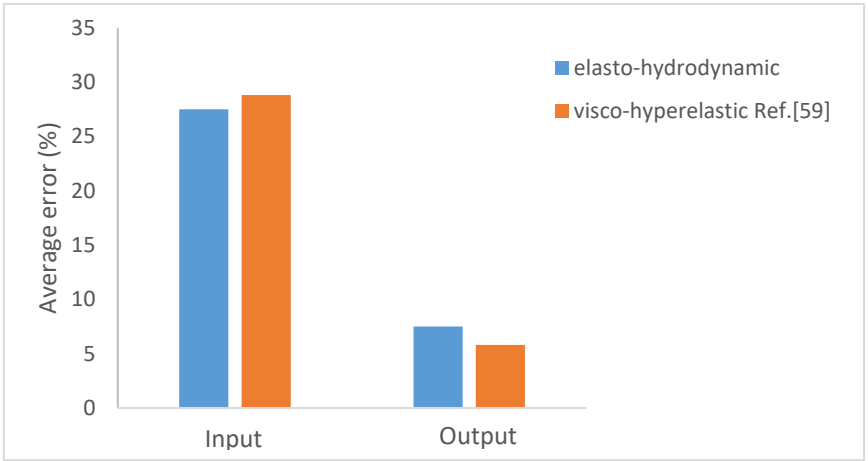

(c) SHPB analysis at $1260s^{-1}$

Figure 2.14: Comparison of average error of experimental and numerical results between this chapter (elasto-hydrodynamic with strain rate effect) and Ref. [59].

2.4 Discussion

The numerical results presented in Section 2.3 consist of the implementation of the elasto-hydrodynamic law with and without the strain rate effect, under various loading configurations. Comparative studies were investigated between numerical and experimental results in order to validate the feasibility of the proposed constitutive law and to study the strain rate influence.

Firstly, Fig. 2.10 (a)-(b) depicts the numerical and experimental loads as a function of displacement during compression tests at intermediate strain rates. It shows the same rising tendency of numerical loads applying the proposed constitutive law as experimental data although numerical values are slightly inferior to those in experiments. It is also deserved to notice that the influence of the strain rate is moderate since all the curves with Young's modulus depending on strain rate (Fig. 2.10 (a)) or constant Young's modulus (Fig. 2.10 (b)) are superimposed.

Next, as is mentioned previously, the input and output strain gauges are used to record strain signals along the longitudinal bar direction in SHPB analysis. Fig. 2.11 (a)-(f) displays the comparison of numerical and experimental strain versus time from input and output strain gauges at various dynamic strain rates, where results without strain rate dependence are presented as well. It can be observed that the numerical input strain signals correlate well with the experimental ones at each strain rate. Also, numerical and experimental output strain signals have a good match although the numerical amplitudes are relatively smaller at $820s^{-1}$ which may be explained by the large element distortions and high stress in the gel sample when its deformation exceeds the bar diameter. On the other hand, it is worth noting that simulations without strain rate dependence are not able to run until end as illustrated in Fig. 2.11 (d) and (f). This point raises the question about the softness of the gel which should be higher at high strain rates, which indicates the necessity of taking the strain rate dependence into consideration when applying the SEBS gel as a human soft tissue simulant. The comparative studies here validate the ability of the new proposed strain-rate-dependent elasto-hydrodynamic law to interpret SEBS gel responses at dynamic strain rates, the numerical model is considered as validated against experimental data of the literature for different strain rates.

Moreover, the gel wall displacement as a function of time is commonly used as a primary measurement in blunt ballistic impacts. Experimental and numerical gel wall displacements versus time at various initial impact velocities of 12, 20 and 30m/s are displayed in Fig. 2.12. Also, Fig. 2.13 illustrates the numerical gel wall stress contour of the blunt ballistic impacts for the three velocities. It can be observed that the gel wall displacements with the proposed strain-rate-dependent elasto-hydrodynamic law have a good correlation with the experimental data. Simulations with a general elasto-

hydrodynamic law without strain rate dependence also show good correlations with experimental data. Slight discrepancies occur for the highest velocity at 30m/s.

In addition, the comparison of average error of experimental and numerical results between this study (elasto-hydrodynamic with strain rate effect) and Ref. [59] is conducted and shown in Fig. 2.14 (a)-(c). Compression test at $14.7s^{-1}$, blunt impact at 30m/s and SHPB analysis at $1260s^{-1}$ are depicted, respectively. It can be seen that the two models show similar average error compared to experimental results. Specifically, the relatively high error in Fig. 2.14 (c) for input strain can be explained by the fluctuant part of input signals in Fig. 2.11 (e).

Soft materials such as gelatin, SEBS gel or clay have been used in the literature as promising human soft tissue substitutes, and the mechanical characterizations of these kind of materials have been widely conducted, allowing extracting main material properties [38,43,45,53,56,58]. Based on these studies, researchers used these data to propose constitutive laws to be implemented in numerical codes. Focusing on mechanical behaviors for high velocity impacts, a number of constitutive laws such as hyperelastic law, viscoelastic law, visco-hyperelastic law and hydrodynamic law have been proposed. The hydrodynamic law has been used for the modeling of 10% and 20% gelatin [40,50]. For SEBS gel, Bracq et al. [59] proposed a strain-rate dependent visco-hyperelastic law based on the Mooney-Rivlin model. In the military contexts, blunt impacts or blast waves can strike the human body and induce soft tissue trauma at very high velocities, so it is of interest to investigate the same kind of material law that already validated in [40,50]. Therefore, combining the elasto-hydrodynamic aspect with strain rate dependency, the present study demonstrates the feasibility of the constitutive law.

More investigations on the influence of the strain rate are planned, in increasing its weight in the mathematical law, for example, its influence in the non-linear part of the deviatoric stress tensor, or adding its influence in the plasticity domain. The present mathematical law elaborated from stress-strain curves in Fig. 2.1 can also be improved, in considering stress-strain curves at higher strain rates. Finally, in addition to the loading configurations (compressive plate test, SHPB test and blunt impacts) conducted in this study on the SEBS gel, further investigations are planned to increase the validity of the proposed strain-rate dependent elasto-hydrodynamic law through studying the interactions of blast waves on the SEBS gel, where there exists higher strain rates.

2.5 Conclusion

In this chapter, a novel strain-rate-dependent elasto-hydrodynamic constitutive law of the synthetic SEBS gel was proposed for the first time based on the mechanical characterization experiments of the literature. The strain rate sensitivity of Young's

modulus E was investigated via Matlab curve fitting toolbox. The implementation of the new proposed law as a user material subroutine programmed in Fortran in the explicit non-linear FE software Radioss (Altair Hyperworks) under various loading configurations was studied, and comparisons with the elasto-hydrodynamic constitutive law with constant Young's modulus were investigated. Comparative studies were also conducted between numerical and experimental results in order to validate the feasibility of the proposed constitutive law. A good agreement exists between the numerical results of the proposed law and experimental data in the literature. Numerical analysis reveals that the strain-rate-dependence effect is significant in SEBS gel especially for high strain rates, which indicates the necessity of taking the strain rate dependence into consideration when modeling the SEBS gel as a human soft tissue substitute.

3 Numerical Investigation of Effect of Geometrical and Mechanical Parameters of Ribs Submitted to High Velocity Impacts

3.1 Introduction

Rib fractures are common in thoracic injuries that can lead to life threatening injuries. In consequence, it is of importance to investigate the dynamic responses of ribs under dynamic loadings, which can help understand the mechanisms of rib fractures and corresponding injury criterion. The well-known Split Hopkinson Pressure Bar (SHPB) apparatus can be employed to reproduce dynamic impact environments and has been applied in predicting the mechanical behavior of human surrogate materials. Dynamic three point bending (3PB) tests of isolated ribs can be carried out to understand rib fractures, which mimic the environments like in car crash accidents. In the review of existing scientific literature, there were few studies concentrating on dynamic 3PB of isolated ribs utilizing SHPB apparatus [31,124], thus this chapter aims to investigate the dynamic behaviors of isolated porcine ribs submitted to high velocity impacts using 3PB SHPB apparatus based on finite element simulations. The porcine ribs are approximated to curved beams and are assumed to have constant elliptical cross sections according to the average geometrical properties, and both porcine and human rib material properties are applied for comparison. Sensitivity studies were conducted to investigate the effects of geometrical and mechanical parameters such as cortical thickness, curvature radius and strain rate on dynamic behaviors of ribs by comparison with experimental data. The numerical curved beam rib models are validated and show biofidelic behaviors. Numerical analysis reveals that geometrical parameters of ribs play an important role in influencing ribs dynamic behaviors. The consideration of the effect of mechanical parameters like loading mode and strain rate sensitivity in FE rib models is also needed.

The outline of this chapter is organized as follows. In Section 3.2, experimental configurations and the finite element modeling of 3PB SHPB apparatus as well as the porcine rib model are firstly introduced. The model is used via an explicit non-linear FE software Radioss (Altair Hyperworks). Then, FE validation tests and sensitivity studies are presented. Next, Section 3.3 displays the comparative results of FE

simulations against experimental data of the literature with porcine rib and human rib material properties respectively. In Section 3.4, we discuss the obtained results and analyze the effects of geometrical and mechanical parameters on dynamic behaviors of ribs. Finally, Section 3.5 summarizes the major conclusions.

3.2 Materials and Methods

3.2.1 Configurations of Tests

The experimental tests of porcine ribs subjected to dynamic 3PB loadings applying SHPB apparatus were conducted by Ayagara et al. [31,125]. As shown in Fig. 3.1, the 3PB SHPB apparatus consists of a striker bar, an input bar and two output bars. The geometrical sizes of the bars are listed in Table 3.1. Specifically, the grey strain gauges in Fig. 3.1 are applied to measure the input and two output strain signals along the longitudinal bar direction. They are located at the middle of the input bar and at 400mm from the output bar-rib interface, respectively. A "time and space" shifting process is applied to address the strain signals, where the absolute time $t^{'}$=0 is defined when the striker bar impacts the input bar and an origin time $t_0^{'}$ is equal to time of arrival for the incident wave at the input bar-rib interface. So all the strains are given in terms of a relative time $t= t^{'}- t_0^{'}$.

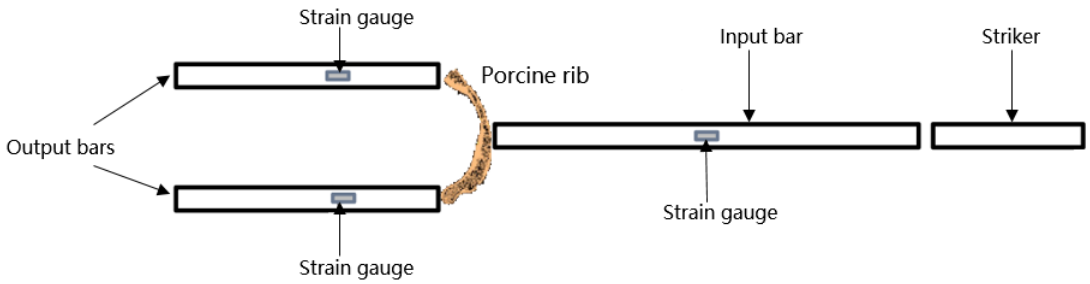

Figure 3.1: Schematic of configuration of the 3PB SHPB apparatus, adapted from [31].

Table 3.1: Geometrical sizes of the 3PB SHPB polymeric bars [125].

	Striker bar	Input bar	Output bar
Length (mm)	500	3000	1750
Diameter (mm)	15	20	20

3.2.2 Finite Element Modeling

3.2.2.1 Rib Model Geometry

The porcine ribs used in the experiments were purchased from the local supermarket. They were then numbered and the geometrical statistics of the porcine ribs were conducted in [125]. Also, as illustrated in Fig. 3.2 that the two extremities of the porcine rib are sanded to planar surfaces, in order to establish a stable contact between bar-sample interfaces. In general, the ribs can be approximated to curved beams and be assumed to have constant elliptical cross sections as displayed in Fig. 3.3. The average geometrical properties of the porcine ribs are listed in Table 3.2. Hence, in the present study, simulations were conducted on rib structures according to the average geometrical dimensions displayed in Table 3.2. A curved beam model with a constant elliptical cross section is used and the cortical bone thickness is assumed to have a constant value as well.

Figure 3.2: Representation of the initial position of the rib sample, extracted from [125].

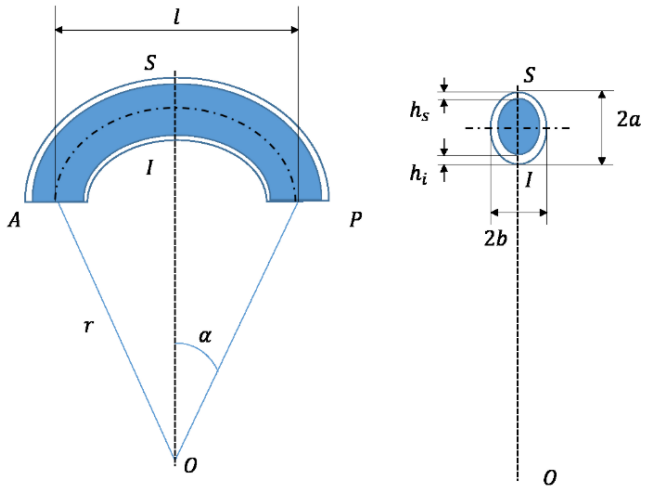

Figure 3.3: Schematic of a curved beam approximation of a rib, extracted from [125].

Table 3.2: Mean and standard deviation values of porcine ribs' geometrical properties, extracted from [125].

Property	Mean *u*	Standard deviation s.d.
Mass *m*	15.6316g	2.6918
Length *l*	113.594mm	10.5015
Radius *r*	63.3105mm	17.0245
Angle α	55.7716deg	14.66
Major axis 2*a*	10.0789mm	3.941
Minor axis 2*b*	9.7842mm	3.6823
Superior layer thickness h_s	1.0789mm	0.44669
Inferior layer thickness h_i	1.9632mm	0.80499

3.2.2.2 Mesh and Boundary Conditions

The present study of dynamic behaviors of isolated porcine ribs submitted to high velocity impacts using 3PB SHPB apparatus is based on finite element simulations via a FE software Altair Hyperworks. Fig. 3.4 presents the developed finite element model of dynamic three points bending tests on ribs applying the 3PB SHPB apparatus. The SHPB bars as well as the strain gauges are meshed with solid hexahedral elements, and one integral point is chosen for the sake of calculation time. As shown in Fig. 3.4, the mesh discretization near the input strain gauge and the rib sample is amplified. It can be seen that the mesh size of the input strain gauge is refined (as well as the output strain gauges) so that the strain signals along the longitudinal bar direction can be measured precisely. Several studies carried out previously proposed both all-hex and hex-shell models for ribs [28,29,105], while it reveals that for the FE model of ribs, the hex-shell model is more computationally efficient and therefore preferred. Consequently, in this study, the trabecular bone is modeled with hexahedral solid elements and the cortical bone with quadrilateral shell elements. The element size of the rib model is around 0.7mm in order to ensure an adequate prediction of the rib behavior.

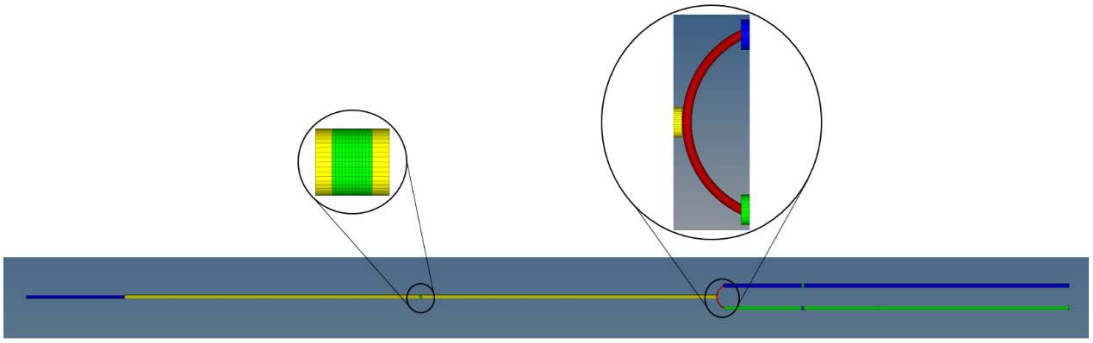

Figure 3.4: Representation of the FE model of 3PB SHPB apparatus.

Consistent boundary conditions are set up in the FE model for modeling equivalent loading conditions as in the experiments. The nodes of the rib sample are left free as it is initially positioned between input and output bars with no constraint. The interface Type 7 is employed between the bar-sample interfaces as well as the striker-input bar interface, which is a general purpose impact interface and able to simulate all types of impact between a master surface and a group of slave nodes [140]. Also, tied contact interface Type 10 is defined between the trabecular-cortical bone interface. A constant friction coefficient between the bars and the rib sample interfaces is set to 0.1 according to the literature [31]. Besides, a minimal physical gap is chosen between the contact interfaces for convenient numerical solutions.

3.2.2.3 Material Properties

Considering the relatively lower mechanical impedance of the rib compared to classical metallic bars, the polymeric bars made of nylon are employed in order to avoid a perturbed signal processing. The elastic constitutive law is applied for the polymeric SHPB bars, and the mechanical parameters are listed as follows: mass density $\rho = 1200 kg/m^3$, Young's modulus $E = 3300 MPa$ and Poisson's ratio $\nu = 0.4$.

It is feasible to apply an elasto-plastic material law for both cortical and trabecular bones as described in previous studies [28–31,105]. Also, it is assumed that the cortical bone shows isotropic hardening while the trabecular bone obeys kinematic hardening [31,141]. Thus, an elasto-plastic material model Law 2 (Johnson-Cook material) in RADIOSS with isotropic hardening is applied in the present study for cortical bone, and the trabecular bone is assigned with Law 3 (Johnson-Cook material, but only compatible with solid elements) with kinematic hardening. No strain rate hardening effect is implemented. A built-in failure criterion based on the maximum fracture plastic strain is used, rib fracture occurs if the plastic strain exceeds the maximum fracture plastic strain. The material parameters of porcine rib cortical and trabecular bones used here are presented in Table 3.3.

Table 3.3: The material parameters of porcine rib cortical and trabecular bones, extracted from [31].

Parameter	Cortical	Trabecular
Density (kg/m^3)	1690.9	772.9
Young's modulus (MPa)	9374	1800
Tangent modulus (MPa)	937	45
Yield stress (MPa)	70.876	20.48
Poisson's ratio	0.3	0.45
Fracture plastic strain	0.02	0.03

In addition, human rib material properties are also applied to study the effect of mechanical parameters on dynamic behaviors of isolated ribs. Thus, human rib cortical bone material properties from different loading modes (tension and compression) and strain rates (0.005 strain/s and 0.5 strain/s) are used as shown in Table 3.4. The material properties of human rib trabecular bone are taken from the literature [28] and remain the same: Young's modulus $E = 0.04GPa$, yield stress $\sigma_y = 2.2MPa$, tangent modulus $E_t = 1MPa$, Poisson's ratio $\nu = 0.45$, density $\rho = 1g/cm^3$ and fracture plastic strain is equal to 0.03.

Table 3.4: Human rib cortical bone compressive and tensile material properties at two different strain rates, extracted from [91,92].

Material Properties	0.005 strain/s		0.5 strain/s	
	Compression	Tension	Compression	Tension
Young's modulus (GPa)	11.5	14.63	12.5	15.45
Yield Stress (MPa)	135	68.9	159	85.7
Ultimate Stress (MPa)	154	104.1	189	135.1
Ultimate Strain	0.0204	0.0247	0.0239	0.0292

3.2.3 Validation Tests and Sensitivity Studies

Validation tests of dynamic behaviors of porcine ribs under three point bending are conducted using an explicit non-linear FE software Radioss (Altair Hyperworks) by comparison with experimental data. The initial impact velocity of the striker bar is 17.39m/s, which is consistent with the experimental configuration. The simulations of ribs with average geometrical properties (i.e. length l=113.59mm, radius r=63.31mm, major axis 2a=10.07mm, minor axis 2b=9.78mm and constant cortical thickness h=(h_s+h_i)/2=1.5mm) and porcine rib material properties are conducted first.

Subsequently, sensitivity studies are carried out to investigate the effects of geometrical and mechanical parameters on dynamic behaviors of ribs. Different cortical thicknesses, curvature radiuses, lengths and cross sections are incorporated into the FE model for numerical analysis. Also, human rib cortical bone material properties from different loading modes (tension and compression) and strain rates (0.005 strain/s and 0.5 strain/s) are applied in the FE rib model. Comparisons between numerical results and experiments data of the literature are investigated and discussed in the following sections.

3.3 Results

This section presents the FE numerical results of dynamic behaviors of isolated porcine ribs submitted to high velocity impact using 3PB SHPB apparatus. Numerical results of strain signals, interface velocities, interface displacements, force-displacement relationship and fracture pattern are compared with experiments data of the literature.

Firstly, in order to validate the proposed FE model in this chapter, numerical results (with average geometrical properties) of various quantities using porcine rib material properties are first compared to the experimental data of the literature [31]. Fig. 3.5 (a)-(d) presents the comparative curves of experimental and numerical strain signals, interface velocities and interface displacements time histories, respectively. Considering that the rib model is a symmetric curved beam model with a constant elliptical cross section, only one output bar signal is plotted such as transmitted strain (Fig. 3.5b) and output interface velocity (Fig. 3.5c). Furthermore, experimental and numerical input interface force-displacement relationship curves are displayed in Fig. 3.6. Also, Fig. 3.7 shows the comparison of experimental and numerical fracture pattern at different absolute time values. It can be observed that numerical results correspond well with the experimental data in the literature even though there exists some discrepancies.

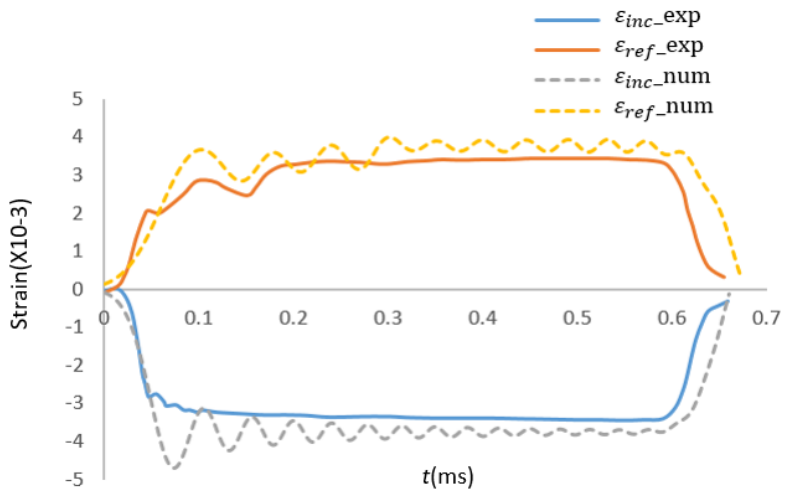

(a) Incident (ε_{inc}) and reflected (ε_{ref}) strains.

(continued)

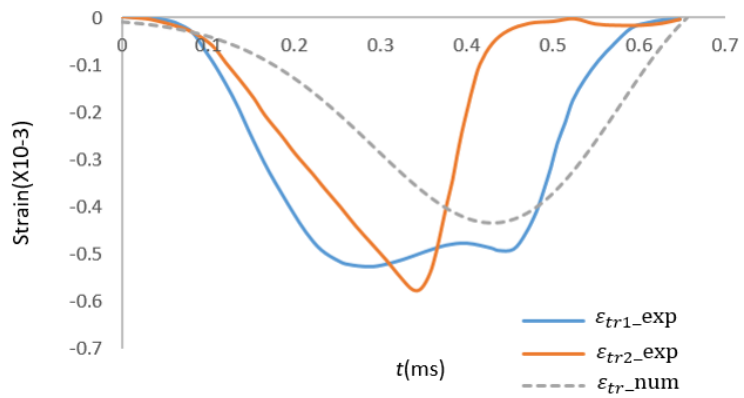

(b) Transmitted (ε_{tr}) strains.

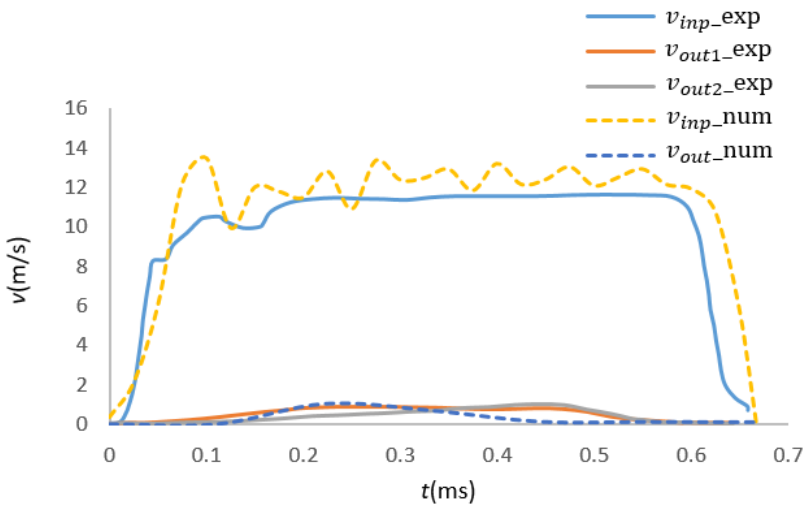

(c) Input (v_{inp}) and output (v_{out}) interface velocities.

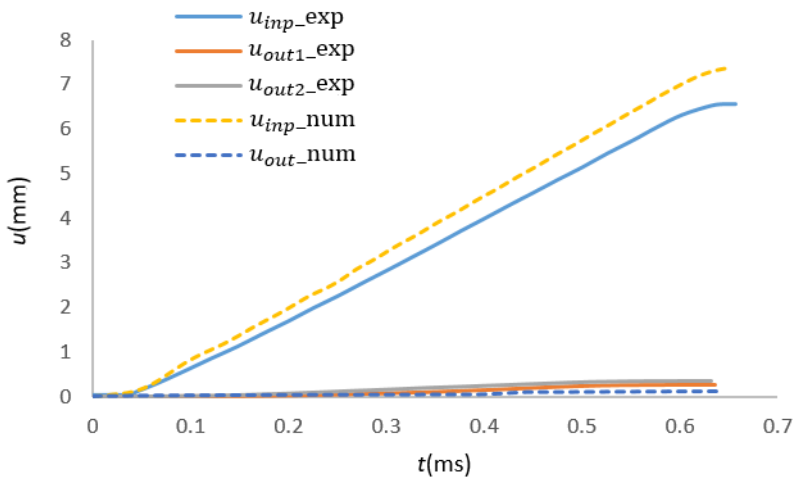

(d) Input (u_{inp}) and output (u_{out}) interface displacements.

Figure 3.5: Comparison of experimental and numerical (with average geometrical properties and porcine rib material properties) results of strains (a, b), velocities (c) and displacements (d).

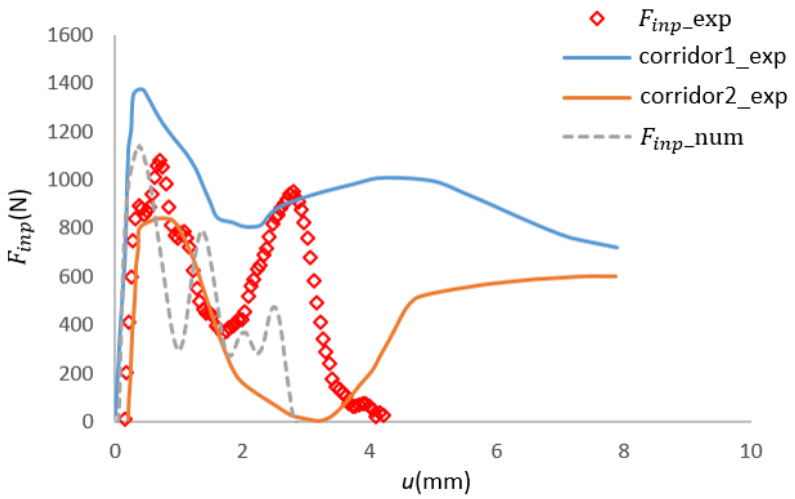

Figure 3.6: Comparison of experimental and numerical (with average geometrical properties and porcine rib material properties) input interface contact force (F_{inp}) versus displacement.

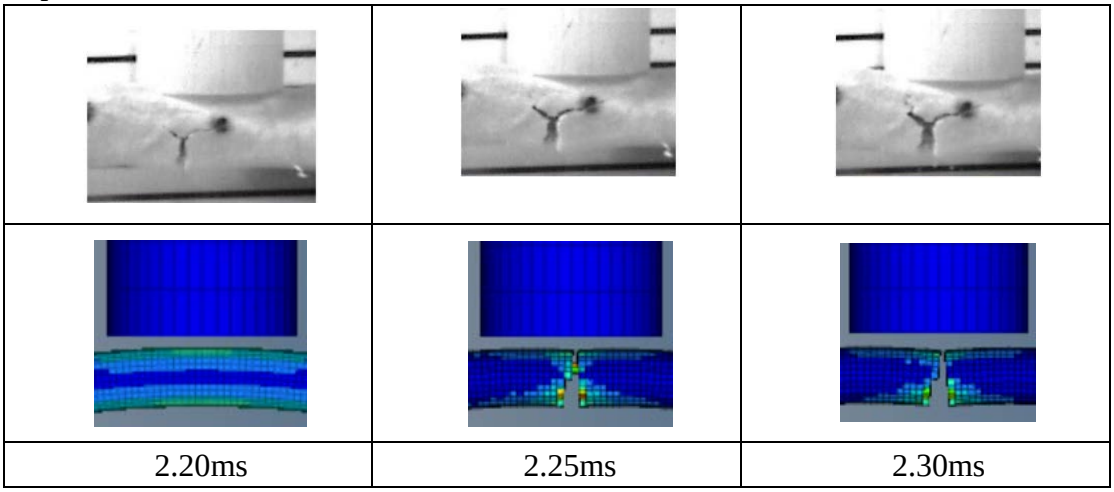

Figure 3.7: Comparison of experimental and numerical (with average geometrical properties and porcine rib material properties) fracture pattern at different absolute time values.

Next, sensitivity studies of different cortical thicknesses, curvature radiuses, lengths and cross sections are presented, in order to investigate the effect of geometrical parameters on dynamic behaviors of ribs. Fig. 3.8 displays experimental and numerical strain signals with different cortical thicknesses (num1, 2 and 3 correspond to cortical thickness h=1mm, 1.5mm and 2mm respectively). It is worth noting that in Fig. 3.8 (a) all the numerical incident strain signals superimpose because incident strain only depends on the characteristics of SHPB bars, therefore hereafter they are not plotted any more. Then, numerical reflected and transmitted strain curves versus time with diverse curvature radiuses, lengths and cross sections are illustrated in Fig. 3.9-Fig. 3.11, respectively. Similarly, Fig. 3.12-Fig. 3.14 separately provides the illustration of effect of the four different geometrical parameters on interface velocities, interface displacements and force-displacement relationships.

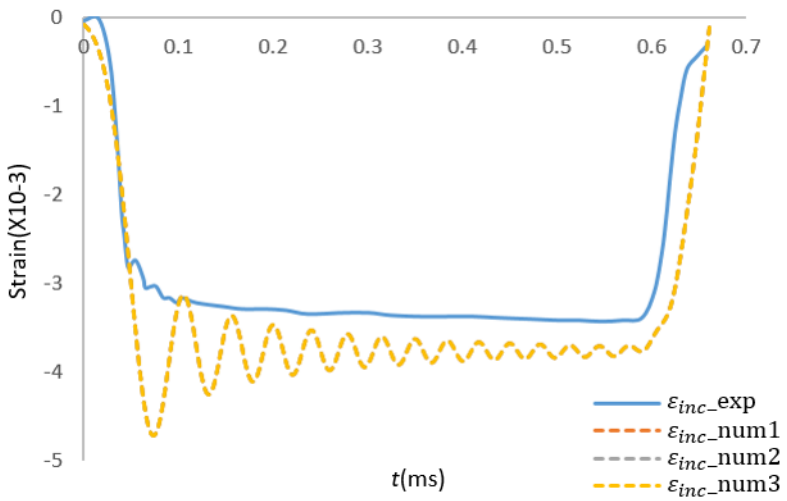

(a) Incident strain (ε_{inc}) time history.

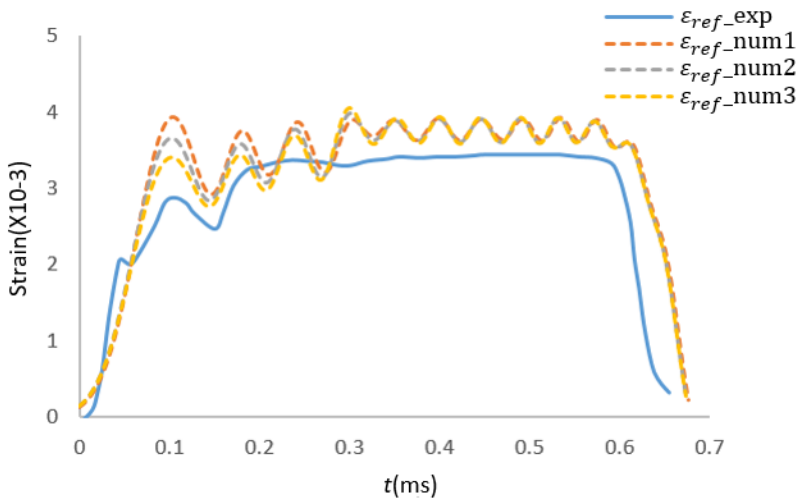

(b) Reflected strain (ε_{ref}) time history.

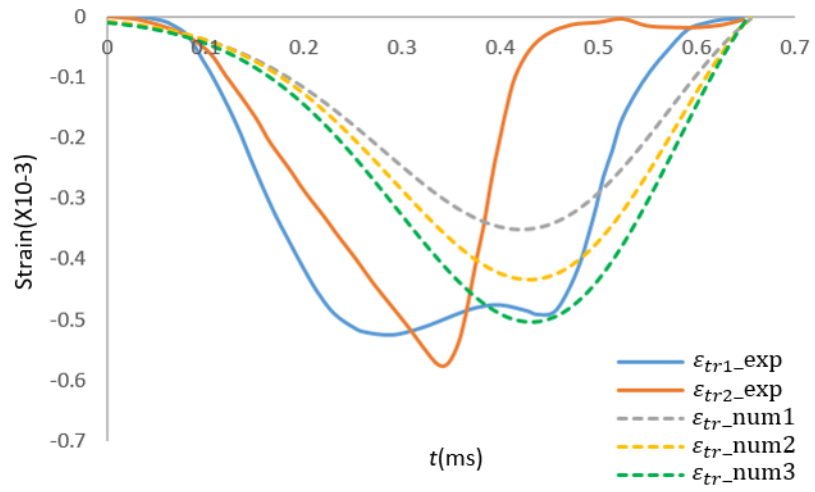

(c) Transmitted strain (ε_{tr}) time history.

Figure 3.8: Experimental and numerical strain signals using porcine rib material properties with different cortical thicknesses, where num1, 2 and 3 correspond to cortical thickness *h*=1mm, 1.5mm and 2mm respectively.

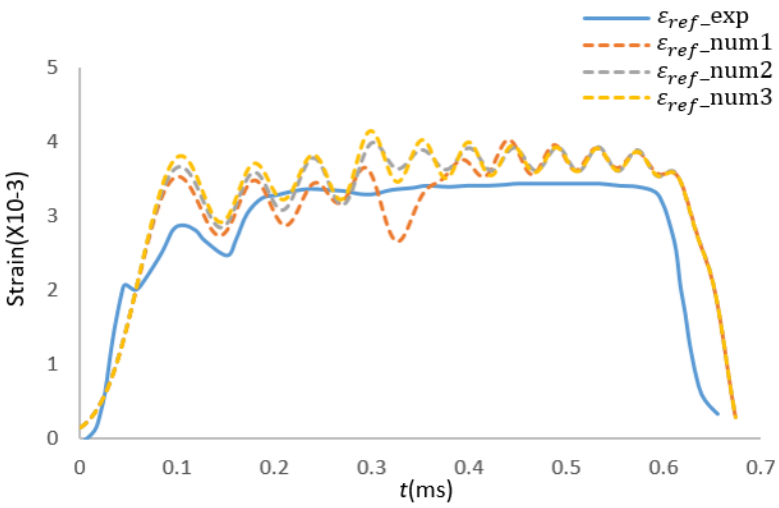

(a) Reflected strain (ε_{ref}) time history.

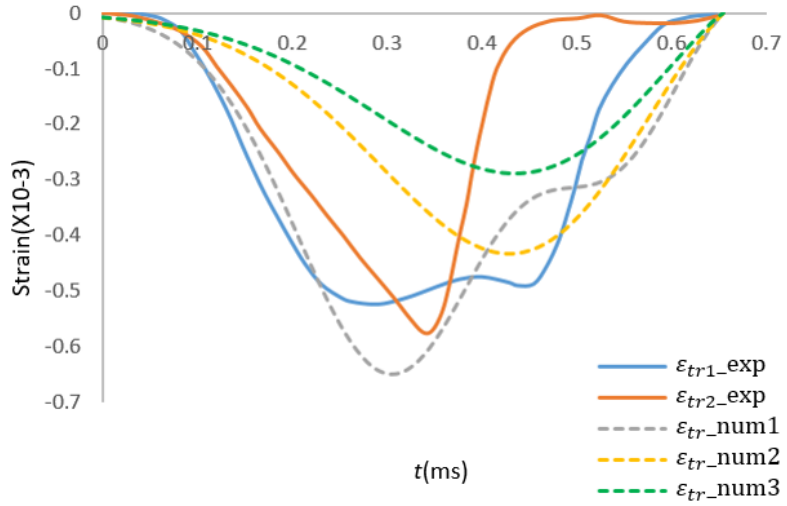

(b) Transmitted strain (ε_{tr}) time history.

Figure 3.9: Effect of curvature radiuses on reflected and transmitted strain signals using porcine rib material properties, where num1, 2 and 3 correspond to curvature radius *r*=56.80mm, 63.31mm and 70mm respectively.

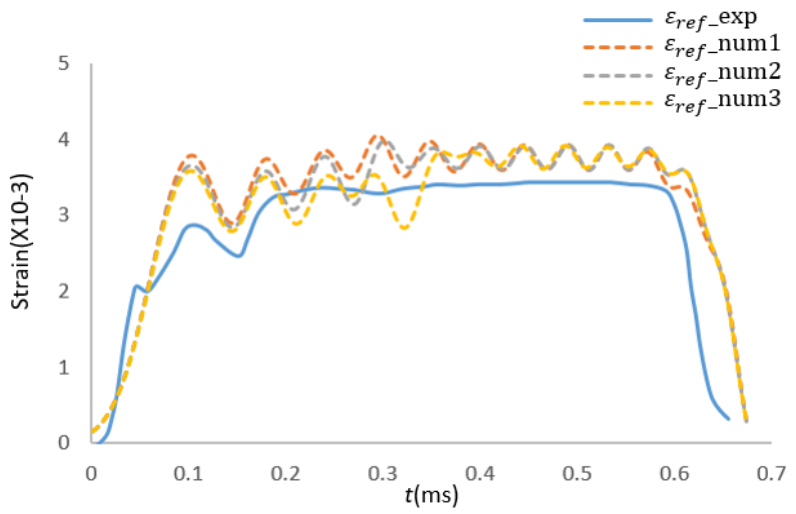

(a) Reflected strain (ε_{ref}) time history.

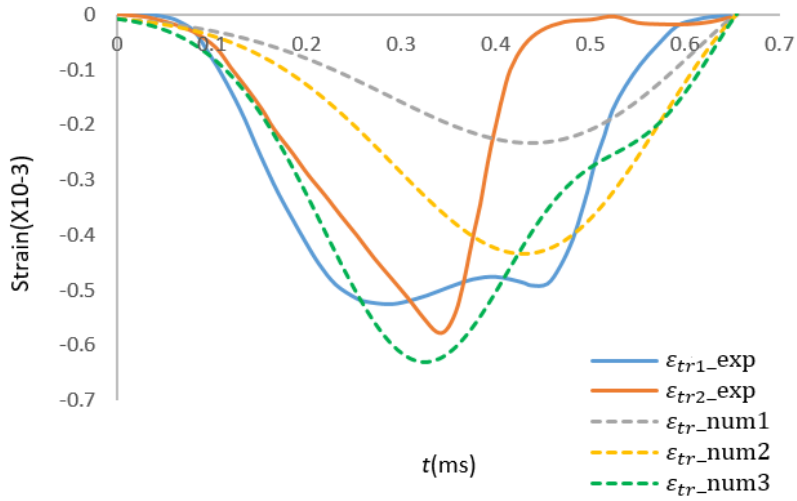

(b) Transmitted strain (ε_{tr}) time history.

Figure 3.10: Effect of lengths on reflected and transmitted strain signals using porcine rib material properties, where num1, 2 and 3 correspond to length *l*=103mm, 113.59mm and 124mm respectively.

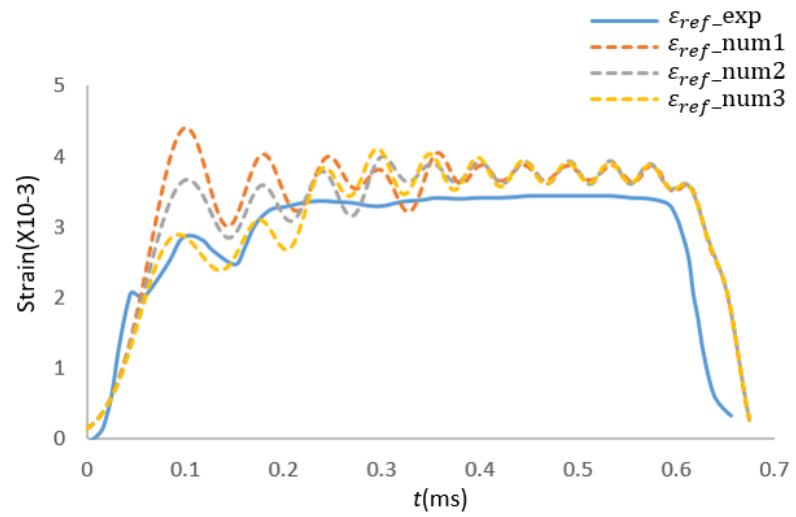

(a) Reflected strain (ε_{ref}) time history.

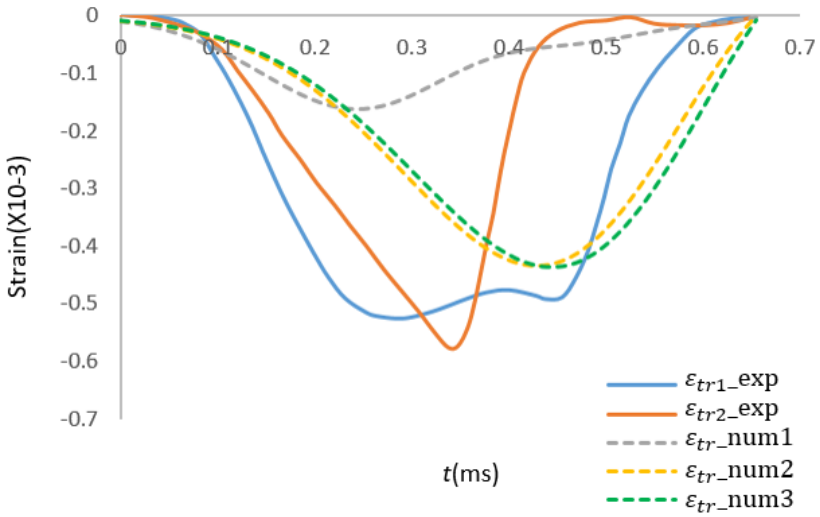

(b) Transmitted strain (ε_{tr}) time history.

Figure 3.11: Effect of rib cross sections on reflected and transmitted strain signals using porcine rib material properties, where num1, 2 and 3 correspond to cross section 2*a*=7mm, 2*b*=6.7mm; 2*a*=10.07mm, 2*b*=9.78mm and 2*a*=13mm, 2*b*=12.7mm respectively.

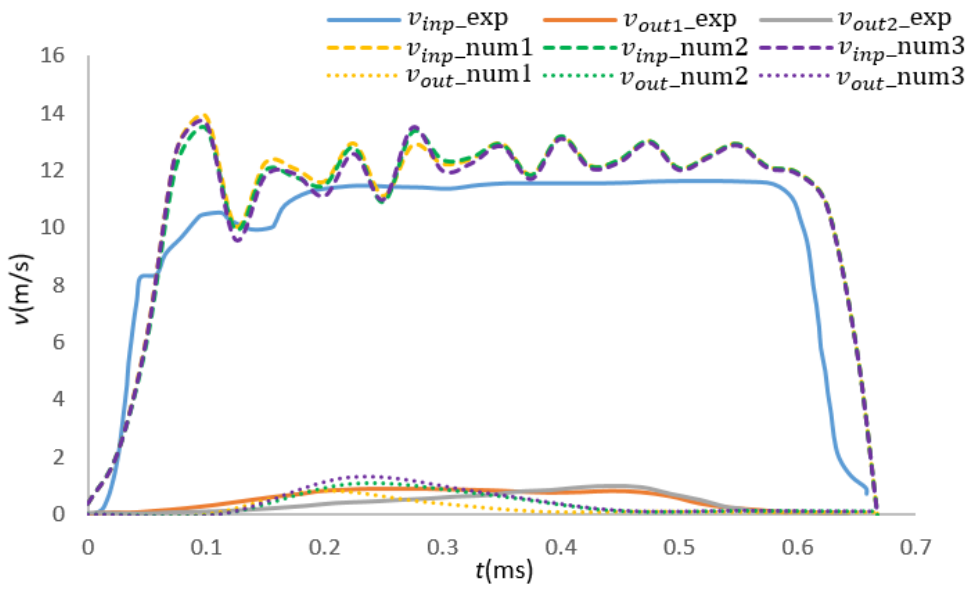

(a) Interface velocities (v_{inp},v_{out}) with different cortical thicknesses (num1, num2 and num3 correspond to cortical thickness *h*=1mm, 1.5mm and 2mm respectively).

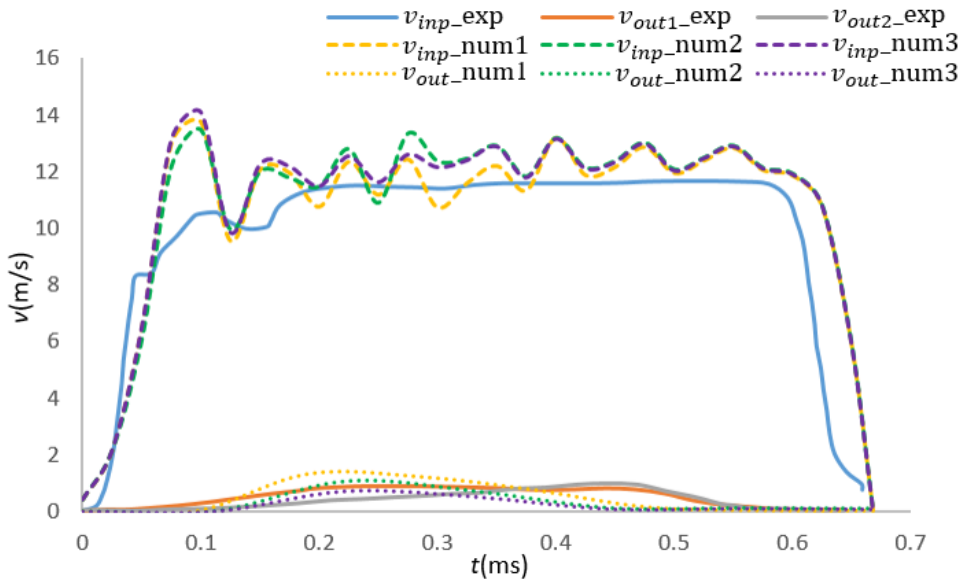

(b) Interface velocities (v_{inp},v_{out}) with different curvature radiuses (num1, 2 and 3 correspond to curvature radius *r*=56.80mm, 63.31mm and 70mm respectively).

(continued)

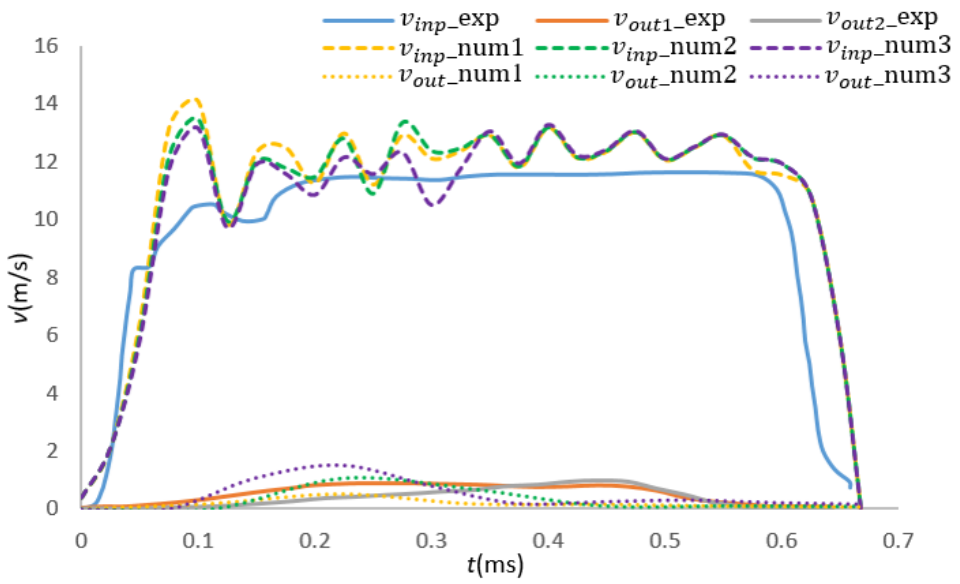

(c) Interface velocities (v_{inp},v_{out}) with different lengths (num1, 2 and 3 correspond to length l=103mm, 113.59mm and 124mm respectively).

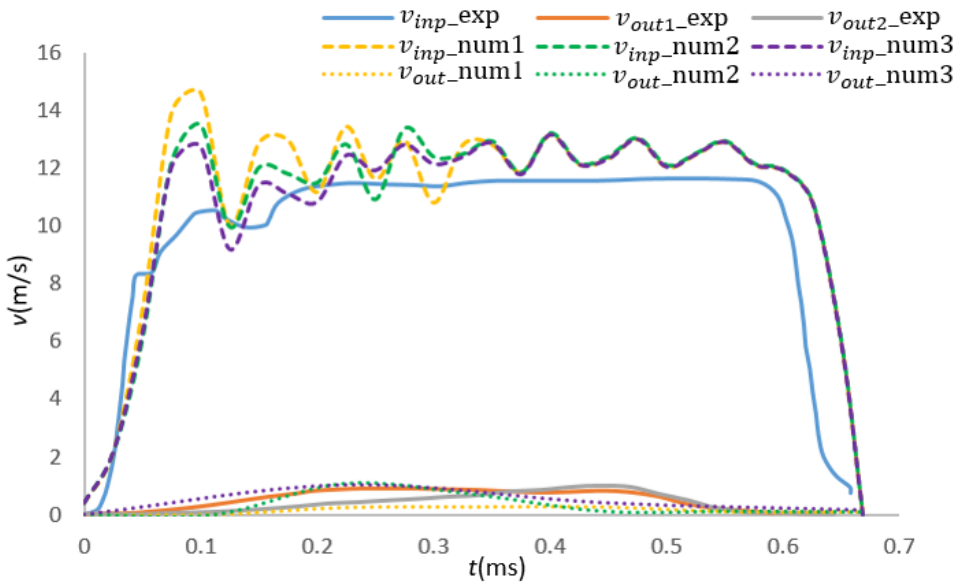

(d) Interface velocities (v_{inp}, v_{out}) with different cross sections (num1, 2 and 3 correspond to cross section 2a=7mm, 2b=6.7mm; 2a=10.07mm, 2b=9.78mm and 2a=13mm, 2b=12.7mm respectively).

Figure 3.12: Illustration of the effect of various geometrical parameters on input (v_{inp}) and output (v_{out}) interface velocities with porcine rib material properties.

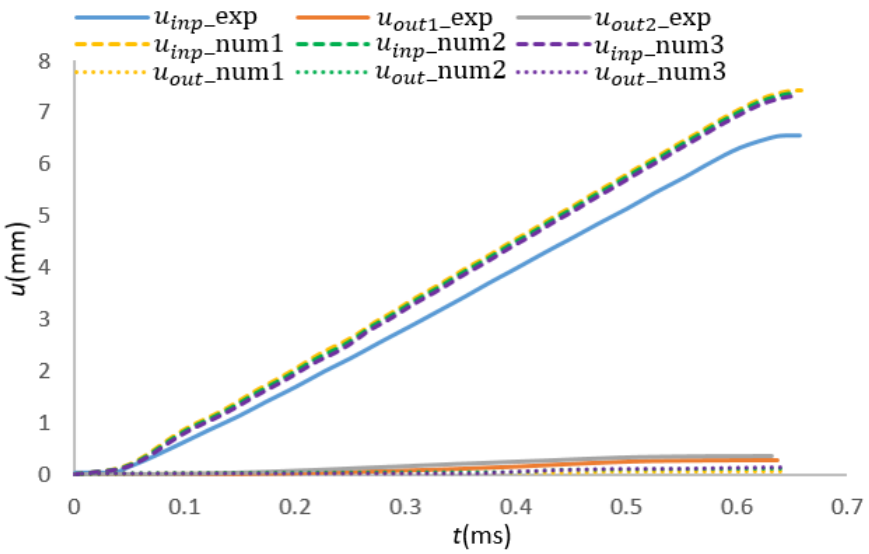

(a) Interface displacements (u_{inp}, u_{out}) with different cortical thicknesses (num1, num2 and num3 correspond to cortical thickness *h*=1mm, 1.5mm and 2mm respectively).

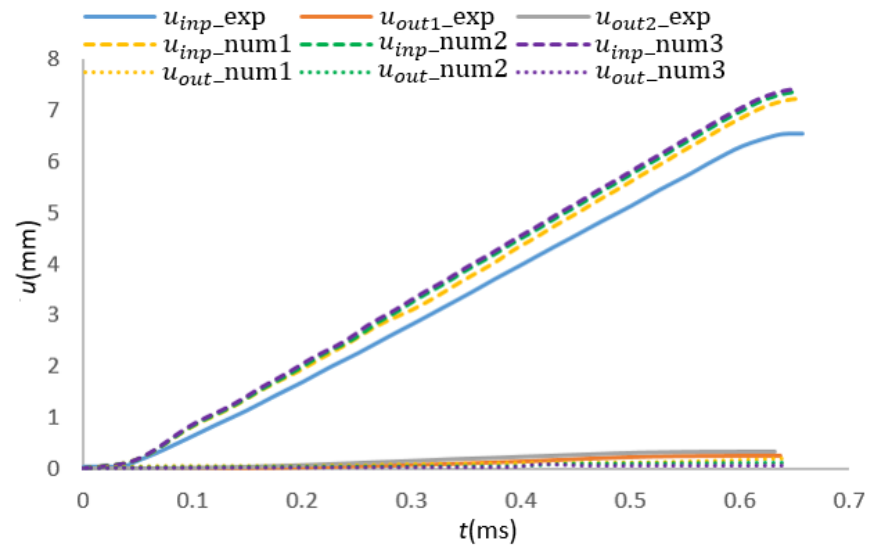

(b) Interface displacements (u_{inp}, u_{out}) with different curvature radiuses (num1, 2 and 3 correspond to curvature radius *r*=56.80mm, 63.31mm and 70mm respectively).

(continued)

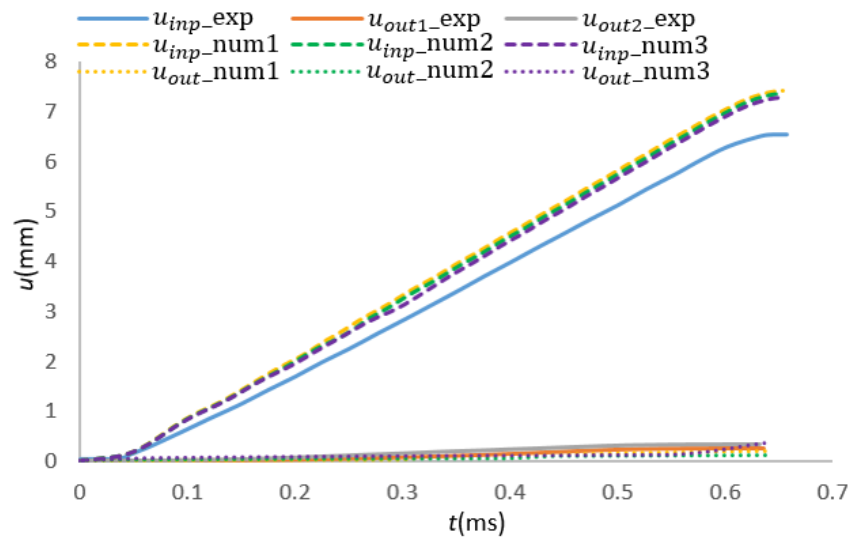

(c) Interface displacements (u_{inp}, u_{out}) with different lengths (num1, 2 and 3 correspond to length *l*=103mm, 113.59mm and 124mm respectively).

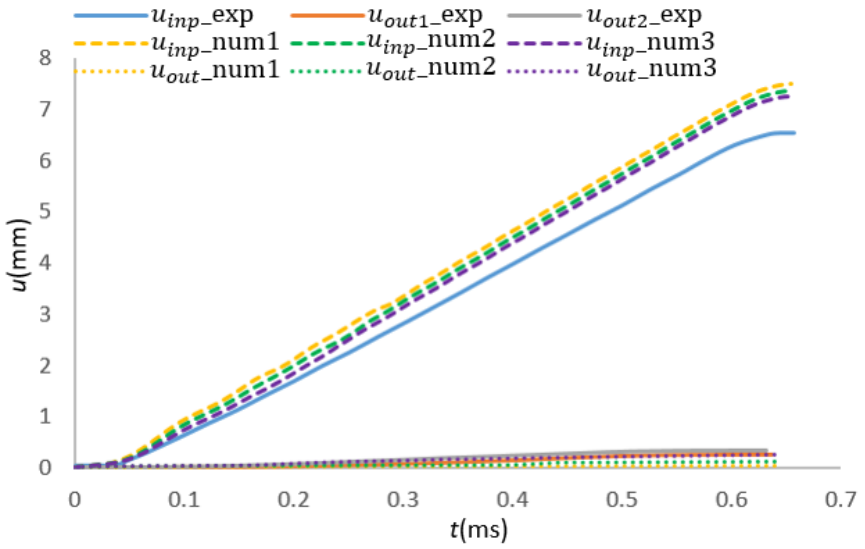

(d) Interface displacements (u_{inp}, u_{out}) with different cross sections (num1, 2 and 3 correspond to cross section 2*a*=7mm, 2*b*=6.7mm; 2*a*=10.07mm, 2*b*=9.78mm and 2*a*=13mm, 2*b*=12.7mm respectively).

Figure 3.13: Illustration of the effect of various geometrical parameters on input (u_{inp}) and output (u_{out}) interface displacements with porcine rib material properties.

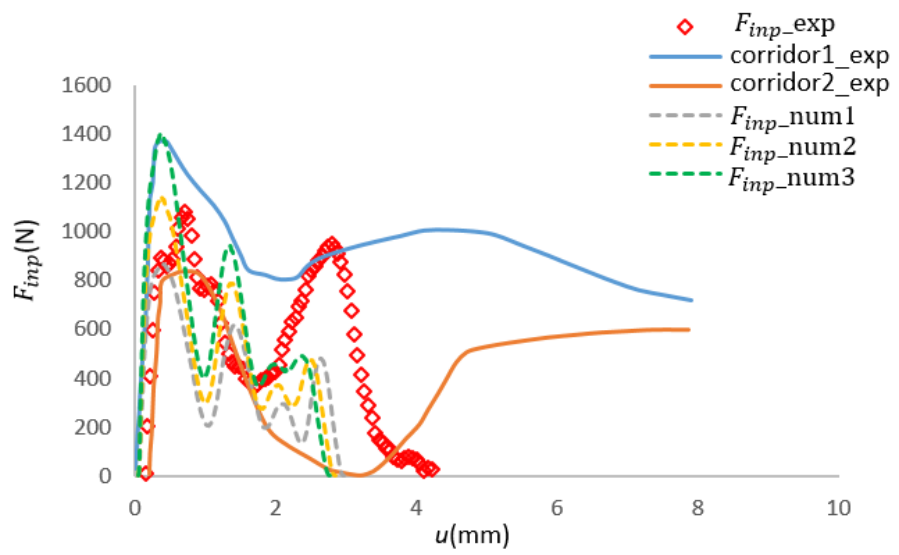

(a) Force-displacement relationship with different cortical thicknesses (num1, num2 and num3 correspond to cortical thickness h=1mm, 1.5mm and 2mm respectively).

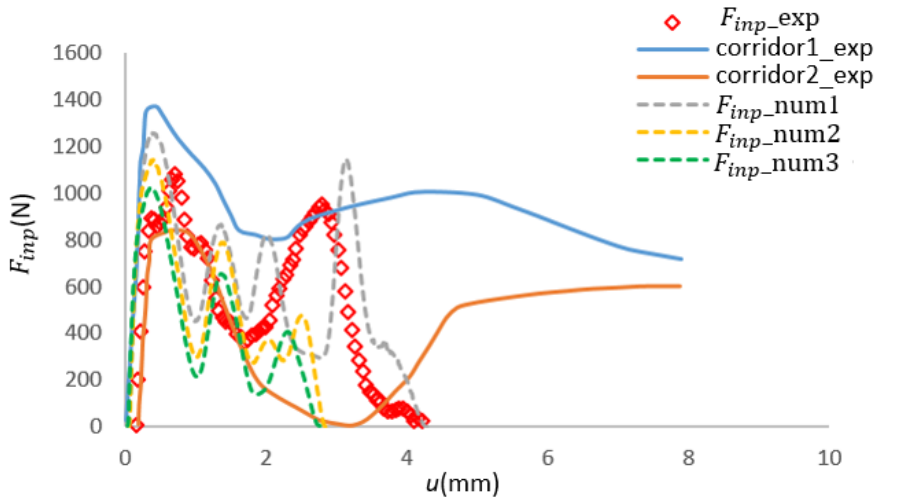

(b) Force-displacement relationship with different curvature radiuses (num1, 2 and 3 correspond to curvature radius r=56.80mm, 63.31mm and 70mm respectively).

(continued)

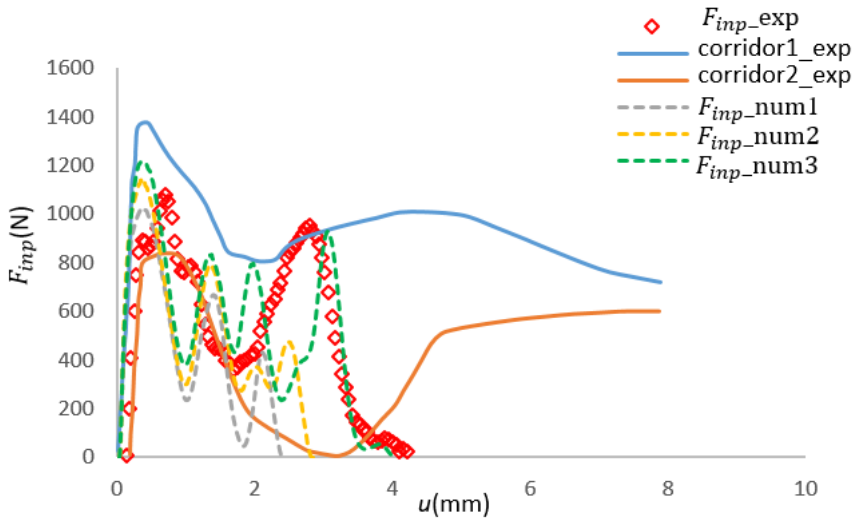

(c) Force-displacement relationship with different lengths (num1, 2 and 3 correspond to length l=103mm, 113.59mm and 124mm respectively).

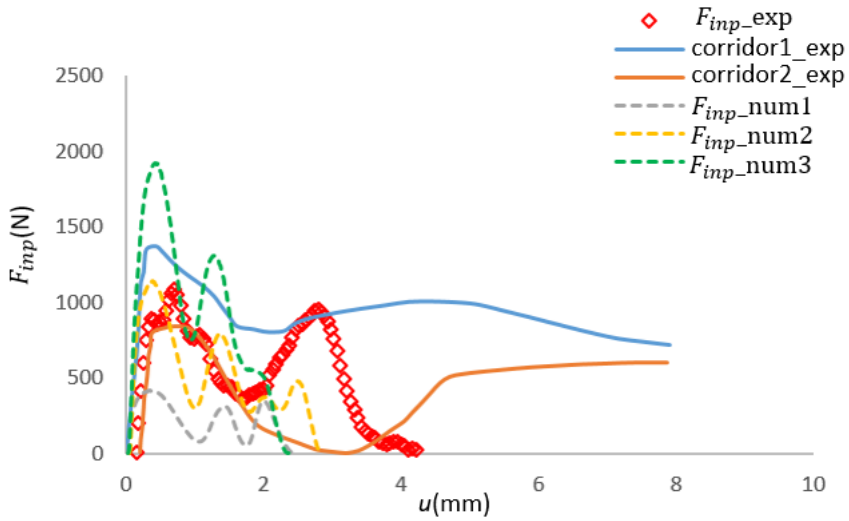

(d) Force-displacement relationship with different cross sections (num1, 2 and 3 correspond to cross section 2a=7mm, 2b=6.7mm; 2a=10.07mm, 2b=9.78mm and 2a=13mm, 2b=12.7mm respectively).

Figure 3.14: Illustration of the effect of various geometrical parameters on input interface force (F_{inp})-displacement relationship with porcine rib material properties.

In addition, human rib cortical bone material properties from different loading modes (tension and compression) and strain rates (0.005 strain/s and 0.5 strain/s) are also applied in order to study the effect of mechanical parameters on dynamic behaviors of isolated ribs. Numerical strains, interface velocities and displacements with human rib cortical bone material properties from different loading modes and strain rates are displayed in Fig. 3.15 (a)-(d), respectively. Fig. 3.16 presents the numerical input interface force-displacement curves compared to experimental corridors. Moreover,

comparisons of numerical fracture patterns with different human rib cortical bone material properties are illustrated in Fig. 3.17.

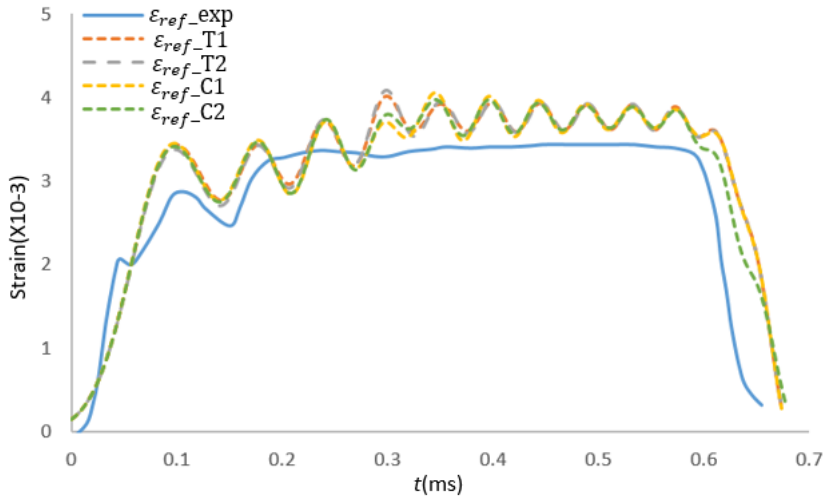

(a) Reflected (ε_{ref}) strains.

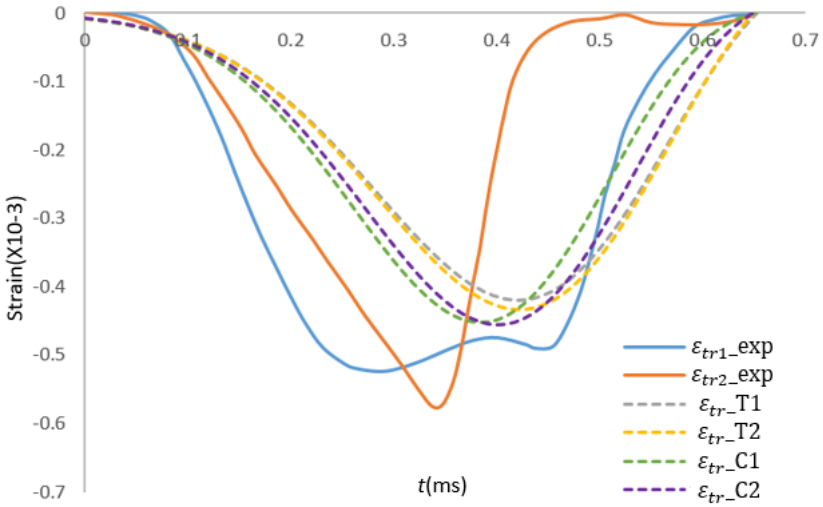

(b) Transmitted (ε_{tr}) strains.

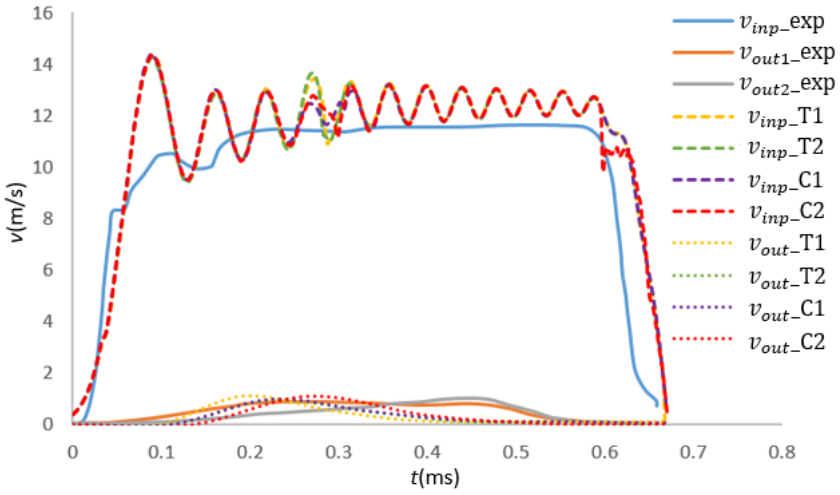

(c) Input (v_{inp}) and output (v_{out}) interface velocities.

(continued)

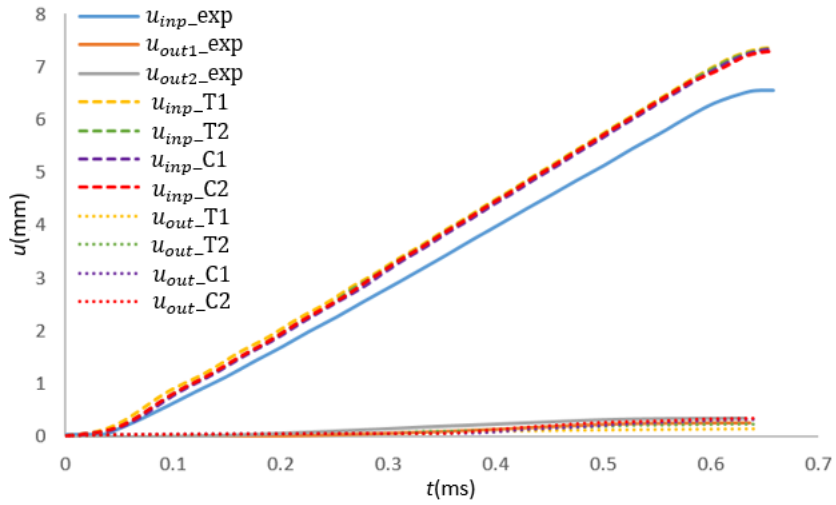

(d) Input (u_{inp}) and output (u_{out}) interface displacements.

Figure 3.15: Illustration of numerical strains (a, b), velocities (c) and displacements (d) with human rib cortical bone material properties from different loading modes and strain rates compared with experimental data, where 'T1', 'T2', 'C1' and 'C2' represent human rib cortical bone tensile material properties at 0.005 strain/s and 0.5 strain/s and human rib cortical bone compressive material properties at 0.005 strain/s and 0.5 strain/s, respectively.

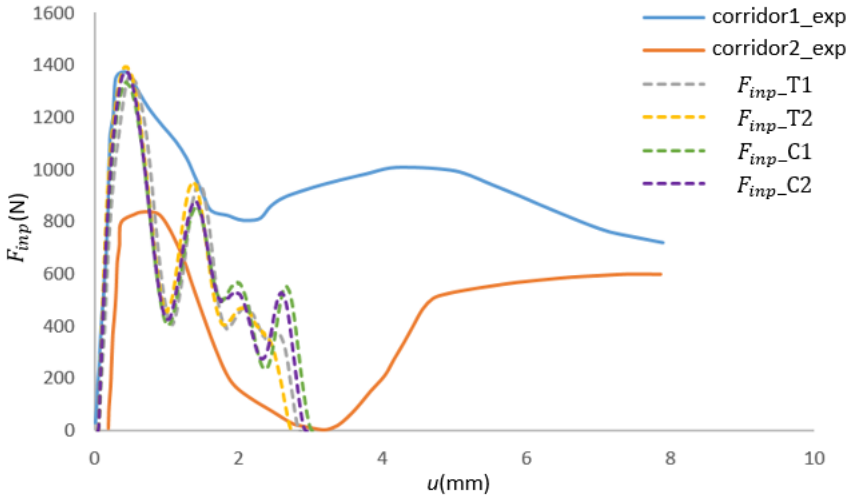

Figure 3.16: Numerical input interface force (F_{inp})-displacement curves with various human rib cortical bone material properties compared with experimental corridors, where 'T1', 'T2', 'C1' and 'C2' represent human rib cortical bone tensile material properties at 0.005 strain/s and 0.5 strain/s and human rib cortical bone compressive material properties at 0.005 strain/s and 0.5 strain/s, respectively.

(a) Tension, 0.005 strain/s	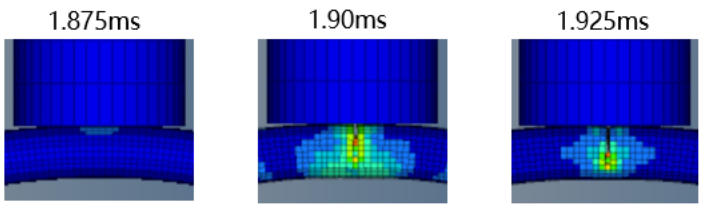
(b) Tension, 0.5 strain/s	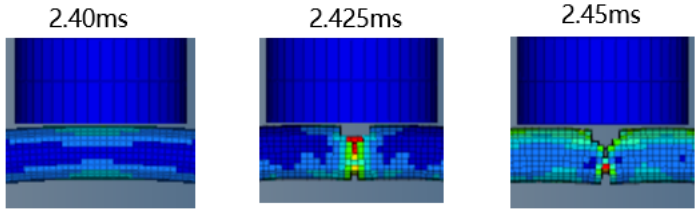
(c) Compression, 0.005 strain/s	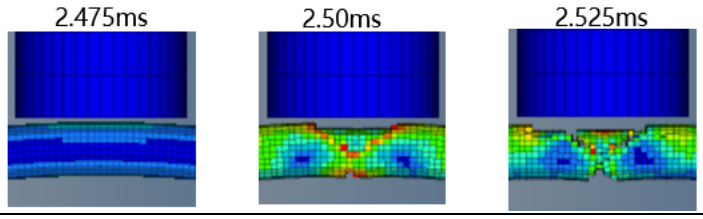
(d) Compression, 0.5 strain/s	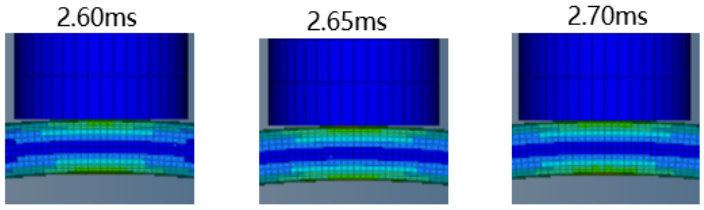

Figure 3.17: Illustration of numerical fracture patterns with different human rib cortical bone material properties.

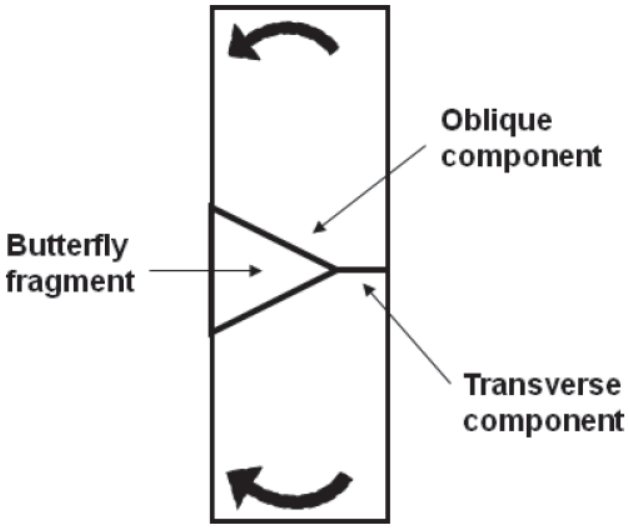

Figure 3.18: Schematic of butterfly fracture, extracted from [82].

3.4 Discussion

Numerical results and investigations of dynamic behaviors of isolated porcine ribs submitted to high velocity impact using 3PB SHPB apparatus are presented in this study.

Comparative and sensitivity studies are conducted in order to validate the feasibility of the developed FE model and methodology, and to investigate the effects of geometrical and mechanical parameters on dynamic behaviors of ribs.

Firstly, numerical results (with average geometrical properties) consisting of strain signals, interface velocities and interface displacements time histories with porcine rib material properties are displayed in Fig. 3.5 (a)-(d), respectively. It can be seen that the numerical curves have a good correlation with the experimental ones, although the transmitted strain is slightly inferior to the experimental value. The input interface force-displacement relationship in Fig. 3.6 indicates that the numerical structural response of rib is within the experimental corridors while it is relatively inferior to experimental data. Also, experimental and numerical fracture patterns in Fig. 3.7 share some common characteristics. That is, the fracture location is similar, the crack origins at the surface subjected to tension towards the impact point, and the fracture pattern is Mode-I crack. It is also worth noting that the strain signals are essential measurement quantities in SHPB tests, and numerical incident, reflected and transmitted strains have a good match with experimental data in Fig. 3.5(a)-(b). Therefore, the curved beam rib model with a constant elliptical cross section developed in this study is demonstrated to be efficient for modeling ribs under high velocity impact, as numerical results correspond well with the experimental data in the literature even if there exists some discrepancies. These discrepancies may be explained by the geometrical differences between FE rib model and real rib geometry characteristics. Actually, previous studies carried out by Niu et al. [142] also proved the ability of rib beam model to study blunt trauma caused by high speed impacts.

Subsequently, as is mentioned previously, comparative sensitivity studies of different cortical thicknesses, curvature radiuses, lengths and cross sections are discussed, in order to investigate the effect of geometrical parameters on dynamic behaviors of ribs. First of all, numerical incident reflected and transmitted strains with different cortical thicknesses are compared in Fig. 3.8, it is evident in Fig. 3.8(a) that all the numerical incident strains superimpose because incident strain only depends on the characteristics of SHPB bars. Also, with the increase of cortical thickness, it can be seen from Fig. 3.8(b) that reflected strain has a slight decrease in early time and then they are superimposed. While the transmitted strain in Fig. 3.8(c) is sensitive to cortical thickness, it has an increasing tendency when cortical thickness increases. In addition, Fig. 3.9-Fig. 3.11 depict numerical reflected and transmitted strain time histories with variable curvature radiuses, lengths and cross sections, respectively. Fig. 3.9(a) and Fig. 3.10(a) indicate that the reflected strain is not sensitive to the increase of curvature radius and length. However, it reveals that transmitted strain shows a significantly decrease trend when curvature radius increases, as illustrated in Fig. 3.9(b), and an increase trend when rib length increases as illustrated in Fig. 3.10(b). With the increase of cross section, the reflected strain in Fig. 3.11(a) has a similar slight influence as

shown in Fig. 3.8(b), but the transmitted strain value reduces as the cross section reduces. In short, the transmitted strain signals are sensitive to the variations of the geometrical parameters of ribs.

Similarly, Fig. 3.12 and Fig. 3.13 separately provide the illustration of the effect of the aforementioned four different geometrical parameters on interface velocities and displacements. It can be observed in Fig. 3.12(a) that interface velocities are insensitive to the change of cortical thickness, but Fig. 3.12(b) indicates that input interface velocities raise slightly with the increase of curvature radius. Fig. 3.12(c)-(d) show a moderate reduction of input interface velocity when rib length and cross section increase. In Fig. 3.13 (a)-(d), interface displacements have consistent variation tendencies as interface velocities in Fig. 3.12 (a)-(d) because of the positive correlation relationship between displacement and velocity. Also, the effect of various geometrical parameters on input interface force-displacement relationship is investigated in Fig. 3.14 (a)-(d). It can be seen in Fig. 3.14(a)-(d) that input interface force increases with the increase of cortical thickness, length and cross section, in contrary, it decreases with the increase of curvature radius. In particular, it is deserved to note the influence of change of cross section on the force magnitude (in Fig. 3.14(d)). This can be explained by the change of contact area between rib extremity and the SHPB bar. In addition, configuration num1 (curvature radius r=56.80mm, length l=113.59mm) in Fig. 3.14(b) and configuration num3 (curvature radius r=63.31mm, length l=124mm) in Fig. 3.14(c) have a better relevancy compared to experimental curves, which points out that the curved beam rib model with a r/l ratio close to 0.5 presents a better force-displacement relationship.

In summary, Table 3.5 illustrates the effect of various geometrical parameters on the dynamic behaviors of the ribs (symbol '-', '+' and '++' signify no evident influence, slight influence and significant influence respectively), which can bring interesting information to study the morphological and anthropometrical aspects and the variability of the human body under dynamic loadings.

Table 3.5: The effect of various geometrical parameters on dynamic behaviors of isolated ribs with porcine rib material properties.

	Cortical thickness	Curvature radius	Length	Cross section
Reflected strain	-	-	-	+
Transmitted strain	+	++	++	++
Interface velocity	-	+	+	+
Interface displacement	-	+	+	+
Force-displacement relationship	+	++	++	++

Moreover, human rib cortical bone material properties from different loading modes

(tension and compression) and strain rates (0.005 strain/s and 0.5 strain/s) were also applied in order to study the effect of mechanical parameters on dynamic behaviors of isolated ribs. It can be seen that numerical strains, interface velocities and displacements with different human rib cortical bone material properties in Fig. 3.15 (a)-(d) have a good match with the experimental data and are insensitive to the variations of cortical bone material properties. The input interface force-displacement curves in Fig. 3.16 are also within the experimental corridors and do not differ a lot. The agreement between numerical and experimental results in Fig. 3.15 and Fig. 3.16 indicates the similarity between porcine rib and human rib material properties. However, the numerical fracture patterns differ a lot with human rib cortical bone material properties from different loading modes (tension and compression) and strain rates (0.005 strain/s and 0.5 strain/s) as shown in Fig. 3.17 (a)-(d). Fig. 3. 17 (a)-(b) and Fig. 3.17 (c)-(d) reveal that with cortical bone material properties from the same loading mode (tension or compression), the rib fractures later (Fig. 3.17(b)) or even does not fracture (Fig. 3.17(d)) because the ultimate stress increases with the increase of the strain rate. In addition, it can be seen that with the same strain rate, the rib fractures later (Fig. 3.17(c)) or even does not fracture (Fig. 3.17(d)) because the rib cortical bone ultimate stress is higher in compression than in tension as displayed in Table 3.4. Therefore, it is needed to consider the effect of mechanical parameters like loading mode and strain rate sensitivity in FE models when investigating rib dynamic behaviors. It also deserves to note that the butterfly fractures are observed in Fig. 3.17 (b)-(c), which were observed when causing an extension of the rib curve in ventrally applied blast experiments conducted by Christensen et al. [81,82]. The butterfly fracture pattern consists of transverse in part and oblique in part and produces a triangular fragment as illustrated in Fig. 3. 18. Actually, the 3PB tests on ribs cause the extension of the rib curve which resemble a ventrally applied blast scenario. The butterfly fracture pattern may be used as an indicator to investigate the body position in blast events for forensic pathologists. Further FE numerical simulations could also be performed to study rib fractures under blast impacts.

Overall, the objective of this study is to investigate the effect of geometrical and mechanical parameters of ribs submitted to high velocity impact. A curved beam rib model with a constant elliptical cross section was developed to simulate dynamic behaviors of ribs under 3PB using the SHPB apparatus. The aforementioned numerical sensitivity studies reveal that geometrical parameters of ribs play an important role in influencing dynamic behaviors of ribs. It is also needed to consider the effect of mechanical parameters like loading mode and strain rate sensitivity in FE models when investigating rib dynamic behaviors. The developed curved beam rib FE model and methodology have been validated and provide interesting ways to simulate ribs under high-velocity impacts. However, there still exists some limitations in this study. First, a constant cortical thickness is used here, actually the cortical thickness is variable throughout the rib. Such simplification may cause some inaccuracies of numerical

results, thus ribs with regional variable cortical thickness are more biofidelic and provide more accurate predictions. Also, apart from applying a built-in failure criterion in the material model based on the maximum fracture plastic strain to represent rib fracture, additional failure models could be added to the material model to simulate rib fracture, while the failure constants are acquired by fitting experimental data and sometimes must be deduced from simulations.

3.5 Conclusion

In this chapter, the dynamic behaviors of porcine ribs under 3PB are studied using finite element simulations. Based on experimental data of the literature, the numerical curved beam rib models are validated and show biofidelic behaviors. In addition, sensitivity studies are conducted on geometrical and mechanical parameters, in order to investigate their effects on the mechanical responses. Numerical analysis highlighted the significant effect of geometrical parameters on dynamic behaviors of ribs. The consideration of the effect of mechanical parameters like loading mode and strain rate sensitivity in FE rib models is also needed. Porcine ribs are usually used as human rib surrogates because they share similar geometrical and anatomical characteristics. This work is an interesting way to study the human rib dynamic behaviors at a numerical level, and these ribs models can be further implemented in a more global thoracic biomechanical model for human trauma investigations.

4 Validation of Rib Structural Responses under Dynamic Loadings with Different Material Properties Using Finite Element Analysis

4.1 Introduction

Rib fractures are a major injury pattern in thoracic injuries during MVCs, better understanding rib fractures has become a challenge for vehicle safety researchers. In order to mimic real-world frontal impact loading in motor vehicle crashes (MVCs), many researchers conducted experiments and numerical simulations of individual ribs under dynamic anterior-posterior bending. Previous numerical studies defined human rib cortical bone material models using material data obtained from tensile coupon tests because of the absence of rib cortical bone compressive material properties in the literature. Actually, the rib suffers both tensile and compressive loading modes during MVCs, for instance, the cutaneous surface suffers tension while the pleural surface suffers compression in frontal crash conditions. Recently, Albert et al. [92] first experimentally quantified human rib cortical bone compressive material properties at two different strain rates (0.5 strain/s and 0.005 strain/s). Consequently, the purpose of this chapter is to develop rib FE models with various material properties including human rib cortical bone material properties from different loading modes (tension and compression), strain rates (0.5 strain/s and 0.005 strain/s) and ages as well as porcine rib material properties, and validate them through replicating experimental configurations, in order to better understand rib structural properties and fracture locations under dynamic anterior-posterior bending. Meanwhile, comparison and analysis of the effect of human rib cortical bone material properties from different loading modes (tension and compression), strain rates, ages and porcine rib material properties on rib structural responses were investigated. Numerical force-displacement relationship, cortical strain, rotation, and fracture locations correspond well with published experimental data, which demonstrates the robustness of the finite element rib models. Numerical analysis reveals that numerical strain and rotation time histories with human rib cortical compressive material properties have a better correlation with experimental data compared to those with human rib cortical tensile material properties. Also, numerical rib structural responses were found to be sensitive to human cortical bone material properties from different loading modes, strain rates and ages. Therefore,

it is necessary to consider the effect of material properties from different loading modes, strain rates and ages when establishing rib FE models. Meanwhile, it is also revealed that porcine rib material properties can obtain similar and reasonable results compared to human rib material properties. This was the first numerical study to apply human rib compressive material properties in investigating rib dynamic structural responses and compare the results with those from tensile material properties. The present study helps better understand human rib fractures in a high velocity impact (HVI) context in a numerical way.

The outline of this chapter is organized as follows. In Section 4.2, experimental setup of individual ribs under anterior-posterior bending is introduced first. Then, finite element modeling of FE rib models is presented, and validation tests are conducted as well. Section 4.3 displays comparative results between FE simulations and experimental data. Subsequently, Section 4.4 discusses the obtained FE results and finally Section 4.5 summarizes the major conclusions.

4.2 Materials and Methods

4.2.1 Configurations of the Experiments

In this study, the 6th level rib was first simulated under dynamic anterior-posterior bending where the sternal (anterior) end of the rib was pushed towards the vertebral (posterior) end within rib's major plane (x-y plane). Experimental configurations used in this study were conducted in Ohio State University by Agnew et al. [108]. The experimental setup is shown in Fig. 4.1, both ends of the rib were potted in Bondo Body Filler (Bondo Corporation, Atlanta, GA), and the two potted ends were fixed in rotating cups which can rotate freely perpendicular to the loading plane. A pendulum with a mass of 54.4kg impacted the sternal end of the rib with initial velocity near 2m/s, to push the sternal end towards the vertebral end along x direction. Moving displacement of the sternal end was recorded by a linear string potentiometer which was positioned on the moving plate of the fixture. The reaction force of the vertebral end of the rib was measured by a load cell attached behind the fixed plate. Also, the rotations of both end cups were measured by rotational potentiometers. Four strain gauges (marked by four stars in Fig. 4.1) were attached to the cutaneous (CSG1, CSG2) and pleural (PSG1, PSG2) surfaces, at 30% and 60% of the rib curve length counted from vertebral end respectively.

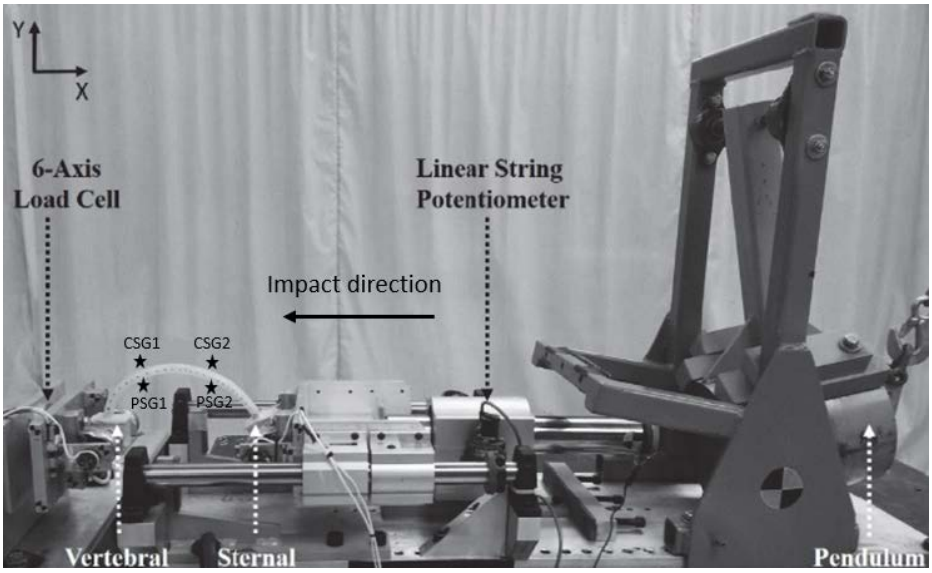

Figure 4.1: Schematic of experimental setup of rib under anterior-posterior bending by impacts using pendulum fixture, adapted from [108].

In addition, to prove the robustness of the finite element rib models, another experimental scenario with initial offset performed by Li et al. 2010 [28,29] and Kindig 2009 [78] was reproduced and simulated as well. Ribs of level 2 to 10 were displaced under anterior-posterior bending. As shown in Fig. 4.2, an offset y_0 between anterior and posterior end was set to represent the distance of costal cartilage. Both rib extremities were potted and connected with loading fixture through rotational pin joints, the posterior extremity was fully constrained except for the rotational degree of freedom around z axis. Displacement applied to the anterior extremity was at a velocity near 1m/s by loading piston. Reaction force of the posterior extremity was measured by a load cell behind the fixed base. Six strain gauges were used to measure deformation on both sides of cutaneous and pleural surfaces. It can be seen in Fig. 4.2 that SG2 is located at the furthest point from the anterior-posterior axis, SG1 and SG3 were respectively at the midpoint between SG2 and the two extremities.

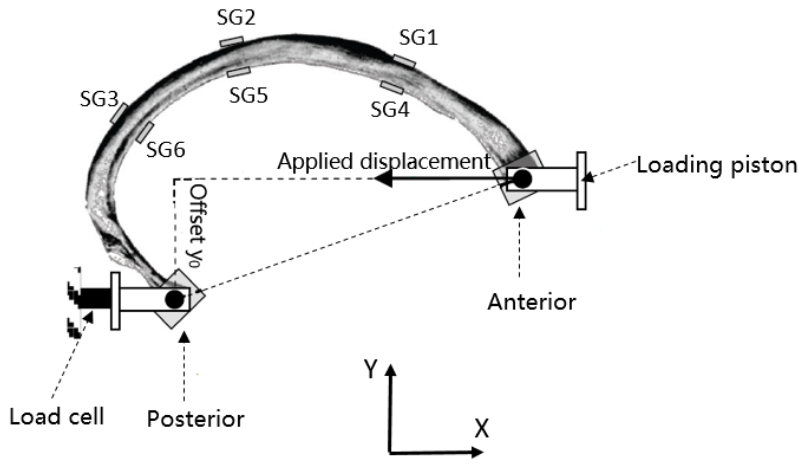

Figure 4.2: Schematic of experimental setup with initial offset, adapted from [29].

4.2.2 Finite Element Modeling

4.2.2.1 Biomechanical Rib Model

The finite element rib models utilized in this study were extracted from a biomechanical thorax model (HUByx model) developed by Roth et al. [26] which was a 3D reconstructed FE model based on medical CT scans. Fig. 4.3 illustrates the finite element modeling of 6th human rib based on the experimental configurations, using the FE software Hypermesh (Altair Hyperworks). The rib model was meshed with hex-shell elements. Specifically, the trabecular bone was meshed with hexahedral solid elements and the cortical bone with quadrilateral shell elements, which has been proved to be applicable and more computationally efficient than all-hex elements [29,127]. A constant cortical thickness was assigned to the shell elements in this study. The element size of the rib model is around 0.7mm in order to obtain adequate rib structural responses. Therefore, the meshed rib model consisted of 13584 solid elements and 4368 shell elements.

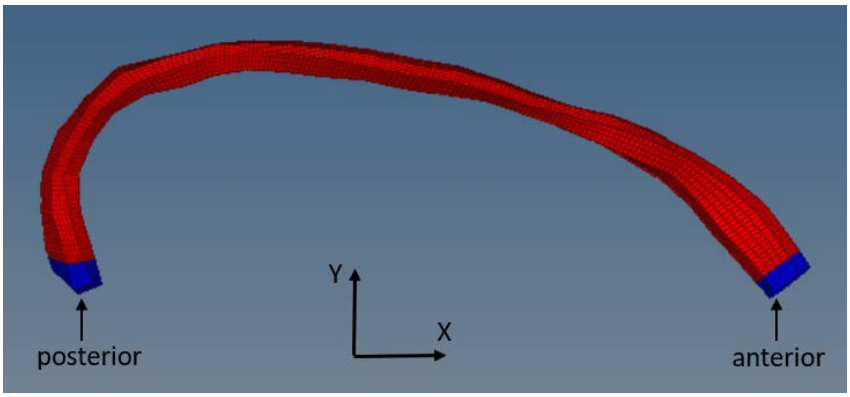

Figure 4.3: Finite element modeling of 6th human rib based on experimental configurations.

4.2.2.2 Boundary Conditions

Subsequently, consistent boundary conditions were defined in the FE model to replicate the experimental setup. As displayed in Fig. 4.3, the two extremities of the rib were modeled as rigid bodies. The sternal (anterior) extremity was allowed to rotate around z axis and to be pushed towards the vertebral (posterior) extremity along x direction, the remaining degrees of freedom were fully constrained. The vertebral (posterior) extremity had only one degree of freedom i.e. rotation around z axis. The reaction force was output at the posterior extremity, and rotations were recorded at both extremities. The strain signals were measured by outputting corresponding strains of cortical shell elements, which were approximately at the same locations in the experiments as described in Section 4.2.1. In addition, for another experimental scenario with initial

offset presented in Fig. 4.2, an offset y_0 between anterior and posterior end was defined in the FE model according to the experimental settings [29,78].

4.2.2.3 Material Properties

Finally, material properties were defined. An elasto-plastic material law was applied for both cortical and trabecular bones. The material model Law 2 (Johnson-Cook material) in RADIOSS was assigned to cortical bone, and the trabecular bone was modeled with Law 3 (Johnson-Cook material compatible with solid elements). Moreover, isotropic hardening was considered for cortical bone and kinematic hardening for trabecular bone. Rib fractures were represented through element deletions based on a built-in failure criterion, by defining maximum plastic strains for cortical and trabecular bones. The human rib cortical bone compressive and tensile material properties at two different strain rates were taken from the literature as shown in Table 4.1, in addition, Poisson's ratio $\nu = 0.3$ and density $\rho = 1990\,kg/m^3$. The material properties of human rib trabecular bone were taken from the literature [127] and remain the same for all the simulations: Young's modulus $E = 0.04GPa$, yield stress $\sigma_y = 2.2MPa$, tangent modulus $E_t = 1MPa$, Poisson's ratio $\nu = 0.45$, density $\rho = 1g/cm^3$ and fracture plastic strain is equal to 0.03. Moreover, the material parameters of porcine rib cortical and trabecular bones were taken from the literature [31] and were displayed in Table 4.2. The two extremities of the rib were modeled as rigid bodies, so a linear elastic material was chosen (Law 1 in RADIOSS) with Young's modulus $E = 210GPa$, Poisson's ratio $\nu = 0.3$ and density $\rho = 7800kg/m^3$.

Table 4.1: Human rib cortical bone compressive and tensile material properties at two strain rates, extracted from [91,92].

Material Properties	0.005 strain/s		0.5 strain/s	
	Compression	Tension	Compression	Tension
Young's modulus (GPa)	11.5	14.63	12.5	15.45
Yield Stress (MPa)	135	68.9	159	85.7
Ultimate Stress (MPa)	154	104.1	189	135.1
Ultimate Strain	0.0204	0.0247	0.0239	0.0292

Table 4.2: The material parameters of porcine rib cortical and trabecular bones, extracted from [31].

Parameter	Cortical	Trabecular
Density (kg/m^3)	1690.9	772.9
Young's modulus (MPa)	9374	1800
Tangent modulus (MPa)	937	45
Yield stress (MPa)	70.876	20.48
Poisson's ratio	0.3	0.45
Fracture plastic strain	0.02	0.03

Table 4.3: Human rib cortical bone compressive material properties at 0.5 strain/s at average age and the decades of 40-49 and 90-99 respectively, extracted from [92].

Material Properties	Average age	40-49 decade	90-99 decade
Young's modulus (GPa)	12.5	14.4	10.7
Yield Stress (MPa)	159	178	129
Ultimate Stress (MPa)	189	214	153
Ultimate Strain	0.0239	0.0233	0.0228

4.2.3 Validation Tests

Validation tests of ribs under dynamic anterior-posterior bending were conducted based on finite element simulations in an explicit nonlinear FE software RADIOSS (Altair Hyperworks) through replicating experimental configurations. Firstly, the 6th level rib model was simulated with the prescribed input displacement recorded by the linear string potentiometer in experimental tests (Fig. 4.1). The average cortical thickness value of rib 6 used here was 0.71mm which was measured by Holcombe et al. [143]. Then, the anterior extremity of rib was pushed at a constant velocity of 1m/s consistent with experiments (Fig. 4.2). The average cortical thickness of rib level 2-10 was 0.67mm according to Li et al. [144]. Numerical force-displacement relationship, cortical strain, rotation and fracture locations were compared with experimental data. Comparison of rib structural responses with human rib cortical bone material properties from different loading modes (tension and compression), different strain rates (0.5 strain/s and 0.005 strain/s), ages and porcine rib material properties was investigated. In addition, the effect of age on rib structural responses was investigated by applying human rib cortical bone compressive material properties at 0.5 strain/s at average age and the decades of 40-49 and 90-99 respectively. Corresponding human cortical bone material properties of different ages are displayed in Table 4.3 and human trabecular bone material properties remain the same. Detailed results and discussions are presented in the following sections.

4.3 Results

This section presents the numerical structural responses of ribs under dynamic anterior-posterior bending for validation and comparison of the developed FE rib models, by comparison with the experimental data of the literature. Two scenarios without (Fig. 4.1) and with (Fig. 4.2) offset were displayed respectively.

Firstly, the 6th rib was simulated as loaded in Fig. 4.1, numerical results were compared to the experiment data of literature [32,133]. Fig. 4.4 (a)-(d) presents the comparison of experimental and numerical strain gauge signals time history with various material properties, which includes human rib cortical material properties from different loading modes (tension and compression), two strain rates (0.5 strain/s and 0.005 strain/s) and porcine rib material properties. Also, numerical and experimental rotations of the two ends of the rib are displayed in Fig. 4.5. Then, numerical force time history with various material properties were compared to five experimental curves as shown in Fig. 4.6. Moreover, Fig. 4.7 (a)-(c) compares the experimental fracture location with numerical fracture locations with human rib and porcine rib material properties respectively. Finally, Fig. 4.8 shows the effect of ages on numerical force time history with human rib cortical bone compressive material properties at 0.5 strain/s at average age and the decades of 40-49 and 90-99, respectively.

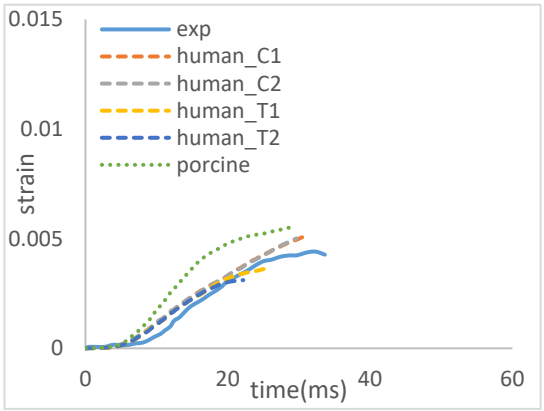

(a) Cutaneous strain gauge 1 (CSG1)

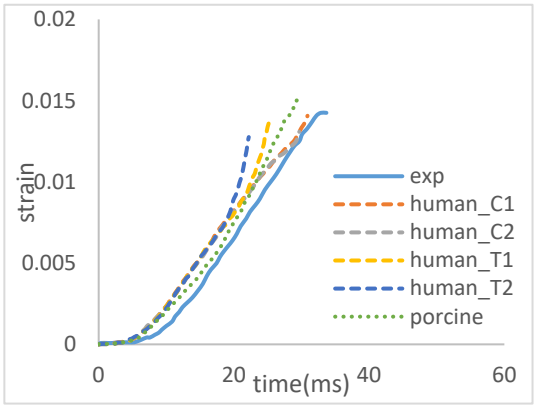

(b) Cutaneous strain gauge 2 (CSG2)

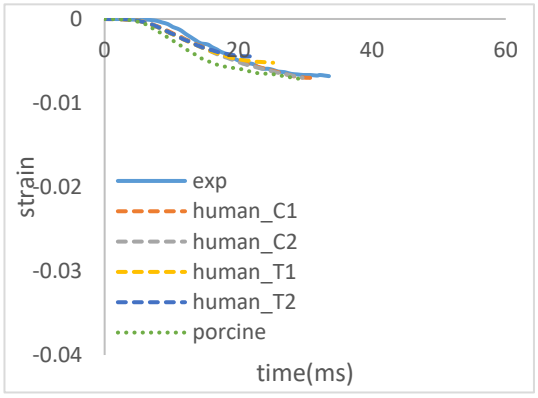

(c) Pleural strain gauge 1 (PSG1)

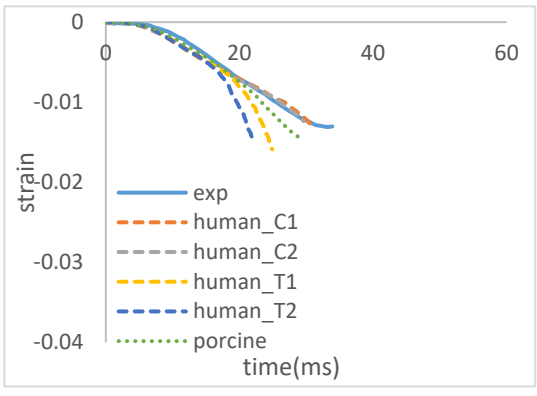

(d) Pleural strain gauge 2 (PSG2)

Figure 4.4: Comparison of experimental and numerical strain gauge signals versus time

with various material properties, where labels ‘human_C1’, ‘human_C2’, ‘human_T1’ and ‘human_T2’ represent human rib cortical bone compressive material properties at 0.5 strain/s and 0.005 strain/s and human rib cortical bone tensile material properties at 0.5 strain/s and 0.005 strain/s, respectively.

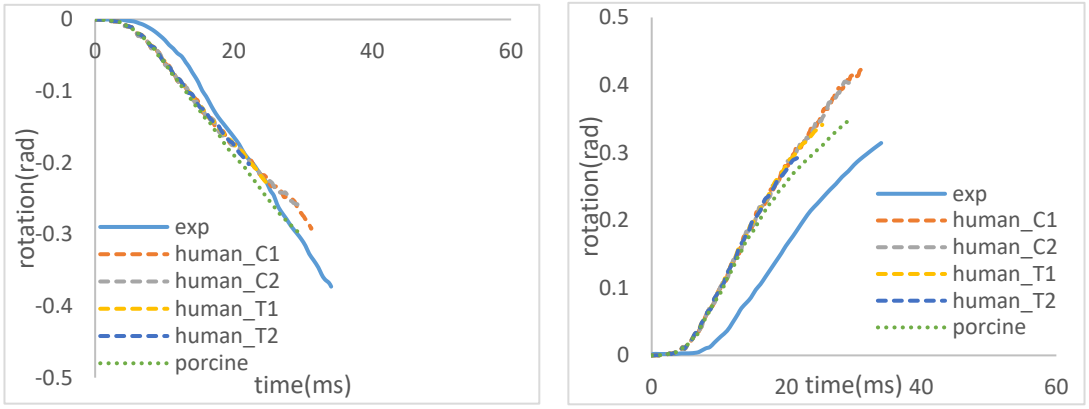

(a) Rotation of sternal (anterior) end (b) Rotation of vertebral (posterior) end

Figure 4.5: Experimental and numerical rotation time history of sternal (anterior) and vertebral (posterior) ends with various rib material properties, where labels ‘human_C1’, ‘human_C2’, ‘human_T1’ and ‘human_T2’ correspond to human rib cortical bone compressive material properties at 0.5 strain/s and 0.005 strain/s and human rib cortical bone tensile material properties at 0.5 strain/s and 0.005 strain/s, respectively.

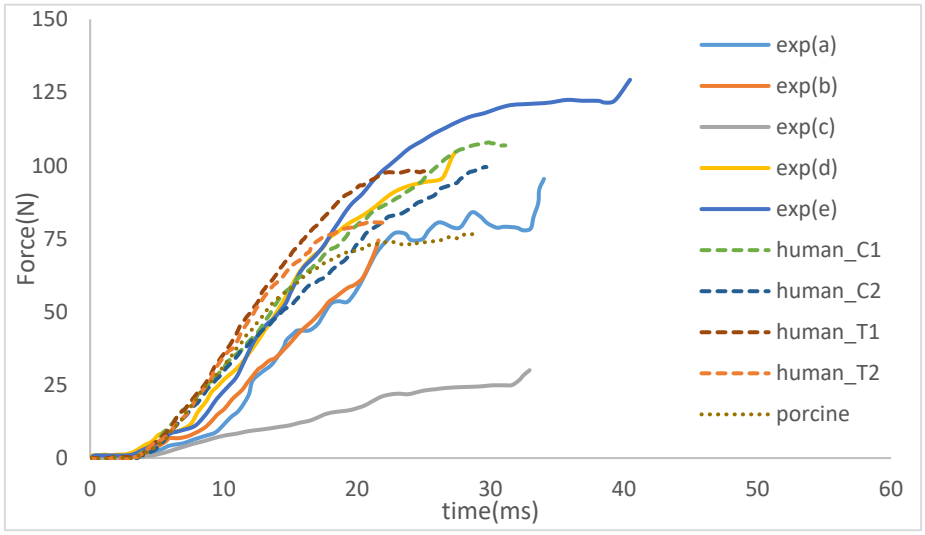

Figure 4.6: Representation of experimental and numerical force time history with various material properties, where labels ‘exp(a)-exp(e)’ represent 5 experimental curves in [32], ‘human_C1’, ‘human_C2’, ‘human_T1’ and ‘human_T2’ represent human rib cortical bone compressive material properties at 0.5 strain/s and 0.005 strain/s and human rib cortical bone tensile material properties at 0.5 strain/s and 0.005 strain/s, respectively.

(a)

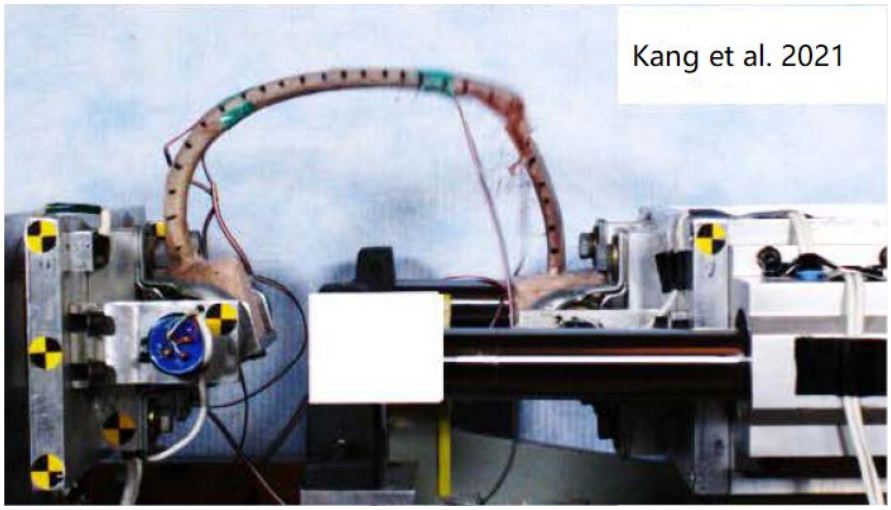

(b)

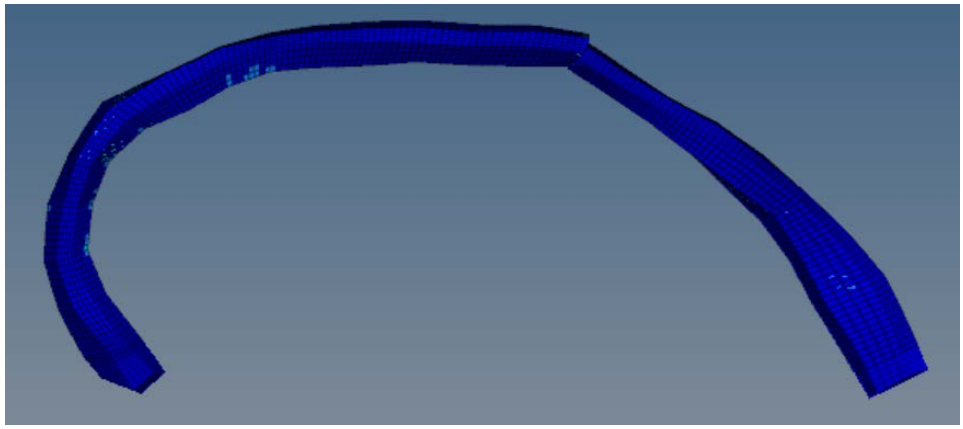

(c)

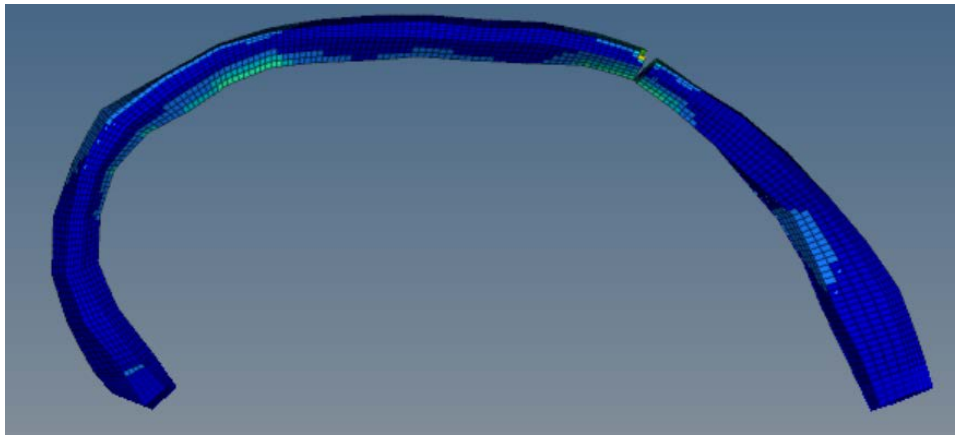

Figure 4.7: Illustration of experimental (a) and numerical fracture locations with human rib (b) and porcine rib (c) material properties.

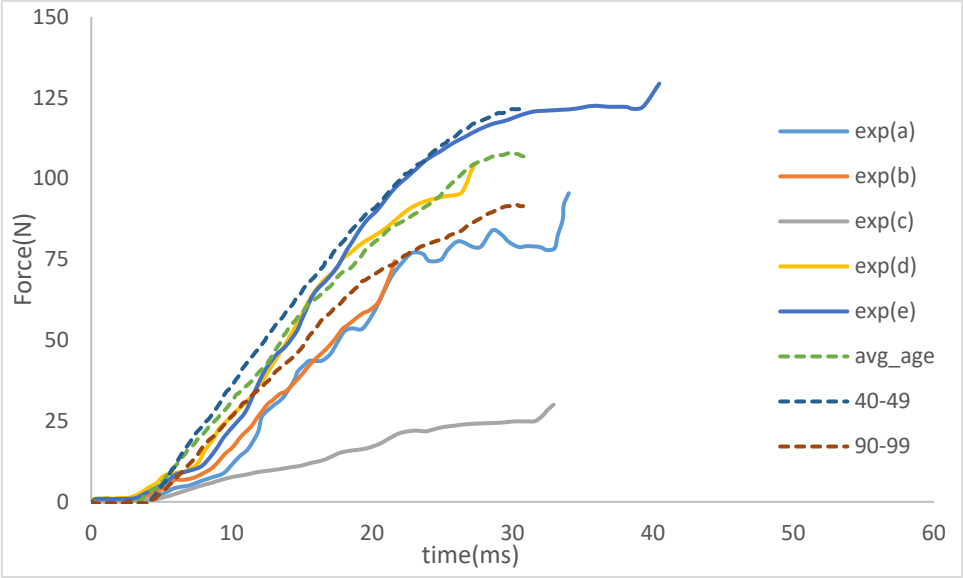

Figure 4.8: Representation of the effect of ages on numerical force time history with human rib cortical bone compressive material properties at 0.5 strain/s.

Then, rib level 2 to 10 with initial offsets were simulated as loaded in Fig. 4.2 as well. Numerical results were compared to the published experimental data by Li et al. [144]. Numerical reaction force versus end-to-end displacement curves of rib level 2-10 were compared to experimental corridors as shown in Fig. 4.9, where various material properties were applied and compared including human rib cortical material properties from different loading modes (tension and compression), different strain rates (0.5 strain/s and 0.005 strain/s) and porcine rib material properties.

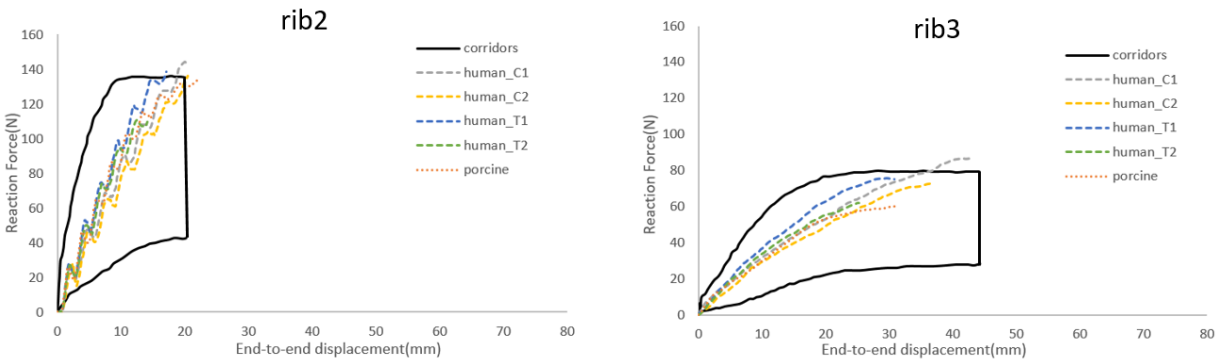

(continued)

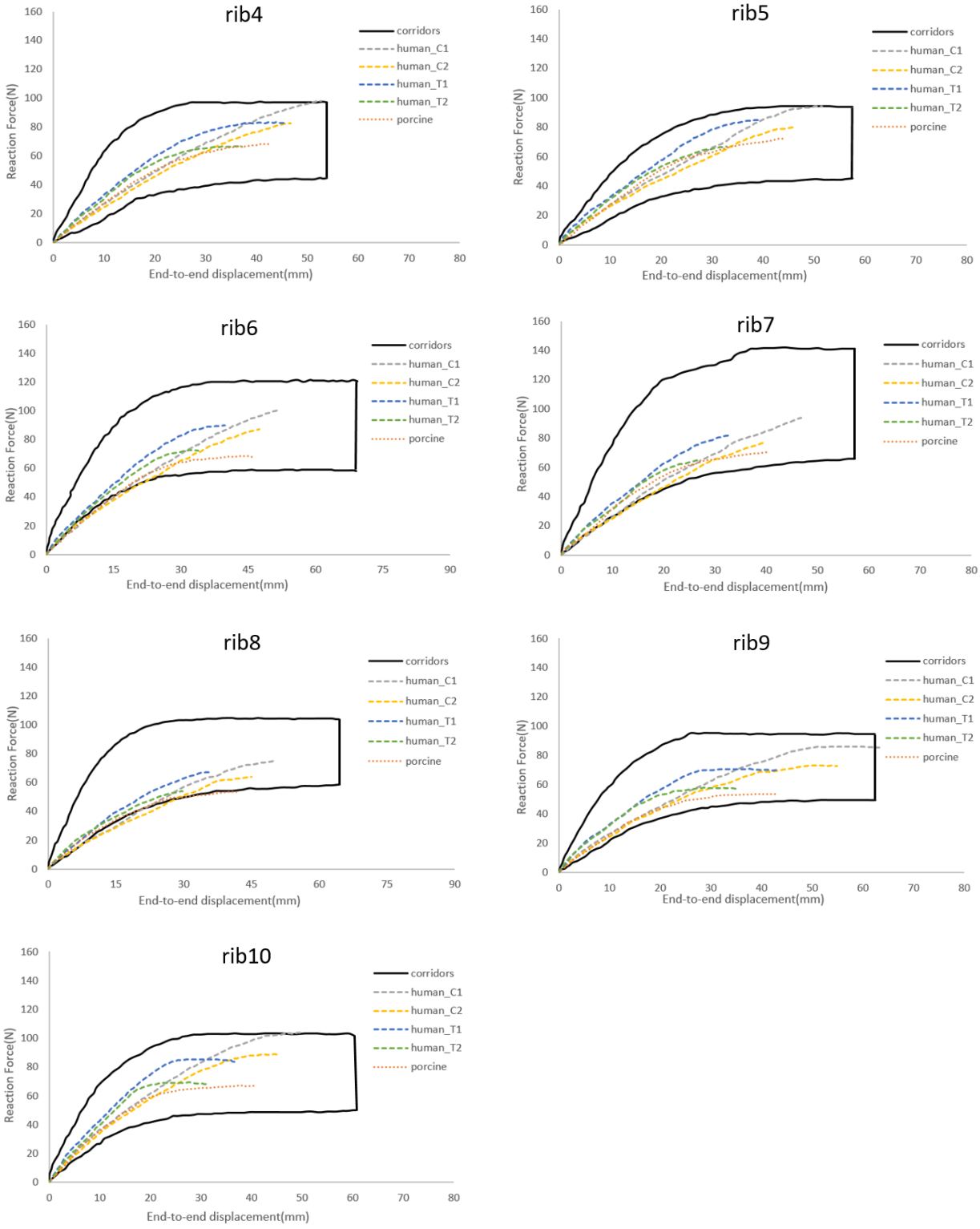

Figure 4.9: Illustration of numerical reaction force versus end-to-end displacement of rib level 2-10 compared to experimental corridors of the literature, where labels 'human_C1', 'human_C2', 'human_T1' and 'human_T2' represent human rib cortical bone compressive material properties at 0.5 strain/s and 0.005 strain/s and human rib cortical bone tensile material properties at 0.5 strain/s and 0.005 strain/s, respectively.

4.4 Discussion

Human rib finite element models were created and simulated by replicating experimental configurations of ribs under dynamic anterior-posterior bending in this study. Numerical rib structural responses and fracture locations were compared with the experimental data of the literature, in order to validate the feasibility and robustness of the developed rib models. Comparison and analysis of the effect of human rib cortical bone material properties from different loading modes (tension and compression), strain rates, ages and porcine rib material properties on rib structural responses were investigated. Two scenarios without (Fig. 4.1) and with (Fig. 4.2) offset were investigated respectively.

Firstly, the 6th level rib model was simulated with the prescribed input displacement in experimental tests (Fig. 4.1). Fig. 4.4 (a)-(d) and Fig. 4.5 (a)-(b) present the comparison of experimental and numerical strain gauge signals and rib end rotations time history with various material properties, including human rib cortical material properties from different loading modes (tension and compression), different strain rates (0.5 strain/s and 0.005 strain/s) and porcine rib material properties. It can be seen that the numerical strain signals as well as rib end rotations have the same rising tendencies as those in experiments despite some slight discrepancies. Numerical fracture time is slightly inferior to experimental fracture time, which indicates that FE rib models are relatively less stiff. It is worth noting that numerical strain and rotation time histories with human rib cortical compressive material properties fracture later and have a better correlation with experimental data compared to those with human rib cortical tensile material properties. It demonstrates that the incorporation of rib cortical bone compressive material properties in FE models of this study is necessary. In fact, the rib suffers both tensile and compressive loading modes during MVCs. Meanwhile, it can also be seen that for both loading modes (tension and compression), numerical results with material properties at 0.5 strain/s have relatively longer fracture time and larger strain and rotation values than those at 0.005 strain/s. Also, numerical results with human cortical bone tensile material properties at 0.5 strain/s fit better with experimental curves compared to those at 0.005 strain/s. Therefore, it confirms the need to consider strain rate sensitivity in FE models when investigating rib dynamic structural responses. Furthermore, it is noted that numerical strain and rotation time histories with porcine rib material properties also have a reasonable correlation with experimental curves. This indicates that porcine ribs can be used as human rib substitutes and can compensate the limit of the use of human cadavers. Actually, porcine ribs were used by researchers as human rib substitutes because they have similar geometrical and anatomical characteristics with human ribs [31,79,81–83].

Next, numerical force versus time curves with various material properties were compared to five experimental curves as depicted in Fig. 4.6. It can be noticed that the

numerical force-time curves have all good correlations with experimental curves. At the same time, numerical reaction forces with human rib cortical compressive material properties are larger than those with human rib cortical tensile material properties while the slope of the curves are relatively smaller. This could be explained by the differences between human rib cortical bone compressive and tensile material properties as displayed in Table 4.1, where compressive material properties have higher ultimate stresses and smaller Young's modulus. Also, numerical forces increase with the increase of strain rate from 0.005 strain/s to 0.5 strain/s for both compressive and tensile material properties. Comparison of numerical forces above in Fig. 4.6 highlights the effect of different material properties in compression and tension as well as different strain rates so that they should be considered in rib FE models. Besides, despite the numerical force with porcine material properties is smaller than forces with human rib material properties, it is still within the experimental values. Then, Fig. 4.7 (a)-(c) illustrates the comparison of experimental and numerical rib fracture locations. It is revealed that both numerical fracture locations with human rib (Fig. 4.7(b)) and porcine rib (Fig. 4.7(c)) material properties correspond well with the experimental location that occurs at the anterolateral region of the rib, which may signify the biofidelity of the finite element rib model.

In addition, Fig. 4.8 compares the effect of age on numerical force-time history with human rib cortical bone compressive material properties at 0.5 strain/s at average age, 40-49 decade and 90-99 decade. The 40-49 decade has the largest force magnitude and fastest rising tendency because this age group has higher ultimate stress and Young's modulus as presented in Table 4.3 while the 90-99 decade has smallest values. Actually, collagen degradation may result in the alteration of the material properties in aged bones [92]. The differences between different ages suggest the consideration of age variations when establishing rib FE models.

Finally, the anterior extremity was pushed at a constant velocity of 1m/s consistent with experimental setup (Fig. 4.2) for ribs from level 2 to 10. Numerical reaction force versus end-to-end displacement curves of rib level 2 to 10 with various aforementioned material properties were compared to experimental corridors presented by Li et al. [144], as illustrated in Fig. 4.9. It is noted that most of the numerical force-displacement curves with human cortical bone compressive and tensile as well as porcine rib material properties are always within the experimental corridors, only rib 2 and rib 3 at final displacement period and rib 6 and rib 8 at initial displacement period have very slight deviations. This also demonstrates the biofidelity of the FE rib models developed in this study. Moreover, the differences and tendencies between force-displacement curves with human rib cortical bone material properties from different loading modes (tension and compression), different strain rates (0.5 strain/s and 0.005 strain/s) and porcine rib material properties are similar to force-time curves in Fig. 4.6.

Overall, numerical rib structural responses and fracture locations have a good correlation with experimental data of the literature. Thus, the biofidelity and robustness of the finite element rib models have been validated via numerical analysis. However, it can be noticed some limitations in this study which may explain the discrepancies of the results. An average constant cortical thickness was used for the rib models in the present study and actually the cortical thickness varies throughout the rib, so it may overestimate or underestimate the cortical thickness somewhere and lead to inaccuracies of local strains. Therefore, precise and variable cortical thicknesses which can represent real cortical thickness distributions should be implemented in a more biofidelic numerical model. Also, although this is the first numerical study to apply human rib cortical bone compressive material properties in investigating rib dynamic structural responses, the material laws used for the ribs in this study are isotropic and homogenous, therefore anisotropic and heterogeneous material models need to be incorporated in the future. Besides, considering that the rib experiences both tensile and compressive loading modes during MVCs, one single material law combining both tensile and compressive behavior could improve the results. Moreover, human rib cortical bone material properties at two strain rates (0.5 strain/s and 0.005 strain/s) were used according to experimental data, material properties at higher strain rates should be taken into account and could better evaluate the strain rate effect on human rib cortical bone material properties.

4.5 Conclusion

Human rib finite element models were created and validated by replicating experimental configurations of ribs under dynamic anterior-posterior bending, using an explicit FE software RADIOSS (Altair Hyperworks). Different material properties including human rib cortical bone material properties from different loading modes (tension and compression), different strain rates and ages as well as porcine rib material properties were considered. A reasonable agreement exists between numerical rib structural responses and fracture locations and experimental data of the literature. Numerical analysis reveals that numerical strain and rotation time histories with human rib cortical compressive material properties have a better correlation with experimental data compared to those with human rib cortical tensile material properties. Numerical rib structural responses were found to be sensitive to material properties from different loading modes, strain rates and ages. Therefore, it is necessary to consider the effect of material properties from different loading modes, strain rates and ages when establishing rib FE models. Meanwhile, it is also indicated that porcine rib material properties can obtain similar and reasonable results compared to human rib material properties. Overall, this was the first numerical study to apply human rib cortical bone compressive material properties in investigating rib dynamic structural responses. The biofidelity and robustness of the finite element rib models have been validated, and these rib models can be further employed in a global thorax model for injury predictions.

The present study can help better understand human rib fractures in high velocity impact (HVI) contexts in a numerical way.

5 Conclusions and Perspectives

5.1 Conclusions

The thorax part is one of the most injured body areas under high velocity impacts, just second behind the head part. Thoracic injuries happen frequently in various frameworks of high velocity impact biomechanics such as road traffic accidents, sports and military contexts. Rib fractures and lung injuries are the most common hard and soft tissue injuries in human thorax and can be life-threatening. In recent years, many biomechanical FE models have been established and employed to repeat real-world impact loading conditions to investigate human tissue dynamic behaviors which can avoid practical issues in biomechanical experiments. Therefore, this thesis aims to contribute to the investigation of dynamic responses of human tissues especially ribs and soft tissues under high velocity impacts using finite element modeling, which can help better understand the mechanisms of corresponding injuries and is useful for design, evaluate and optimizing protecting equipment.

Firstly, a novel strain-rate-dependent elasto-hydrodynamic constitutive law of the SEBS gel was proposed in Chapter 2 based on the mechanical characterization extracted from the literature. The proposed law was then implemented as a user material subroutine programed in Fortran in an explicit nonlinear FE software Radioss (Altair Hyperworks) to reproduce various loading configurations in order to validate the accuracy of the model, and the effect of strain rate was investigated. A good agreement exists between the numerical results of the proposed law and experimental data in the literature. Numerical analysis reveals that the strain-rate-dependence effect is significant in SEBS gel especially for high strain rates, which indicates the necessity of taking the strain rate dependence into consideration when modeling the SEBS gel as a human soft tissue substitute.

Then, this thesis numerically investigated the dynamic behaviors of isolated porcine ribs submitted to high velocity impacts using 3PB SHPB apparatus based on finite element simulations in Chapter 3, both porcine and human rib material properties were applied for comparison. The numerical curved beam rib models are validated and show biofidelic behaviors by comparing numerical and experimental results. In addition, sensitivity studies were conducted to study the effects of geometrical and mechanical parameters such as cortical thickness, curvature radius and strain rate on dynamic responses of ribs under high velocity impacts. Numerical analysis highlights the significant effect of geometrical parameters on dynamic behaviors of ribs. The consideration of the effect of mechanical parameters like loading mode and strain rate

sensitivity in FE rib models is also needed. Porcine ribs are usually used as human rib surrogates because they share similar geometrical and anatomical characteristics. Hence, this work is an interesting way to study the human rib dynamic behaviors at a numerical level, and these ribs models can be further implemented in a more global thoracic biomechanical model for human trauma investigations.

Finally, in Chapter 4 rib FE models with various material properties including human rib cortical bone material properties from different loading modes (tension and compression), strain rates (0.5 strain/s and 0.005 strain/s) and ages as well as porcine rib material properties were developed and validated through replicating experimental configurations, in order to better understand rib structural responses and fracture locations under dynamic anterior-posterior bending. Numerical force-displacement relationship, cortical strain, rotation and fracture locations correspond well with published experimental data, which demonstrates the robustness of the finite element rib models. Numerical analysis reveals that numerical strain and rotation time histories with human rib cortical compressive material properties have a better correlation with experimental data compared to those with human rib cortical tensile material properties. Also, numerical rib structural responses are found to be sensitive to human cortical bone material properties from different loading modes, strain rates and ages. Therefore, it is necessary to consider the effect of material properties from different loading modes, strain rates and ages when establishing rib FE models. Meanwhile, it is also revealed that porcine rib material properties can obtain similar and reasonable results compared to human rib material properties. This is the first numerical study to apply human rib compressive material properties in investigating rib dynamic structural responses under dynamic anterior-posterior bending and compare the results with those from tensile material properties. The present study can help better understand human rib fractures in high velocity impact (HVI) contexts in a numerical way.

Overall, this thesis investigates the dynamic responses of human soft and hard tissues under high velocity impacts using finite element modeling. The proposed constitutive law of the SEBS gel and the rib FE models can be employed in a global thorax model for injury predictions.

5.2 Limits and Perspectives

There are some limitations in the present studies although the proposed constitutive law and rib models have been validated to be feasible and biofidelic. For example, the proposed strain rate dependent constitutive law of the SEBS gel elaborated from stress-strain curves is based on mechanical characterization at intermediate strain rates, so it can be improved by considering stress-strain curves at higher strain rates. The strain rate dependence can also be considered in the plasticity domain in further investigations. Also, a constant cortical thickness is used in this thesis and actually the cortical

thickness varies variable throughout the rib, so it may overestimate or underestimate the cortical thickness somewhere and lead to inaccuracies of numerical results. Therefore, precise and variable cortical thicknesses which can represent real cortical thickness distributions should be implemented in a more biofidelic numerical model. Moreover, the material laws used for the ribs in this thesis are isotropic and homogenous, therefore anisotropic and heterogeneous material models need to be incorporated in the future studies. Besides, the material laws are based on single tensile or compressive tests, considering that the rib experiences both tensile and compressive loading modes during MVCs, one single material law combining both tensile and compressive behaviors needed to be developed and could improve the results. In addition, a built-in failure criterion in the material model based on the maximum fracture plastic strain is used to represent rib fracture, additional failure models could be added to the material model in order to better simulate rib fractures.

The developed constitutive law of the SEBS gel and rib models can be further implemented in a more global thoracic biomechanical model for human trauma investigations. They are also planned to be applied at higher strain rates, such as in blast contexts.

Bibliography

[1] Cavanaugh JM, Zhu Y, Huang Y, King AI. Injury and response of the thorax in side impact cadaveric tests. SAE Tech. Pap., 1993. https://doi.org/10.4271/933127.

[2] Ruan J, El-Jawahri R, Chai L, Barbat S, Prasad P. Prediction and Analysis of Human Thoracic Impact Responses and Injuries in Cadaver Impacts Using a Full Human Body Finite Element Model. Stapp Car Crash J., 2003, p. 47:299-321. https://doi.org/10.4271/2003-22-0014.

[3] Payne T, Mitchell S, Bibb R, Waters M. The evaluation of new multi-material human soft tissue simulants for sports impact surrogates. J Mech Behav Biomed Mater 2015;41:336–56. https://doi.org/10.1016/j.jmbbm.2014.09.018.

[4] Forman J, Poplin GS, Shaw CG, McMurry TL, Schmidt K, Ash J, et al. Automobile injury trends in the contemporary fleet: Belted occupants in frontal collisions. Traffic Inj Prev 2019;0:1–6. https://doi.org/10.1080/15389588.2019.1630825.

[5] Richard Cuerden, Rebecca Cookson PM and ME. A review of the european 40% offset frontal impact test configuration. Proc 20th Int Tech Conf Enhanc Saf Veh 2007.

[6] Yamamoto L, Schroeder C, Morley D, Beliveau C. Thoracic trauma: The deadly dozen. Crit Care Nurs Q 2005. https://doi.org/10.1097/00002727-200501000-00004.

[7] Kent R, Patrie J. Chest deflection tolerance to blunt anterior loading is sensitive to age but not load distribution. Forensic Sci Int 2005. https://doi.org/10.1016/j.forsciint.2004.04.086.

[8] Kent R, Woods W, Bostrom O. Fatality risk and the presence of rib fractures. Ann Adv Automot Med - 52nd Annu Sci Conf 2008;52:73–82.

[9] Morris A, Welsh R, Frampton R, Charlton J, Fildes B. An overview of requirements for the crash protection of older drivers. Annu Proc Assoc Adv Automot Med 2002.

[10] Kent R, Lee SH, Darvish K, Wang S, Poster CS, Lange AW, et al. Structural and Material Changes in the Aging Thorax and Their Role in Crash Protection for Older Occupants. SAE Tech Pap 2005;2005-Novem:1–19. https://doi.org/10.4271/2005-22-0011.

[11] Bir C, Viano D, King A. Development of biomechanical response corridors of the thorax to blunt ballistic impacts. J Biomech 2004;37:73–9. https://doi.org/10.1016/S0021-9290(03)00238-0.

[12] Prat N, Rongieras F, de Freminville H, Magnan P, Debord E, Fusai T, et al. Comparison of thoracic wall behavior in large animals and human cadavers submitted to an identical ballistic blunt thoracic trauma. Forensic Sci Int 2012;222:179–85. https://doi.org/10.1016/j.forsciint.2012.05.022.

[13] Humphrey C, Kumaratilake J. Ballistics and anatomical modelling – A review.

Leg Med 2016;23:21–9. https://doi.org/10.1016/j.legalmed.2016.09.002.
[14] Albert DL, Beeman SM, Kemper AR. Occupant kinematics of the Hybrid III, THOR-M, and postmortem human surrogates under various restraint conditions in full-scale frontal sled tests. Traffic Inj Prev 2018;19:S50–8. https://doi.org/10.1080/15389588.2017.1405390.
[15] Yang KH, Hu J, White NA, King AI, Chou CC, Prasad P. Development of Numerical Models for Injury Biomechanics Research: A Review of 50 Years of Publications in the Stapp Car Crash Conference. Stapp Car Crash J 2006;50:429–90. https://doi.org/10.4271/2006-22-0017.
[16] Iwamoto M, Kisanuki Y, Watanabe I, Furusu K, Miki K. Development of a finite element model of the total human model for safety (THUMS). IRCOBI Conf 2002.
[17] Robin S. Humos: Human Model for Safety–a joint effort towards the development of refined human like car occupant models. Stapp Car Crash Conf 2001.
[18] Gayzik FS, Moreno DP, Vavalle NA, Rhyne AC, Stitzel JD. Development of a Full Human Body Finite Element Model for Blunt Injury Prediction Utilizing a Multi-Modality Medical Imaging Protocol. 12th Int LS-DYNA Users Conf 2012.
[19] Forbes PA, Cronin DS, Deng YC. Multi-scale human body model to predict side impact thoracic trauma. Int J Crashworthiness 2006;11:203–16. https://doi.org/10.1533/ijcr.2005.0391.
[20] Roberts SB, Chen PH. Elastostatic analysis of the human thoracic skeleton. J Biomech 1970;3:527–45. https://doi.org/https://doi.org/10.1016/0021-9290(70)90037-0.
[21] Sundaram SH, Feng CC. Finite element analysis of the human thorax. J Biomech 1977;10:505–16. https://doi.org/https://doi.org/10.1016/0021-9290(77)90104-X.
[22] Huang Y, King AI, Cavanaugh JM. Finite Element Modeling of Gross Motion of Human Cadavers in Side Impact. SAE Trans 1994;103:1604–22.
[23] Plank G, Eppinger R. An Improved Finite Element Model of the Human Thorax. Proc. 13th Int. Tech. Conf. Exp. Saf. Veh., 1991.
[24] Lizée E, Robin S, Song E, Bertholon N, Coz JL, Besnault B, et al. Development of a 3D finite element model of the human body. Proc 42nd Stapp Car Crash Conf 1998.
[25] Kimpara H, Lee JB, Yang KH, King AI, Iwamoto M, Watanabe I, et al. Development of a Three-Dimensional Finite Element Chest Model for the 5th Percentile Female. Proc. 49th Stapp Car Crash Conf., 2005. https://doi.org/10.4271/2005-22-0012.
[26] Roth S, Torres F, Feuerstein P, Thoral-Pierre K. Anthropometric dependence of the response of a Thorax FE model under high speed loading: Validation and real world accident replication. Comput Methods Programs Biomed 2013;110:160–70. https://doi.org/10.1016/j.cmpb.2012.11.004.
[27] Charpail E, Trosseille X, Petit P, Laporte S, Lavaste F, Vallancien G.

Characterization of PMHS Ribs: A New Test Methodology. SAE Tech. Pap., 2005. https://doi.org/10.4271/2005-22-0009.
[28] Li Z, Kindig MW, Kerrigan JR, Untaroiu CD, Subit D, Crandall JR, et al. Rib fractures under anterior-posterior dynamic loads: Experimental and finite-element study. J Biomech 2010;43:228–34. https://doi.org/10.1016/j.jbiomech.2009.08.040.
[29] Li Z, Kindig MW, Subit D, Kent RW. Influence of mesh density, cortical thickness and material properties on human rib fracture prediction. Med Eng Phys 2010;32:998–1008. https://doi.org/10.1016/j.medengphy.2010.06.015.
[30] Iraeus J, Lundin L, Storm S, Agnew A, Kang YS, Kemper A, et al. Detailed subject-specific FE rib modeling for fracture prediction. Traffic Inj Prev 2019;20:S88–95. https://doi.org/10.1080/15389588.2019.1665649.
[31] Ayagara AR, Langlet A, Hambli R. On dynamic behavior of bone: Experimental and numerical study of porcine ribs subjected to impact loads in dynamic three-point bending tests. J Mech Behav Biomed Mater 2019;98:336–47. https://doi.org/10.1016/j.jmbbm.2019.05.031.
[32] Yates KM, Agnew AM, Albert DL, Kemper AR, Untaroiu CD. Subject-specific rib finite element models with material data derived from coupon tests under bending loading. J Mech Behav Biomed Mater 2021;116:104358. https://doi.org/10.1016/j.jmbbm.2021.104358.
[33] Chaurasiya BD. Human Anatomy: Upper Limb, Thorax. CBS Publ Distrib 2013;1.
[34] Gray H, Lewis WH. Anatomy of the Human Body. Lea \& Febiger; 1918.
[35] Schünke M, Schulte E, Ross LM, Schumacher U, Lamperti ED, Rude J, et al. Thieme Atlas of Anatomy: Neck and Internal Organs. Thieme; 2006.
[36] Standring S. Gray's Anatomy: The Anatomical Basis of Clinical Practice. Elsevier Health Sciences; 2015.
[37] Jussila J, Leppäniemi A, Paronen M, Kulomäki E. Ballistic skin simulant. Forensic Sci Int 2005;150:63–71. https://doi.org/10.1016/j.forsciint.2004.06.039.
[38] Moy P, Gunnarsson CA, Weerasooriya T. Tensile deformation and fracture of ballistic gelatin as a function of loading rate. Soc Exp Mech - SEM Annu Conf Expo Exp Appl Mech 2009 2009;2:848–55.
[39] Sparks JL, Vavalle NA, Kasting KE, Long B, Tanaka ML, Sanger PA, et al. Use of silicone materials to simulate tissue biomechanics as related to deep tissue injury. Adv Ski Wound Care 2015;28:59–68. https://doi.org/10.1097/01.ASW.0000460127.47415.6e.
[40] Taddei L, Awoukeng Goumtcha A, Roth S. Smoothed particle hydrodynamics formulation for penetrating impacts on ballistic gelatine. Mech Res Commun 2015;70:94–101. https://doi.org/10.1016/j.mechrescom.2015.09.010.
[41] Luo S, Xu C, Chen A, Zhang X. Experimental investigation of the response of gelatine behind the soft body armor. Forensic Sci Int 2016;266:8–13. https://doi.org/10.1016/j.forsciint.2016.04.019.
[42] Fontenier B, Hault-Dubrulle A, Drazetic P, Fontaine C, Naceur H. On the

mechanical characterization and modeling of polymer gel brain substitute under dynamic rotational loading. J Mech Behav Biomed Mater 2016;63:44–55. https://doi.org/10.1016/j.jmbbm.2016.06.008.
[43] Sauer C, Heine A, Bagusat F, Riedel W. Ballistic impact on fired clay masonry bricks. Int J Prot Struct 2019. https://doi.org/10.1177/2041419619893708.
[44] Shergold OA, Fleck NA. Experimental investigation into the deep penetration of soft solids by sharp and blunt punches, with application to the piercing of skin. J Biomech Eng 2005;127:838–48. https://doi.org/10.1115/1.1992528.
[45] Riedel W, Kawai N, Kondo K ichi. Numerical assessment for impact strength measurements in concrete materials. Int J Impact Eng 2009;36:283–93. https://doi.org/10.1016/j.ijimpeng.2007.12.012.
[46] Maiden N. Historical overview of wound ballistics research. Forensic Sci Med Pathol 2009;5:85–9. https://doi.org/10.1007/s12024-009-9090-z.
[47] Wen Y, Xu C, Wang H, Chen A, Batra RC. Impact of steel spheres on ballistic gelatin at moderate velocities. Int J Impact Eng 2013;62:142–51. https://doi.org/10.1016/j.ijimpeng.2013.07.002.
[48] Liu L, Fan Y, Li W. Viscoelastic shock wave in ballistic gelatin behind soft body armor. J Mech Behav Biomed Mater 2014;34:199–207. https://doi.org/10.1016/j.jmbbm.2014.02.011.
[49] Carr DJ, Stevenson T, Mahoney PF. The use of gelatine in wound ballistics research. Int J Legal Med 2018;132:1659–64. https://doi.org/10.1007/s00414-018-1831-7.
[50] Al Khalil M, Frissane H, Taddei L, Meng S, Lebaal N, Demoly F, et al. SPH-based method to simulate penetrating impact mechanics into ballistic gelatin: Toward an understanding of the perforation of human tissue. Extrem Mech Lett 2019;29:100479. https://doi.org/10.1016/j.eml.2019.100479.
[51] Jussila J. Preparing ballistic gelatine - Review and proposal for a standard method. Forensic Sci Int 2004;141:91–8. https://doi.org/10.1016/j.forsciint.2003.11.036.
[52] Nicholas NC, Welsch JR, LAB. PSUUPAR. Institute for Non-Lethal Defense Technologies Report: Ballistic Gelatin. pennsylvania state univ university park applied research lab; 2004.
[53] Cronin DS, Falzon C. Characterization of 10% Ballistic Gelatin to Evaluate Temperature, Aging and Strain Rate Effects. Exp Mech 2011;51:1197–206. https://doi.org/10.1007/s11340-010-9438-z.
[54] M. L. Fackler JAM. Ordnance gelatin for ballistic studies: Detrimental effect of excess heat used in gelatin preparation. Am J Forensic Med Pathol 1988;93.
[55] Mauzac O, Paquier C, Debord E, Barbillon F, Mabire P, Jacquet JF. A substitute of gelatine for the measurement of the dynamic back face deformacion . Proc Pers Armour Syst Symp 2010:99–108.
[56] Mrozek RA, Leighliter B, Gold CS, Beringer IR, Yu JH, VanLandingham MR, et al. The relationship between mechanical properties and ballistic penetration depth in a viscoelastic gel. J Mech Behav Biomed Mater 2015;44:109–20. https://doi.org/10.1016/j.jmbbm.2015.01.001.

[57] Mauzac O, Paquier C, Barbillon F, Mabire P, Jacquet J, Debord E, et al. Comparative assessment of behind armour blunt trauma (BABT) by means of a novel transparent synthetic gel. Pers Armour Syst Symp 2012.
[58] Bracq A, Haugou G, Delille R, Lauro F, Roth S, Mauzac O. Experimental study of the strain rate dependence of a synthetic gel for ballistic blunt trauma assessment. J Mech Behav Biomed Mater 2017;72:138–47. https://doi.org/10.1016/j.jmbbm.2017.04.027.
[59] Bracq A, Haugou G, Bourel B, Maréchal C, Lauro F, Roth S, et al. On the modeling of a visco-hyperelastic polymer gel under blunt ballistic impacts. Int J Impact Eng 2018;118:78–90. https://doi.org/10.1016/j.ijimpeng.2018.04.001.
[60] Meng S, Shen J, Taddei L, Lebaal N, Veysset D, Nelson KA, et al. Modelling of micro-particles perforations into human tissue surrogate: Numerical and analytical aspects. Extrem Mech Lett 2021;45:101299. https://doi.org/10.1016/j.eml.2021.101299.
[61] Vawter DL. A Finite Element Model for Macroscopic Deformation of the Lung. J Biomech Eng 1980;102:1–7. https://doi.org/10.1115/1.3138193.
[62] Yang LM, Shim VPW, Lim CT. A visco-hyperelastic approach to modelling the constitutive behaviour of rubber. Int J Impact Eng 2000;24:545–60. https://doi.org/10.1016/S0734-743X(99)00044-5.
[63] Salisbury CP, Cronin DS. Mechanical properties of ballistic gelatin at high deformation rates. Exp Mech 2009;49:829–40. https://doi.org/10.1007/s11340-008-9207-4.
[64] Kwon J, Subhash G. Compressive strain rate sensitivity of ballistic gelatin. J Biomech 2010;43:420–5. https://doi.org/10.1016/j.jbiomech.2009.10.008.
[65] Ravikumar N, Noble C, Cramphorn E, Taylor ZA. A constitutive model for ballistic gelatin at surgical strain rates. J Mech Behav Biomed Mater 2015;47:87–94. https://doi.org/10.1016/j.jmbbm.2015.03.011.
[66] Johnson AF, Holzapfel M. Numerical prediction of damage in composite structures from soft body impacts. J Mater Sci 2006;41:6622–30. https://doi.org/10.1007/s10853-006-0201-x.
[67] Appleby-Thomas GJ, Hazell PJ, Sheldon RP, Stennett C, Hameed A, Wilgeroth JM. The high strain-rate behaviour of selected tissue analogues. J Mech Behav Biomed Mater 2014;33:124–35. https://doi.org/10.1016/j.jmbbm.2013.05.018.
[68] Dewar DC, Tarrant SM, King KL, Balogh ZJ. Changes in the epidemiology and prediction of multiple-organ failure after injury. J Trauma Acute Care Surg 2013;74.
[69] Schmitt KU, Niederer PF, Cronin DS, Muser MH, Walz F. Trauma Biomechanics: An Introduction to Injury Biomechanics. Springer Berlin Heidelberg; 2014.
[70] Becher RD, Colonna AL, Enniss TM, Weaver AA, Crane DK, Martin RS, et al. An innovative approach to predict the development of adult respiratory distress syndrome in patients with blunt trauma. J Trauma Acute Care Surg 2012;73.
[71] Moore KL, Agur AMR, Dalley AF. Essential Clinical Anatomy. Lippincott

Williams \& Wilkins; 2007.
[72] Gierczycka D. Investigation of Thorax Response and Potential for Injury in Side Impacts Using Integrated Detailed Human and Vehicle Finite-Element Models. University of Waterloo, 2018.
[73] DePuy P, Young DW, Rowe S. Extensive Pulmonary Laceration in Pediatric Trauma. Respiration 2008;79:76.
[74] Cavanaugh JM. Biomechanics of Thoracic Trauma BT - Accidental Injury: Biomechanics and Prevention. In: Nahum AM, Melvin JW, editors., New York, NY: Springer New York; 2002, p. 374–404. https://doi.org/10.1007/978-0-387-21787-1_16.
[75] Lundin L, Storm S. Detailed FE rib modelling for fracture prediction. Chalmers University of Technology, 2018.
[76] Olivier Mayeur. Personnalisation geometrique et mecanique multi-echelles du thorax humain. Universite de Valenciennes et du Hainaut-Cambresis, 2013.
[77] G. Granik and I.Stein. Human ribs: Static testing as a promising medical application. J Biomech 1973;6:137–40.
[78] Kindig MW. Tolerance to Failure and Geometric Influences on the Stiffness of Human Ribs Under Anterior-posterior Loading. University of Virginia; 2009.
[79] Tucker BK, Hutchinson DL, Gilliland MF, Charles TM, Daniel HJ, Wolfe LD. Microscopic characteristics of hacking trauma. J Forensic Sci 2001;46:234–40.
[80] Wieberg DAM, Wescott DJ. Estimating the timing of long bone fractures: correlation between the postmortem interval, bone moisture content, and blunt force trauma fracture characteristics*. J Forensic Sci 2008;53:1028–34. https://doi.org/10.1111/j.1556-4029.2008.00801.x.
[81] Christensen AM, Smith VA, Ramos V, Shegogue C, Whitworth M. Primary and Secondary Skeletal Blast Trauma. J Forensic Sci 2012;57:6–11. https://doi.org/10.1111/j.1556-4029.2011.01938.x.
[82] Christensen AM, Smith VA. Rib Butterfly Fractures as a Possible Indicator of Blast Trauma. J Forensic Sci 2013;58. https://doi.org/10.1111/1556-4029.12019.
[83] N.Zywicki M. A study of the predictability of rib fracture patterns based on three different modes of trauma. Texas State University, 2014.
[84] Gibson LJ. The mechanical behaviour of cancellous bone. J Biomech 1985;18:317–28. https://doi.org/10.1016/0021-9290(85)90287-8.
[85] Garcia D. Elastic plastic damage laws for cortical bone. ECOLE POLYTECHNIQUE FEDERALE DE LAUSANNE, 2006.
[86] Kemper AR. Material Properties of Human Rib Cortical Bone from Dynamic Tension Coupon Testing. Virginia Polytechnic Institute and State University, 2005. https://doi.org/10.4271/2005-22-0010.
[87] Carter DR, Hayes WC. The compressive behavior of bone as a two-phase porous structure. J Bone Joint Surg Am 1977;59:954–62.
[88] Kemper AR, McNally C, Pullins CA, Freeman LJ, Duma SM, Rouhana SM. The biomechanics of human ribs: material and structural properties from dynamic tension and bending tests. Stapp Car Crash J 2007.

[89] Subit D, de Dios E del P, Valazquez-Ameijide J, Arregui-Dalmases C, Crandall J. Tensile material properties of human rib cortical bone under quasi-static and dynamic failure loading and influence of the bone microstucture on failure characteristics. ArXiv:11080390v2 2011.
[90] Albert DL, Kang YS, Agnew AM, Kemper AR. A comparison of rib structural and material properties from matched whole rib bending and tension coupon tests. Conf Proc Int Res Counc Biomech Inj IRCOBI 2017;2017-Septe:567–76.
[91] Katzenberger MJ, Albert DL, Agnew AM, Kemper AR. Effects of sex, age, and two loading rates on the tensile material properties of human rib cortical bone. J Mech Behav Biomed Mater 2020;102:103410. https://doi.org/10.1016/j.jmbbm.2019.103410.
[92] Albert DL, Katzenberger MJ, Agnew AM, Kemper AR. A comparison of rib cortical bone compressive and tensile material properties: Trends with age, sex, and loading rate. J Mech Behav Biomed Mater 2021;122:104668. https://doi.org/10.1016/j.jmbbm.2021.104668.
[93] Yoganandan N, Pintar FA. Biomechanics of human thoracic ribs. J Biomech Eng 1998;120:100–4. https://doi.org/10.1115/1.2834288.
[94] Cormie JM, Stitzel JD, Duma SM, Matsuoka F. Regional variation in the structural response and geometrical properties of human ribs. Annu Proc - Assoc Adv Automot Med 2005:153–70.
[95] Stitzel JD, Cormier JM, Barretta JT, Kennedy EA, Smith EP, Rath AL, et al. Defining Regional Variation in the Material Properties of Human Rib Cortical Bone and Its Effect on Fracture Prediction. SAE Tech Pap 2003;2003-Octob:243–65. https://doi.org/10.4271/2003-22-0012.
[96] McElhaney JH. Dynamic response of bone and muscle tissue. J Appl Physiol 1966;21:1231–6. https://doi.org/10.1152/jappl.1966.21.4.1231.
[97] Crowninshield RD, Pope MH. The response of compact bone in tension at various strain rates. Ann Biomed Eng 1974;2:217–25. https://doi.org/10.1007/BF02368492.
[98] Currey JD. The effects of strain rate, reconstruction and mineral content on some mechanical properties of bovine bone. J Biomech 1975;8. https://doi.org/10.1016/0021-9290(75)90046-9.
[99] Hansen U, Zioupos P, Simpson R, Currey JD, Hynd D. The effect of strain rate on the mechanical properties of human cortical bone. J Biomech Eng 2008;130:11011. https://doi.org/10.1115/1.2838032.
[100] Ferreira F, Vaz MA, Simões JA. Mechanical properties of bovine cortical bone at high strain rate. Mater Charact 2006;57:71–9. https://doi.org/10.1016/j.matchar.2005.11.023.
[101] Pithioux M, Subit D, Chabrand P. Comparison of compact bone failure under two different loading rates: Experimental and modelling approaches. Med Eng Phys 2004;26:647–53. https://doi.org/10.1016/j.medengphy.2004.05.002.
[102] Burstein AH, Reilly DT, Martens M. Aging of bone tissue: mechanical properties. J Bone Joint Surg Am 1976;58:82—86.
[103] McCalden RW, McGeough JA, Barker MB, Court-Brown CM. Age-related

changes in the tensile properties of cortical bone. The relative importance of changes in porosity, mineralization, and microstructure. J Bone Joint Surg Am 1993;75:1193—1205. https://doi.org/10.2106/00004623-199308000-00009.
[104] Perz R, Toczyski J, Subit D. Variation in the human ribs geometrical properties and mechanical response based on X-ray computed tomography images resolution. J Mech Behav Biomed Mater 2015;41:292–301. https://doi.org/10.1016/j.jmbbm.2014.07.036.
[105] Yates K, Untaroiu C. Subject-Specific Modeling of Human Ribs : Finite Element Simulations of Rib Bending Tests , Mesh Sensitivity , Model Prediction with Data Derived From Coupon Tests. 15th Int. LS-DYNA Users Conf., 2018.
[106] Wolfram U, Schwiedrzik J. Post-yield and failure properties of cortical bone. Bonekey Rep 2016;5:1–10. https://doi.org/10.1038/bonekey.2016.60.
[107] Wedel VL, Galloway A. BROKEN BONES: Anthropological Analysis of Blunt Force Trauma (2nd Ed.). Charles C. Thomas, Publisher; 2013.
[108] Agnew AM, Murach MM, Dominguez VM, Sreedhar A, Misicka E, Harden A, et al. Sources of Variability in Structural Bending Response of Pediatric and Adult Human Ribs in Dynamic Frontal Impacts. SAE Tech Pap 2018;2019-Novem:119–92. https://doi.org/10.4271/2018-22-0004.
[109] Fackler ML, Malinowski JA. The wound profile: a visual method for quantifying gunshot wound components. J Trauma 1985;25:522–9.
[110] Fackler ML, Bellamy RF, Malinowski JA. The wound profile: illustration of the missile-tissue interaction. J Trauma 1988;28:S21-9. https://doi.org/10.1097/00005373-198801001-00007.
[111] Bree J V, Fairlie G. Compression wave experimental and numerical studies in gelatine behind armour. Proc. 18th Int. Symp. Ballist., 1999.
[112] Bree J V, Gotts P. The twin peaks of BABT. Proc. Pers. Armor Syst. Symp., 2000.
[113] Bresson F, Ducouret J, Peyré J, Maréchal C, Delille R, Colard T, et al. Experimental study of the expansion dynamic of 9mm Parabellum hollow point projectiles in ballistic gelatin. Forensic Sci Int 2012;219:113–8. https://doi.org/10.1016/j.forsciint.2011.12.007.
[114] Wen Y, Xu C, Wang S, Batra RC. Analysis of behind the armor ballistic trauma. J Mech Behav Biomed Mater 2015;45:11–21. https://doi.org/10.1016/j.jmbbm.2015.01.010.
[115] Wang Y, Shi X, Chen A, Xu C. The experimental and numerical investigation of pistol bullet penetrating soft tissue simulant. Forensic Sci Int 2015;249:271–9. https://doi.org/https://doi.org/10.1016/j.forsciint.2015.02.013.
[116] Luo S, Xu C, Wang S, Wen Y. Transient pressure wave in the behind armor blunt trauma: experimental and computational investigation. Comput Methods Biomech Biomed Engin 2017;20:308–18.
[117] Han R, Qu Y, Yan W, Qin B, Wang S, Wang J. Experimental study of transient pressure wave in the behind armor blunt trauma induced by different rifle bullets. Def Technol 2020;16:900–9.

[118] Bracq A, Delille R, Maréchal C, Bourel B, Roth S, Mauzac O. Rib fractures prediction method for kinetic energy projectile impact: from blunt ballistic experiments on SEBS gel to impact modeling on a human torso FE model. Forensic Sci Int 2019;297:177–83. https://doi.org/10.1016/j.forsciint.2019.02.007.
[119] Bracq A, Delille R, Maréchal C, Bourel B, Lauro F, Roth S, et al. On the use of a SEBS polymer gel block as a new ballistic target to assess blunt ballistic impacts: Application to a wide range of LLKE projectiles. Int J Impact Eng 2021;153. https://doi.org/10.1016/j.ijimpeng.2021.103874.
[120] Veysset D, Sun Y, Lem J, Kooi SE, Maznev AA, Cole ST, et al. High-Strain-Rate Behavior of a Viscoelastic Gel Under High-Velocity Microparticle Impact. Exp Mech 2020;60:1179–86. https://doi.org/10.1007/s11340-020-00639-9.
[121] Stein ID, Granik G. Rib structure and bending strength: An autopsy study. Calcif Tissue Res 1976. https://doi.org/10.1007/BF02546398.
[122] Hideyuki Kimpara, Masami Iwamoto, Kazuo Miki, Jong B. Lee, Paul C. Begeman, King H. Yang AIK. Biomechanical Properties of the Male and Female Chest Subjected to Frontal and Lateral Impacts. Ircobi 2003:235–47.
[123] Estelle Charpail. Mechanical behavior analysis of human ribs in dynamics. Arts et Metiers ParisTech, 2006.
[124] Aubert R, Pavier J, Eches N, Langlet A, Bailly P. On the use of Hopkinson bar-bending apparatus to study soft impact on porcine ribs. Comput Methods Biomech Biomed Engin 2012;15 Suppl 1:311–2. https://doi.org/10.1080/10255842.2012.713674.
[125] Ayagara AR. Caracterisation de la fracturation dynamique des os de la cage thoracique: simulations numeriques et validation experimentale. Universite D'Orleans, 2019.
[126] Trosseille X, Baudrit P, Leport T, Vallancien G. Rib cage strain pattern as a function of chest loading configuration. Stapp Car Crash J 2008;52:205–31.
[127] Li Z, Kindig MW, Kerrigan JR, Untaroiu CD, Subit D, Crandall JR, et al. Rib fractures under anterior – posterior dynamic loads : Experimental and finite-element study. J Biomech 2010;43:228–34. https://doi.org/10.1016/j.jbiomech.2009.08.040.
[128] Kindig M, Lau AG, Kent RW. Biomechanical response of ribs under quasistatic frontal loading. Traffic Inj Prev 2011;12:377–87. https://doi.org/10.1080/15389588.2011.583960.
[129] Perz R, Toczyski J, Kindig M, Ito D, Ejima S, Kamiji K, et al. Evaluation of the Geometrical Properties Distribution Along the Human Ribs Using Different X-Ray Imaging Methods. IRCOBI Conf., 2013.
[130] Agnew AM, Schafman M, Moorhouse K, White SE, Kang YS. The effect of age on the structural properties of human ribs. J Mech Behav Biomed Mater 2015;41:302–14. https://doi.org/10.1016/j.jmbbm.2014.09.002.
[131] Murach MM, Schafman M, Kang Y, White S, Iv JHB, Moorhouse K, et al. Geometric Properties of Human Ribs as Predictors of Structural Properties. Inj

Biomech Symp 2015:1–12.
[132] Albert DL, Kang YS, Agnew AM, Kemper AR. A comparison of rib structural and material properties from matched whole rib bending and tension coupon tests. Conf Proc Int Res Counc Biomech Inj IRCOBI 2017;2017-Septe:567–76.
[133] Kang YS, Kwon HJ, Stammen J, Moorhouse K, Agnew AM. Biomechanical Response Targets of Adult Human Ribs in Frontal Impacts. Ann Biomed Eng 2021;49:900–11. https://doi.org/10.1007/s10439-020-02613-x.
[134] Luo S, Xu C, Wang S, Wen Y. Transient pressure wave in the behind armor blunt trauma: experimental and computational investigation. Comput Methods Biomech Biomed Engin 2017;20:308–18. https://doi.org/10.1080/10255842.2016.1228908.
[135] Awoukeng-Goumtcha A, Taddei L, Tostain F, Roth S. Investigations of impact biomechanics for penetrating ballistic cases. Biomed Mater Eng 2014;24:2331–9. https://doi.org/10.3233/BME-141046.
[136] Iraeus J, Brolin K, Pipkorn B. Generic finite element models of human ribs, developed and validated for stiffness and strain prediction – To be used in rib fracture risk evaluation for the human population in vehicle crashes. J Mech Behav Biomed Mater 2020;106:103742. https://doi.org/10.1016/j.jmbbm.2020.103742.
[137] Johnson AF, Holzapfel M. Modelling soft body impact on composite structures. Compos Struct 2003;61:103–13. https://doi.org/10.1016/S0263-8223(03)00033-3.
[138] Nagayama K, Mori Y, Motegi Y, Nakahara M. Shock hugoniot for biological materials. Shock Waves 2006;15:267–75. https://doi.org/10.1007/s00193-006-0030-5.
[139] Wu JZ, Dong RG, Schopper AW. Analysis of effects of friction on the deformation behavior of soft tissues in unconfined compression tests. J Biomech 2004;37:147–55. https://doi.org/10.1016/S0021-9290(03)00240-9.
[140] Altair. HyperWorks 2017 Radioss User Guide 2017.
[141] Wolfram U, Schwiedrzik J. Post-yield and failure properties of cortical bone. Bonekey Rep 2016;5:1–10. https://doi.org/10.1038/bonekey.2016.60.
[142] Niu Y, Shen W, Stuhmiller JH. Finite element models of rib as an inhomogeneous beam structure under high-speed impacts. Med Eng Phys 2007;29:788–98. https://doi.org/10.1016/j.medengphy.2006.08.015.
[143] Holcombe SA, Kang YS, Derstine BA, Wang SC, Agnew AM. Regional maps of rib cortical bone thickness and cross-sectional geometry. J Anat 2019;235:883–91. https://doi.org/10.1111/joa.13045.
[144] Li, Z., Subit, D., Kindig, M., Kent R. Development of a finite element ribcage model of the 50th percentile male with variable rib cortical thickness. Thirty-Eight Int Work Inj Biomech Res 2010. https://doi.org/10.4271/942210.

Publications

J. Shen, S. Roth (2021). Effect of geometrical and mechanical parameters of ribs submitted to high velocity impact. A numerical investigation. Mechanics of Advanced Materials and Structures, DOI: 10.1080/15376494.2021.1919802.

J. Shen, L. Taddei, S. Roth (2020). Numerical modeling of a human tissue surrogate SEBS gel under high velocity impacts: investigation of the effect of the strain rate in an elasto-hydrodynamic law. Mechanics of Advanced Materials and Structures, DOI: 10.1080/15376494.2020.1761490.

S. Meng, J. Shen, L. Taddei, et al. Modelling of micro-particles perforations into human tissue surrogate: Numerical and analytical aspects. Extreme Mechanics Letters 2021;45:101299.

J. Shen, S. Roth. Validation of rib structural responses under dynamic loadings using different material properties: A finite element analysis. Medical Engineering & Physics. (under review)

SPIM

Titre: Contribution à l'étude des réponses dynamiques des tissus humains sous des impacts à haute vitesse en utilisant la modélisation par éléments finis

Mots clés: méthode des éléments finis, impact à haute vitesse, tissus humains, fracture des côtes, modélisation constitutive

Résumé: Cette thèse vise à étudier les réponses dynamiques des tissus humains sous des impacts à haute vitesse en utilisant la modélisation par éléments finis. Premièrement, une nouvelle loi de comportement élasto-hydrodynamique dépendante de la vitesse de déformation du gel polymère synthétique SEBS a été développée et implémentée en tant que «loi utilisateur» dans Radioss pour simuler les comportements dynamiques du gel SEBS. Les corrélation essais/calculs valident le modèle et révèlent l'importance et l'effet de vitesse de déformation, en particulier pour les vitesses de déformation élevées. La seconde partie traite de l'étude numérique des réponses dynamiques et des fracture de côtes sous flexion dynamique trois points et flexion antéro-postérieure. Les études de sensibilité mettent en évidence l'effet significatif des paramètres géométriques comme l'épaisseur corticale et la section transversale sur les comportements dynamiques des côtes. De plus, des paramètres mécaniques tels que le mode de chargement, la vitesse de déformation et l'âge doivent également être pris en compte lors de la modélisation par éléments finis des côtes. De manière générale, les lois de comportement du substitut de tissus mous, ainsi que celles des côtes donnent des résultats très satisfaisants, et mènent à des modélisation biofidèles, permettant à ces modèles d'être implémentés dans un modèle global du thorax pour une utilisation dans un contexte de traumatismes du corps humains sous impacts à hautes vitesses.

Title: Contribution to the investigation of dynamic responses of human tissues under high velocity impacts using finite element modeling

Keywords: finite element analysis, high velocity impact, human tissues, rib fractures, constitutive modeling

Abstract: This thesis aims to investigate the dynamic responses of human tissues under high velocity impacts using finite element modeling. Firstly, a novel strain-rate-dependent elasto-hydrodynamic constitutive law of the synthetic polymer Styrene-Ethylene-Butylene-Styrene (SEBS) gel was proposed and used as a user subroutine in Radioss for interpreting dynamic behaviors of SEBS gel. Numerical analysis validates the model's accuracy and reveals the significance of strain-rate-dependence effect especially for high strain rates. Then, this thesis numerically investigated dynamic responses and fractures of isolated ribs subjected to dynamic three point bending (3PB) and anterior-posterior bending respectively. Sensitivity studies highlight the significant effect of geometrical parameters like cortical thickness and cross section on ribs' dynamic behaviors. Moreover, mechanical parameters like loading mode, strain rate and age are also needed to be considered when modeling FE rib models. Overall, the proposed law of SEBS gel and established rib models can be applied in a global thorax model for human trauma investigations under high velocity impacts.

UBFC UNIVERSITÉ BOURGOGNE FRANCHE-COMTÉ

Université Bourgogne Franche-Comté
32, avenue de l'Observatoire
25000 Besançon